THÈSE

En vue de l'obtention du

DOCTORAT DE L'UNIVERSITÉ DE TOULOUSE

Délivré par :

Institut National Polytechnique de Toulouse (Toulouse INP)

Discipline ou spécialité :

Photonique et système optoélectronique

Présentée et soutenue par :

M. EINAR KNUDSEN

le mardi 18 mai 2021

Titre :

Nonintrusive Acoustic Measurements by Optical Feedback Interferometry

---

Ecole doctorale :

Génie Electrique, Electronique, Télécommunications (GEETS)

Unité de recherche :

Laboratoire d'Analyse et d'Architecture des Systèmes (LAAS)

Directeur(s) de Thèse :

M. THIERRY BOSCH

M. JULIEN PERCHOUX

Rapporteurs :

M. JEAN-CHRISTOPHE VALIERE, UNIVERSITE DE POITIERS

MME YANGUANG YU, Université de Wollongong

Membre(s) du jury :

M. ALEKSANDAR RAKIC, UNIVERSITY OF QUEENSLAND, Président

M. JULIEN PERCHOUX, TOULOUSE INP, Membre

M. MAURIZIO DABBICCO, UNIVERSITA DEGLI STUDI DI BARI, Membre

M. THIERRY BOSCH, TOULOUSE INP, Membre

M. THIERRY MAZOYER, ACOEM FRANCE, Invité(e)

Acknowledgments

That's it. It's finally finished. The research is done, the publications are published and the defense is coming up in a few days at the time of writing this very phrase. It's been six years since I first set foot in Toulouse to get my masters degree in electronics, and to my great surprise I ended up with a PhD.

First of all I would like to thank my three PhD directors for giving me the opportunity to do this PhD. Here at the lab, Julien Perchoux and Thierry Bosch, with their state of the art scientific insight, have given me excellent and much needed support throughout my research. At ACOEM I would like to thank Thierry Mazoyer who is a through and through idea production machine. As the director of the department of innovation he has been following me at a weekly basis, giving me much needed support and acoustic insight.

During my time spent at Limonest with ACOEM, I've always felt welcomed by the team led by Thierry and we've spent several nice moments together. A big thank you to everyone at the department of innovation. Pascal, who is off to discover new horizons, helped me a lot at the beginning of my PhD, so a grand thank you is due for all his help.

Most of my time was spent here at the lab in Toulouse. So a big thank you is in order for Bastien, my fellow PhD student, for four good years of research together. Thank you for all the help with both heavy and basic calculations and the time spent bouncing ideas around for our separate research projects. Your defense is coming up very soon too, and I'm much looking forward to it.

The rest of the team has always been there, be it to build experiments, discuss laser interferometry and physics, or to eat croissants at 10:00 in the morning during coffee. A large thank you to Francis and Clément for all the help with the experiments and for our nice discussions together. A big thank you to Emmanuelle for keeping up with the administration and keeping track of all the paper work. Both Adam and the ever returning Michael make the lab lively and I've had a great time working with both of you. Michael, I'm still putting your name on my latest publication (if it's ever published), so sorry for the additional paperwork that is going to give you.

Over the course of the PhD people have come and gone, and the previous generation of PhD students all have their degree now. Big thank you to Fernando and his family for being such great people, and especially Fernando who is a real visionary with a big heart. Mengkoung is now back on the other side of the planet also. A big thank you for all our great discussions, Mengkoung, and with the help with my simulations.

Luckily, my time in Toulouse haven't been only work but a lot of pleasure too. I've

shared many good moments with the Cool Kids; Shivank, Vincent (Du Heng), Lucas, Laura, Yevgeniy and Alessia, Argheesh, Kuba and Plinio. I especially appreciate the time I spent with Shivank during our first months in Toulouse, our many dinners together after class and passionate discussions. These where the best days. An enormous thank you to all of the Cool Kids, and also to all our Chinese friends for all the dinner parties, picnics, travels and good moments we've spent together. I'm looking forward to our next trip abroad, wine-tasting or park strolling together.

I'm glad I discovered Taekwondo thanks to the people over at TéSA. I'm much looking forward to return to the sparring mat with you, Quentin, Laëtitia, Lorenzo and Adrien. You, and the friends over at SupAero are always up for a get-together and I always appreciate our discussions. Thank you Franco, for our bike rides and the paella, and to Guillaume for our nice mountain hikes. Also, a big congratulations Quentin who defended his PhD just a week ago today. Next winter we'll all go skiing again, and we all laugh about being doctors but not being able to help each other in case of an accident (since we're the wrong type of doctors).

Also my best friends up in Norway, Thomas, Anders and Jan Petter deserves a big thank you for the great times we've spent together. Despite of the distance between Norway and France we've managed to stay in touch, which i greatly appreciate.

I should also give a great thanks and infinite hugs and kisses to my little family who've supported me throughout my time in France and especially during the PhD. They've learned by heart now how much I dislike administration. This being said, they've been there for me a 100% of the time non-stop. Coming back home is always a pleasure that i cherish dearly. Thank you Mamma, Pappa, Torunn, Halvor and Marit for being the best family anyone could ever ask for.

Finally, the one guilty (at least to some degree) of convincing me to get my PhD; Selma. You've been there by my side supporting me through the ups and downs, the gray weekdays, the sunny travels, the rainy days, the times of joy and the times of distress. You've always kept my morals up, no matter what. We've had a beautiful journey together, from our humble trips to the park with our books, to getting our first car together and driving it to Italy. I enjoy every second I spend by your side. Thank you for loving me, Selma, and know that my heart is yours.

Contents

List of Figures

List of Tables

Table of Acronyms

OFI	Optical Feedback Interferometry
SM	Self-Mixing
SM-signal	Signal acquired from the laser's photo diode
PV	Probe Volume
PIV	Particle Image Velocimetry
LDV	Laser Doppler Vibrometer
LDA	Laser Doppler Anemometer

Introduction

Context and Objectives

The ACOEM Group is a long term leader in the sound and measurement industry. ACOEM delivers diagnostic systems for the industry through acoustic and vibrational analysis and expertise. Such systems are used in preventive maintenance and to reduce companies' environmental impact through sound and vibration reduction. They deliver real-time pollution detection, threat detection and surveillance through acoustic signature recognition. In the military domain they have a range of detectors capable of recognizing gun shot signatures and the origin of the projectile. This PhD is a collaborative work between the LAAS - CNRS and ACOEM to produce research on a new range of acoustic detectors based on Optical Feedback Interferometry (OFI) for use in the industry.

By recording the sounds in our environment we develop a better understanding of our surroundings. Hearing aides record sound and play it back instantly. Industries reduce their environmental impact by reducing noise. Preventive maintenance is made possible through audio and vibration recordings of industrial machines, increasing the machine lifespan and reducing costs. Sound acquisition devices are found everywhere. Due to the vast number of situations where sound recordings is necessary, microphones are found in all shapes and sizes.

Fundamental sciences such as metrology use accurate acquisition devices to precisely characterize sound fields. Such characterizations are necessary in order to understand the propagation and interaction of sound waves with materials. The information may then be used in different industries to perform strain analysis of materials, create better sound insulation, produce consumer products or create new military applications to mention a few.

Researchers and engineers are constantly developing and improving sound acquisition devices to make them more precise, more durable, cheaper and more versatile. Today the vast majority of microphones are based on transducers and diaphragms. These are moving parts that degrade over time and their performances depend on the environmental conditions. A microphone mounted on a vehicle in the dessert may need frequent maintenance, whereas the intercom at the office may function for years of use without any problem.

Through the use of optical microphones some of the problems related to mechanical parts have been addressed. Optical systems would not be prone to the same level of main-

tenance as classical acoustic detection systems. With no moving parts the issue of material inertia related to the mass of the microphone diaphragm is eliminated. Interferometers can be used to detect acoustic waves by direct measurements of the refractive index of air. Inside the oscillating pressure wave, the refractive index of air will also oscillate. This effect is called the acousto-optic effect and can be measured as an optical path change of the laser beam inside the acoustic wave.

An advantage of interferometry based sound acquisition systems that use the acousto-optic effect is that they can be used to characterize sound fields without perturbing them. The classical microphone has to be positioned in the sound field to operate, whereas the interferometer uses the laser beam to measure the sound wave, without touching it.

The major drawback of these interferometric systems is that they can be quite bulky. In many cases, several optical components are needed to make these systems work and these tools are often very specialized. Another drawback is their price. Classical interferometer systems are highly specialized and often comes with a very high price tag. For these reasons it is often not practical to use interferometers to acquire sound.

Optical Feedback-based interferometers have a much smaller footprint, are a lot cheaper and can be made by of-the-shelf parts. This renders the OFI-sensing scheme very interesting for non intrusive sound acquisition. Its small size makes it easy to integrate, and its affordable price makes it more accessible than classical interferometers. The OFI-based acoustic detector is thus an interesting candidate to replace the microphone as it encompasses the advantages posed by classical optical detectors in addition to the OFI-specific advantages just mentioned.

The acousto-optic effect has been measured using OFI by researchers of the LAAS-CNRS in a seminal paper [1]. In this PhD we attempt to use the OFI sensing scheme to develop a Class 1 acoustic detector. These detectors are characterized as being extremely linear, they can operate in a wide temperature and pressure range, and to measure acoustic waves as small as 20 $\mathrm{dB_{RMS}}$.

We investigate the impact of environmental factors on the refractive index, the parameter measured in order to acquire sound. we also investigate the lowest detectable acoustic pressure using this method. These studies are compared to the norms of a class 1 microphone.

Laser interferometers have been used to measure the movement of particles in the air. When these particles are pushed by an acoustic wave, the particle movement is recorded and information of the sound wave can be acquired. In this we PhD study the concept of and an acoustic LIDAR using the OFI sensor. We investigate what information can be extracted from a flow of moving particles and if this information can be used to extract acoustic information from a passing sound wave. We then propose an implementation of

an OFI sensor that in a LIDAR configuration. We study it's performances under variable conditions such as short an long distance acquisitions.

Thesis Structure & Scientific Contributions

Chapter 1 is introductory and discusses acoustic acquisition devices and Optical Feedback Interferometry theory. We start with a brief introduction of the concept of sound, then the main acoustic acquisition devices that exist in the literature are covered. These are divided into diaphragm-based and diaphragm-free devices. We also cover a section of non contact acoustic measurement. Then we introduce the basic theory and governing equations of Optical Feedback Interferometry. This gives a platform for understanding the concepts proposed in Chapter 2 and Chapter 3. At the end of Chapter 1 we discuss some applications where OFI has been used in acoustic acquisition.

Chapter 2 is dedicated to the class 1 OFI microphone. Here we investigate the limits of the OFI sensor for acoustic measurements using the acousto-optic effect. The optical path change in an acoustic pressure wave is smaller than a half laser wavelength. We have investigated the difficulty of measurement of such a small equivalent displacement and we show that shape of the interferometric fringe will have an impact on the amplitude of the detected signal.

We investigate the impact of the environmental parameters temperature, atmospheric pressure humidity have on the refractive index of air. Through this study we verify if the refractive index of air can indeed be used as a tool to make an optical class 1 microphone.

To quantify the acousto-optic effect, a model to calculate the optical path change in a pressure wave is developed. An experimental study is made to verify the correct workings of the model and to find the lowest detectable acoustic pressure using our system, to compare it to a class 1 microphone.

Chapter 3 contains the study of another non intrusive method to measure acoustic waves. Here we use the OFI-sensing scheme in a LIDAR configuration. In this configuration we attempt to measure acoustic waves by measuring the oscillatory movement of particles in air as the acoustic waves travel by. The acoustic waves set the particles into motion, which can be measured using our OFI sensor.

The acoustic signals are extracted from the OFI-sensor's output signal using a demodulation algorithm. The performance of the algorithm is studied through acquisitions of acoustic signals at different frequencies and amplitudes, at a distance from the OFI sensor. We study the performance of the sensor and its demodulation algorithm both at a close

range just shy of a meter, and at a long range of over 10 meters.

When the distance between the target we are measuring and the laser is high, the laser may become unstable. This degrades our sensor signal. Thus a complementary study in regards to laser stability and particle reflectivity is presented for the long range acquisitions.

The final chapter is dedicated to a general conclusion and future perspectives. Here we will give a brief summary of our achievements, the challenges we've encountered and the future perspectives of the technology.

Over the course of this PhD thesis we've had the following opportunities to communicate our work.

- Journal article: E. Knudsen, J. Perchoux, T. Mazoyer, J. J. Imas, M. Veng, F. Jayat, C. Tronche, and T. Bosch, "*Experimental demonstration of the impact of the fringe shape in sub-lambda/2 sensing with optical feedback interferometry*," Appl. Opt. 60, 119-124 (2021).
- Conference paper: E. Knudsen, J. Perchoux, T. Mazoyer, F. Jayat, C. Tronche and T. Bosch, "*Lower detection limit of the acousto-optic effect using Optical Feedback Interferometry*," 2020 IEEE International Instrumentation and Measurement Technology Conference (I2MTC), Dubrovnik, Croatia, 2020, pp. 1-4, doi: 10.1109/I2MTC43012.2020.9128405.
- International Workshop: IEEE France 2020 Workshop, presentation on "*Acoustic LIDAR using Optical Feedback Interferometry*".
- Award: Laureate of Best Student Presentation Award IEEE France 2020 Workshop.

Chapter 1

Sound Acquisition Systems & Literature Review

Contents

1.1 Introduction

The physical acquisition of sound dates back to the mid 19th century when a French inventor by the name of Édouard-Léon Scott de Martinville filed a patent for a mechanical deivce called the phonoautograph. Patented on March 25th in 1857, the phonoautograph recorded sound waves by transcribing mechanical vibrations onto paper covered in soot [2]. The engravings in the soot reflected the recorded sound waves. Since then the technology has much developed and today we find ourselves with a lavish choice of acoustic detectors. Sound recording devices are found in many industries, ranging from machine monitoring to entertainment to medical applications. The vast majority of these detectors are based on the principle of a diaphragm that moves in response to a change in atmospheric pressure. There are several types of detectors capable of recording sound. Generalities in regards to some of the principal detectors in use today and how they work will be discussed in this chapter.

We start of by a brief description of sound and the concept of propagating sound waves. From there we will discuss the main acoustic detectors available. We divide the acoustic detectors into two main categories: Diaphragm based detectors and detectors without the need of a diaphragm. The chapter also cover laser and non intrusive acquisition techniques. We describe acoustic acquisition through the measurement of particle movement using different acquisition systems. We also cover acoustic acquisition through measurements of the refractive index of air.

After these bibliographic studies, we introduce the concept of Optical Feedback Interferometry and we describe the operating principles and the governing equations of this measurement cheme. Three measurement configurations are then presented. These configurations are used as a base on which to construct the two main research topics in this PhD.

A bibliographic study is presented regarding measurements of the acouso-optic effect. This section also contain the main equations regarding this sensing configuration. These are subjects to be discussed in Chapter 2, where we test the hypotheses outlined in this section.

Finally we propose an entirely new way of measuring sound using the OFI-sensing scheme. This OFI configuration has never been used before to acquire acoustic signals. We draw on experience from several fields including fluid measurements and anemometry.

1.2 Sound

What is sound? Sound can be defined as a material wave propagating through a medium such as gas, a liquid or a solid. For most animals, sound is interpreted as the repetition of material waves that are recorded, generally by our ears, and interpreted by the brain. Sound is created when a force pushes on an ensemble of molecules in a transmission medium, that in turn depose their kinetic energy into adjacent molecules. This sets of a chain reaction of movement that propagates through the medium. After pushing the adjacent molecules or particles, the initial particle will return back to it's resting position.

Sound cannot propagate where there is an absence of material, such as in vacuum. There are two main types of waves with slightly different properties. The Longitudinal waves are those just explained, where the waves propagate through the alteration of pressure. In solids there are also transverse waves that are essentially shear stress at a 90° angle to the propagation direction. These waves are similar to what one would observe in a rope tied to a wall where someone flicked the other end rapidly up and down. Both types of waves are presented in Fig 1.1.

Figure 1.1: Left: Longitudinal waves. Right: Transverse waves [3]

We define sound pressure as the variation of pressure in air Δp from the static pressure p_0 which is typically the atmospheric pressure. A sound wave is in general a sinusoidal alteration of air pressure, giving rise to the following expression.

$$p(t) = p_0 + \Delta p_{\max} \sin(\omega_{\mathrm{a}} t + \phi) \tag{1.1}$$

where $p(t)$ is the measured sound pressure, $\Delta p_{\max}$ is the maximal amplitude of the pressure variation, $\omega_{\mathrm{a}} = 2\pi f_{\mathrm{a}}$ is the angular frequency where f_{a} is the acoustic frequency, t is time and ϕ is a phase term.

Throughout this manuscript the acoustic pressure will often be measured as the zero to peak value, instead of the rms value which is calculated as

$$p_{\mathrm{rms}} = \frac{\Delta p_{\max}}{\sqrt{2}} \tag{1.2}$$

This is because the acoustic pressure will be converted to displacement amplitudes and velocities, which are natural to express in zero to peak values. Whenever the pressure is

measured in either zero to peak or in rms, it is clearly marked and should not be a source of confusion.

The human ear has a pain threshold of about 20 Pa and can hear sounds as low as 20 μPa which is called p_{ref}. To calculate the Sound Pressure Level (SPL), p_{ref} is used.

$$L_p = 10 \log_{10} \left(\frac{p_{\text{rms}}}{p_{\text{ref}}} \right) \tag{1.3}$$

where L_p is the SPL expressed in decibel (dB).

The sound intensity I is measured in W/m^2 and is a measure of energy passing through a unit of surface per unit of time. It can be used to calculate the velocity v of the particle movement in a sound wave.

$$I = pv \tag{1.4}$$

The acoustic intensity I can be measured with a device called an intensity probe. This device functions by measuring the acoustic pressure p at two points in space using a microphone duplet. A microphone duplet is a device consisting of two microphones with a fixed spacing between them. As the acoustic wave pass over the duplet, the gradient of pressure between the two microphones is obtained. The particle velocity is then found by

$$v = -\frac{1}{\rho} \int \text{Grad } p \tag{1.5}$$

Where ρ is the density of air and the pressure $p = (p_1 + p_2)/2$ which is the average pressure between the two microphones during the acquisition. The particle velocity v can thus be used to calculate the acoustic intensity I or be used to estimate the oscillation velocity of a small aerosol suspended the air, inside the acoustic wave.

1.3 Sound Acquisition devices

In this PhD we to contribute to the development of non intrusive, laser based sound acquisition systems. An overview of existing acquisition devices is thus provided in this section. We will distinguish between two main types of sound systems, some with overlapping properties. On the one hand we have systems that converts the movement of a diaphragm or a diaphragm-like target to an acoustic signal. These detectors constitute the vast majority of acoustic detectors on the market.

On the other hand there are systems that measures a change in particle flow or in refractive index of air. These systems does not depend on the movement of a target or

diaphragm. These systems are often more specialized and used in special applications and research.

In the following section we will cover both types of systems. We acknowledge that there is some overlap between these two categories, especially in regards to optical systems. Thus we ask the reader to bear with us while we attempt to separate the different acquisition schemes into "classical" acquisition systems and systems that are similar to the ones developed in the research in this PhD thesis.

1.3.1 Diaphragm Based Microphones

Electro Mechanical Microphone

Most classical microphones are transducer based, converting acoustic pressure waves into an electric signal through the movement of a diaphragm attached to an electromechanical circuit. A dynamic microphone acquires it's signal through electromagnetic induction; A coil is wrapped around a magnet, as shown in Fig. 1.2, and the movement of a diaphragm moves the coil in which an electric current is created. The electrical signal is in turn amplified and filtered by appropriate circuits before it is digitalized and stored.

Similar microphones, such as the condenser microphone, use the vibrations in a capacitor plate that acts as a diaphragm. The change in capacity reflects the incoming acoustic pressure wave. Piezo electric microphones use crystals that produce a voltage when subjected to compression. MEMS microphones are easily miniaturized as the diaphragm is etched onto a silicon wafer. ADC circuits are often etched directly onto the chip itself, making these microphones vastly popular due to their size and cost.

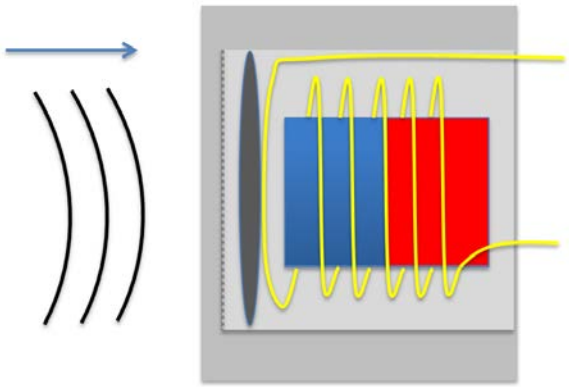

Figure 1.2: Dynamic Microphone with a diaphragm attached to a coil that is wrapped around a magnet. Pressure waves coming in from the left.

The common advantage of the electro mechanical microphone is that it can be produced very cheaply and can be made very small. Their dynamic range is a function of the materials used, shape and often cost. Properties such as a high dynamic range and linearity are often associated with high cost. A disadvantage of such microphones is that they can be perturbed by electromagnetic radiation and electric fields, such as those encountered at the vicinity of high tension generators or some types of medical equipment.

The transducer based microphones are found in most audio recording and detection applications. One application is the microphone array which is an ensemble of microphones working in tandem to produce a desired effect such as acoustic source localization or determination of acoustic field shapes. When the sound wave or sound field impinges on the microphone array, the pressure at each microphone location is recorded and time stamped. Data processing then reconstruct the sound field in two or three dimensions. The resolution of the measurement depends on the array's spatial dimensions. There is a trade off between resolution and fidelity in the sense that a high density array with many points of measurements may perturb and distort the acoustic wave. An array with fewer points of measurements will interfere less with the acoustic wave, but will also have a lower resolution.

Fiber Optic Microphone

The fiber optic microphone is similar to the electro mechanical microphone in that it too has a moving diaphragm. The fiber optic microphone uses light to record the signal [4]. Light from a light source travels through a fiber and is reflected off the diaphragm back the way it came. The reflected light's intensity is modulated by the movement of the diaphragm and a photodetector acquires the signal. The acoustic signal is obtained from the intensity modulation created by the moving diaphragm. Figure 1.3 shows an example of a fiber microphone.

An advantage of such microphones is their immunity to electro magnetic radiation and magnetic fields. This makes the fiber optic microphone particularly suitable for settings where sound is recorded in the presence of strong magnetic fields such as during magnetic resonance imaging (MRI). The size is relatively small and the microphone is lightweight. Thanks to the optical fiber the electronic equipment may be placed out of harms way. A drawback is however that the microphone is less portable due to the optical fiber which may become relatively long depending on the situation. Optical fibers are fragile and thus needs to be protected which encumbers the device. For these reasons the fiber optical microphone stays a rather niche product.

Figure 1.3: Optical Fiber Microphone [4], [5] where light reflected from the diaphragm is used to register audio signals.

Intensity Modulated Laser and Interferometric Laser Microphones

Often associated with espionage, laser microphones may record sound at a distance. The predecessor of this type of microphone was invented around or before 1947 by Russian and Soviet inventor Léon Theremin [6]. The device used an infrared beam that was reflected off distant surfaces such as walls or windows. As sound waves impinge on these surfaces they vibrate. This creates a modulation of the reflected intensity of the light beam, which is capture by a photodetector. The principle is largely the same today where lasers are used instead of the original beam of infrared light [7]. The returning light hits a photodetector as shown in Fig. 1.4a and the recorded signal is converted into audio and denoised.

Several companies offer these kinds of microphones, often in relation to counter terrorism and protection. The quality of sound acquisition depends on factors such as the quality of air through which the light travels, the reflecting surface and distance. Such microphones are rather expensive and only work when there is a vibrating surface that can act as a diaphragm. Today counter-measurements are implemented to block this kind of audio recording device [7]. This device can however be used in industrial monitoring where machines vibrate, and thus the vibration can be recorded at a distance.

Following the same principle as light modulation based microphones, the interferometric based laser microphone needs a vibrating target in order to record sound. Thus we consider this device a diaphragm based microphone in this section. It is worth mentioning that although in this example the interferometric microphone needs a vibrating target, the technology could be used as a contactless acquisition device (ref. Section 1.4).

A variety of interferometers exist, and the type is in general adapted to the application at hand. Figure. 1.4b shows an example of a basic Michelson interferometer. The reference

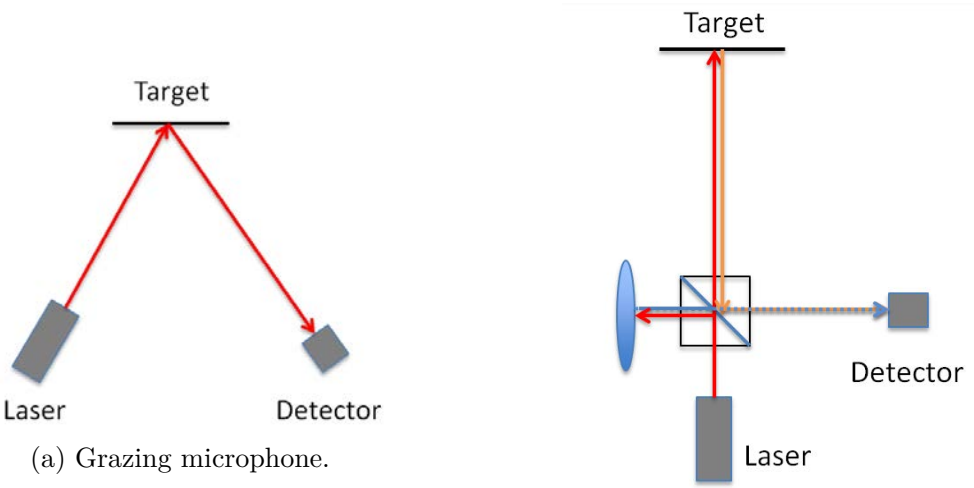

(a) Grazing microphone.

(b) Interferometric microphone

Figure 1.4: Laser microphones recording movement of distant vibrating diaphragm.

beam is generated using a beam splitter, sending half the beam into a mirror and then into a detector. The other half goes through the beam splitter and hits the distant target before being reflected back to the beam splitter and then to the detector. The interference between these two beams is used to gather information of the moving target, and thus the sound waves that set it in motion. The advantages of an interferometric device is that it may acquire very precise informations about the movement of the target it is pointing on. These informations are crucial in order to reconstruct the sound wave that sat it in motion. These devices can however be both cumbersome and quite expensive, which is a limiting factor.

1.3.2 Diaphragm Free Microphones

There are several sound acquisition systems that does not need a vibrating diaphragm to record audio. Some of these systems record densities in a flux, others a variation of refraction index of air as the sound wave passes. The advantage of some of these systems is their ability to record a sound wave without perturbing it, as would be the case with classical microphones. In the case of particle anemometry based acquisitions, the moving particle could be interpreted as a diaphragm. We have however chosen to consider this as a diaphragm free system as it differs quite substantially from the systems discussed in Section 1.3.1.

Hot Wire Anemometer

The hot wire anemometer is a device normally used for flow measurements. An electric current subjected to constant measurement passes through a small string, often only a few μm thick. As flux, often air, flows over the string, the temperature and thus the

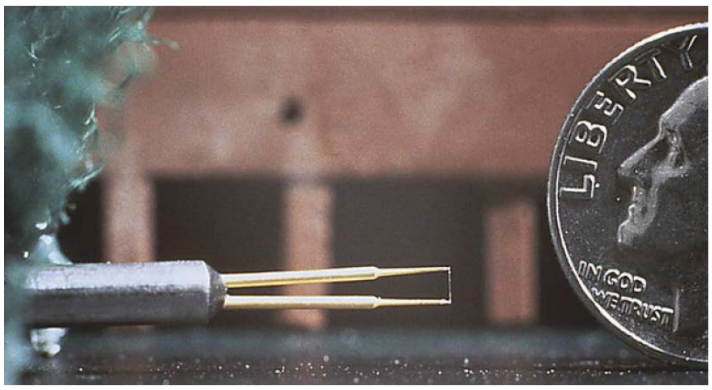

Figure 1.5: Hot wire anemometer [8]

resistance of the wire change [8]. This change mirrors the flux velocity. The hot wire anemometer has been applied to acoustic sensing, and M. R Davis [9] noted that acoustic waves would influence the velocity of the flux measured by his hot wire anemometer. Huelsz and López [10] measured low frequency sound waves in a flux using a similar method. The variations in pressure will change the electric properties of the wire, and information of the acoustic pressure is recorded. The advantages of these devices are their ability to measure acoustic waves in very high speed fluxes, and the small size which leads to only minor perturbations of the acoustic field.

Particulate flow detection microphone

The Particulate flow detection microphone is an optical microphone with similarities to a hot-wire anemometer [11]. The system measure the opacity of a semi transparent flux that flows between a light emitter and a photodetector. As a sound wave travels through the flux, its density and thus opacity changes. The light detected by the photodetector is modulated and the optical signal is an image of the acoustic signal.

This microphone mitigates problems related to inertia in the diaphragm found in transducer based microphones. Resonances are also removed as the flux is linearly coupled with the air pressure change.

Particle Image Velocimetry

Particle Image Velocimetry (PIV) has been around for a while and was developed for the fluid mechanics domain to measure 2D velocity fields in fluids. The method started to be applied to acoustics in the beginning of the 21st century using pulsed lasers and high speed cameras [12]. Ronald J. Adrian [13] proposed using lasers to illuminate particles and Willert and Gharib [14] proposed digital signal processing techniques to image the velocity fields. The majority of PIV systems used today has similar setups [12]. In 1997 Hann and Greatet [15], [16] applied the pulsed laser method to measure acoustic particle velocities.

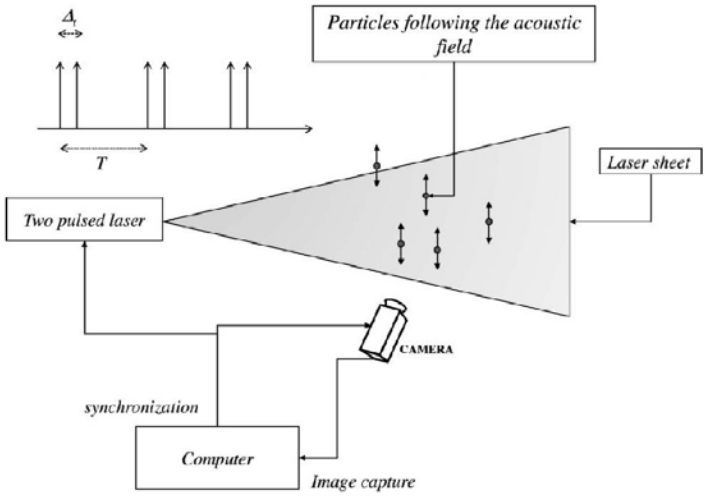

Figure 1.6: Typical PIV setup [12]

Figure 1.6 presents a schematic of a typical PIV setup where a high speed camera records light scattered off particles traversing a laser beam. Typically a pulsed laser is used and the particle position is recorded for each laser pulse. The pulses are controlled electronically if the laser allows for it. In some cases a continuous laser is used, and the pulses are created by placing a spinning disc with spaced openings in front the laser beam. Here, the spacing of the openings is carefully adapted to the system and the velocity of the disk is set accordingly.

Regardless of the system, the laser beam is often shaped into a sheet to illuminate a zone through which the particles travel. The high speed camera is synchronized with the laser pulsations and the pulses are separated by a time Δt with a period T between each double pulsation. T and Δt are often limited by the camera. The laser light is scattered off the particles and hits the camera's CCD sensor.

The signal is processed by a computer, often using spatial correlation techniques. As a

result the parameter Δt is considered more important than T. The particles are assumed to follow the acoustic movement and are recorded by two principal parameters. In terms of camera resolution, the most important parameter is the number of pixels N_p provided by the sensor. A high number of pixels may give high spatial accuracy.

The second parameter depends on the camera's dynamics and measure the intensity of light scattered off the particles. Seeding particles are needed to obtain images and it is assumed that the particles follow the acoustic wave perfectly [12]. Using PIV to measure sound fields does however present some limitations as most measurements are for frequencies up to 2 kHz.

This setup remains somewhat cumbersome, needing high speed camera, laser lighting and seeding particles. These factors limits the uses of this particular method for acoustic detection. These components also comes with a certain cost, both monetary and computational.

1.4 Laser Doppler Velocimetry Applied to Acoustics

Laser Doppler Velocimetry (LDV) and Laser Doppler Anemometry (LDA) are well established techniques for measuring the velocity of objects, surface reliefs and fluids. Campbell et al [17] provides an extensive review of using lasers to measure sound, and he treats subjects ranging from PIV to the acousto-optic effect which measures the change of refractive index of air due to acoustic waves. The topics regarding PIV and LDV/LDA are later discussed and summarized by Valière et al [12], [18]. They propose using an LDV to directly measure the movement of particles entrained by sound waves.

These methods provides us with acoustic measurements in places where traditional microphones may not suffice. Typical subjects of measurement could be boundary areas, where placing a microphone would distort the sound field, in inhomogeneous media and in the close field of an acoustic source. This section will treat the basic principles of acoustic detection using lasers. First the measurement of particle entrainment using LDV is presented and the method's operating principles are outlined. Then measurements of the variations in refractive index through the acousto-optic effect are discussed. First up is the acoustic measurements made by LDV applied to particle entrainment.

1.4.1 Measurement of Particle Entrainment by LDV

Particle entrainment is subjected to research especially in industries where aerosol is produced in large quantities. A typical example would be a combustion plant where large

quantities of material is burned and exhaust such as ash escapes through a chimney. These industries have implemented extensive measures to reduce air pollution. Thomas L. Hoffmann [19] in 2000 and E. Riera in 2015 proposed agglomeration of aerosol through acoustic injection in the escape ducts as a mean for reducing pollution. Larger particles are captured more easily by filters. Several numerical and experimental studies has been conducted on the movement of aerosol entrained by acoustic waves [20]–[23]. These and similar findings combined with LDV/LDA measurements would be of great interest to the industry for measuring and assessing pollution, and reducing emissions.

1.4.1.1 Introduction

The first method of LDV applied to acoustics dates back to to 1976 where K. J. Taylor [24] used a Laser Dopper system to measure the movement of particles in a sound field. The principle is straight forward: A particle or aerosol is suspended in air (or another liquid or gaseous medium) or moves with a flux. When an acoustic wave pass through the medium, the particle is entrained by the acoustic wave and it's velocity is modulated. Using an LDV, the movement of the particle is captured and information of the acoustic wave is extracted. The area from which the LDV records it's signal is called the detection volume or probe volume (PV). Due to it's small size, it can be used to generate very high resolution measurements when displaced throughout a volume.

In early experiments different types of smoke were used to create aerosol [24], and being the good old days the researchers found that "tobacco smoke was the most useful". They reasoned that the information available on the cigarette smoke's particle size distribution made it the best choice. Having their cigarettes payed for by the lab and smoking at work probably had nothing to with the choice of aerosol.

Several papers have been published developing the subject of LDV and LDA in acoustics. Taylor [25] published in 1981 a calibration method for microphones using LDV. In 1986 Davis and Huges-Taylor [26] measured complex acoustic impedances. In 1991 Vignola et al [27] used an LDV to measure standing waves in water. The same year Eckman et al [28] estimated acoustic velocity of particles in an oscillatory flow. Later, in 1997 Valeau [29] published new approaches for calculating instantaneous frequencies in an LDV signal. In 2000, Valière et al [18] published a paper dedicated to acoustic measurements in air using commercial available LDV equipment, and published again in 2014 a comprehensive document on LDV for acoustics [12].

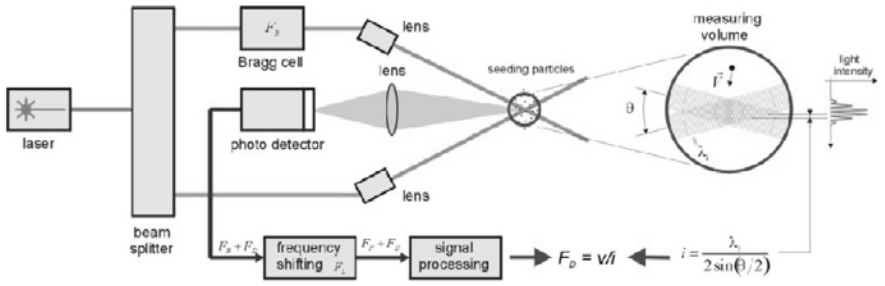

Figure 1.7: Typical LDV setup [12]

1.4.1.2 Operating Principles

Figure 1.7 shows a typical LDV setup for use in particle detection and anemometry. A laser beam is split in two and the resulting coherent beams are focused at a position in space. The volume where the two beams cross each other is called the detection volume or Probe Volume (PV). Inside the PV the interference between the two beams create light and dark zones as shown in Fig. 1.8. When an aerosol or seeding particle crosses the PV, some light is backscattered onto a photodetector creating an oscillating signal. The distance between the light and dark zones is denoted i and is used to calculate the velocity of a particle traversing the PV. The oscillation of the detected signal is proportional to the velocity of the particle. The frequency of the oscillation can be expressed as

$$f_d = \frac{2\sin(\theta)V_x}{\lambda} = \frac{V_x}{i} \tag{1.6}$$

where θ is the angle between the beams and λ si the wavelength. V_x is the particle velocity in the x-direction and i is the fringe space.

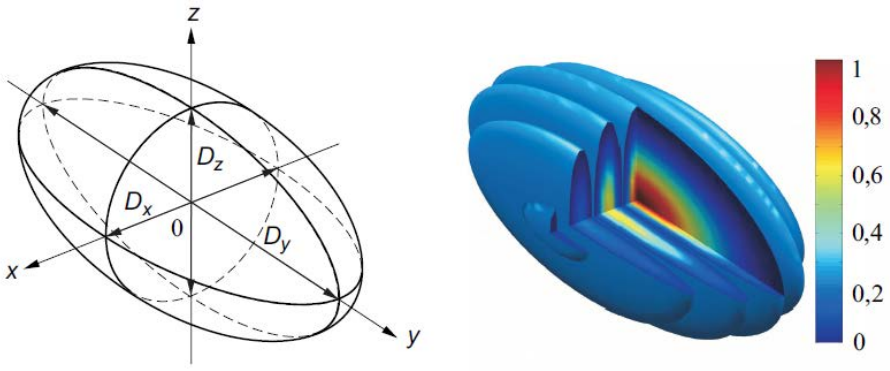

Figure 1.8: Probe volume interferences [30]

The dimensions of the PV can be expressed as

$$D_d = \frac{4\lambda f_l}{\pi d_1} = D_z \qquad D_x = \frac{D_d}{\cos(\theta/2)} \qquad D_y = \frac{D_d}{\sin(\theta/2)} \tag{1.7}$$

Here f_l is the beams focal length and d_l is the beam width at emission.

Due to the movement of the particle, the backscattered light will be Doppler shifted, and each of the interfering beams will have it's own Doppler shift. Equation (1.6) can be found by considering the Doppler shift of the light [31].

Suppose the two laser beams enter the PV from directions $\vec{k}_1$ and $\vec{k}_2$. An electric field being reflected off a particle traversing the PV can be expressed by

$$E = E_0 \exp(\vec{k}_1 - \vec{k}_0) \cdot \vec{s} + E_0 \exp(\vec{k}_2 - \vec{k}_0) \cdot \vec{s} \tag{1.8}$$

where $\vec{k}_0$ is the direction of observation and $\vec{s}$ is the displacement vector. Here the $\cdot$ meas scalar product. The photodetected signal is proportional to the square modulus of the field

$$I \propto |E|^2 \tag{1.9}$$

where I is the intensity. Developing this expression gives

$$I \propto 2E_0^2 + 2E_0^2 \cos\left([\vec{k}_1 - \vec{k}_0] \cdot \vec{s} - [\vec{k}_2 - \vec{k}_0] \cdot \vec{s}\right) \tag{1.10}$$

$$= 2E_0^2 \left[1 + \cos\left((\vec{k}_1 - \vec{k}_2) \cdot \vec{s}\right)\right] \tag{1.11}$$

As we see, the final result does not depend on the vector of observation $\vec{k}_0$. The signal thus depends on the vector difference $\vec{k}_1 - \vec{k}_2$. Taking the modulus gives us

$$|\vec{k}_1 - \vec{k}_2| = 2k \sin(\theta) \tag{1.12}$$

Where θ is the incident angle of the beams. If a particle travels in-plane, parallel to the x-axis, the phase of the cosine function can is expressed $phi = (\vec{k}_1 + \vec{k}_2) \cdot \vec{s} = 2ks \sin(\theta)$. The angular frequency $\omega = 2\pi f$ is found by time differentiating the phase shift ϕ.

$$f_d = \frac{1}{2\pi}\frac{d\phi}{dt} = \frac{1}{2\pi} 2k \frac{ds}{dt} \sin(\theta) = \frac{2V_x \sin(\theta)}{\lambda} \tag{1.13}$$

Which is equal to Eq. (1.6).

If we suppose that a particle with constant velocity V_x traverse the PV along the x-axis perpendicular to the fringes, the photodetector will capture a signal with the following

form [12]

$$P(t) = GI_r \, \mathrm{e}^{-(V_x t/D_x)^2}(L + \cos(2\pi f_d t)) \tag{1.14}$$

Where G is the gain from the photodetector and I_r is the intensity of the backscattered light. The pedestal L is the always positive level of magnitude around which the Doppler signal oscillates as shown in Fig. 1.9.

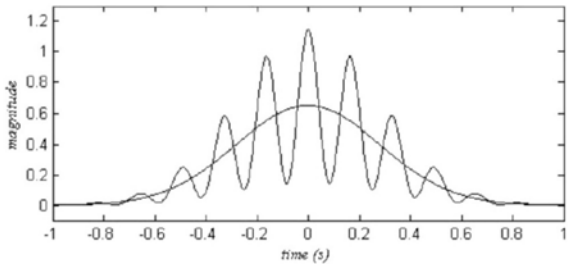

Figure 1.9: Doppler burst from eq.(1.14) [12]

The use of a Bragg cell enables us to discern the direction of the particle crossing the PV. A Bragg cell is a device that can shift the frequency of a laser beam by a known value f_{ref} called the Bragg frequency, often set to 40 MHz. A cell is inserted into one of the beams, shifting it's frequency by $f_{\mathrm{ref}} = 40$ MHz so that the interference pattern moves with constant speed. The signal captured by the photodetector takes on a new form

$$P(t) = GI_r \, \mathrm{e}^{-(V_x t/D_x)^2}[L + \cos(2\pi(f_d + f_{\mathrm{ref}})t)] \tag{1.15}$$

$$= GI_r \, \mathrm{e}^{-(V_x t/D_x)^2}[L + \cos(2\pi(V_x/i + f_{\mathrm{ref}})t)] \tag{1.16}$$

where we recognize that if the particle velocity is positive, $V_x > 0$, the interferometer will detect a frequency superior to the reference frequency, $f_{\mathrm{det}} > f_{\mathrm{ref}}$, and vice versa.

1.4.1.3 Signal Acquisition and Treatment

Let's consider the case of a constant flow of particles with velocity V_x. The treatment has to be adapted according to the magnitude of V_x. At low velocities the particles may spend a longer time inside the detection volume. However we may observe a lower Doppler frequency f_d that approaches the Bragg frequency f_{ref} discussed in the previous section. On the other hand, at high velocities, f_d is easily separated from f_{ref} but the time passed in the detection volume is relatively short. These two situations will have an impact on the precision of the resulting calculations.

The first step of retrieving the acoustic signal is a burst detection where a particle crosses the detection volume. Various signal processing schemes are applied to the signal

in order to retrieve the movement information. In one of their latest papers Le Duff et al [32] applied an extended Kalman Filter to facilitate the demodulation of their photodetected signal. Such filters however, needs an *a priori* information of the phenomenon in question as input in order to work.

An easier method is to perform a short time frequency analysis on the Doppler signal/burst. Such methods can either be correlation based or Fourier Transform based. Due to the Gaussian character of the laser beam, the Doppler burst are usually weighed by a Gaussian shaped window on the form

$$w(t) = \mathrm{e}^{-(V_x t/D_x)^2} \tag{1.17}$$

The correlation based methods is used to find the periodicity of the change in Doppler frequency whereas the Fourier transformation based method calculate the instantaneous frequency that shift in time with the acoustic pressure wave. The drawback of these methods is often the low signal to noise ratio, making demodulation tricky.

1.4.2 Acousto-Optic Effect: Measuring the Refractive Index of Air

The acousto-optic effect has been a known phenomenon for several decades and an application was outlined in Scurby's 1991 book on laser ultrasonics [33]. A direct measurement of a passing acoustic wave, through the oscillating change in refractive index of air, implies that the phenomenon can be used as a non-contact, non-invasive acoustic measurement scheme. Non-contact acoustic sensing schemes such as anemometric measurements has limitations in detection frequency [12], [18], [24]. Other setups such as Schlieren photography [34] or PIV are cumbersome and need recording devices such as high speed cameras. Characterization of sound fields without perturbing them is complicated, and the resolution of the measurements usually depends on the number of acquisition devices employed. By using laser interferometers one can examine acoustic fields without the need for microphone arrays and high speed cameras. Direct measurements of the refractive index change enables us to reconstruct the acoustic signal, without perturbing the wave.

1.4.2.1 Introduction

In 1993, X. Jia et al [35] used a laser interferometer to record ultrasonic waves by measuring the change in refractive index in air inside the waves. Since then, development has continued at a steady pace, and in 2001 Remenieras et al [36] applied tomographic recon-

struction to their data in order to create 2D images of the sound field. Zipster et al [37]–[39] proposed a simple interpretation of the phenomenon and coined the term refracto vibrometry. Zipster et al confined sound waves between a rigid transparent barrier and a reflective backplane. Using this method, the sound wave made the reflective surface appear as a simple vibrating surface. Malkin et al [40] devised in 2014 a simple method for 2D imaging of acoustic fields using acousto-optic effect, and Mbailassem et al [41] used a similar method in 2018 to analyze acoustical properties of irregular cavities. Several advances has been made on the topic in regards to Optical Feedback Interferometry. These advances will be discussed in section 1.6

1.4.2.2 Operating Principles

The systems used to measure the acousto-optic effect essentially measure the change in refractive index. The change happens as sound waves compress and decompress the medium through which they travel (typically air). To build up an understanding of how to measure this effect, let us consider a basic Mach–Zehnder Doppler interferometer like the one in Fig. 1.10. In this device a laser beam is split and one half goes through a frequency modulator, typically a Bragg cell as discussed in section 1.4.1.2, and then onto a detector. The other half travels to some distant target. The beam is reflected from the distant target and onto a detector where it joins (interferes with) the beam that was modulated by the Bragg cell. In Fig. 1.10, f_s is the emission frequency, Δf is the frequency shift due to the movement of the target and f_B is the Bragg frequency.

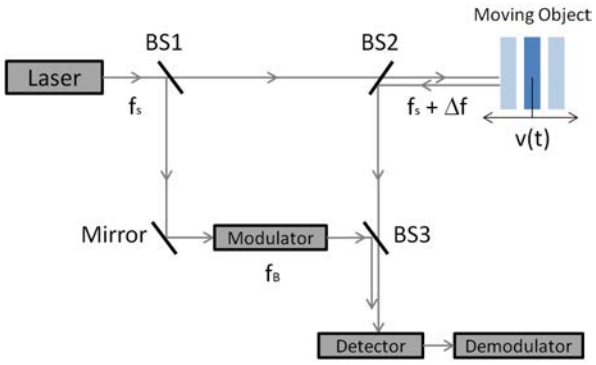

Figure 1.10: Schema of LDV setup with a Mach–Zehnder Doppler interferometer

The beam intensity detected by the photo-detector can be expressed [3] as follows

$$I = I_0 + I_r + 2\sqrt{I_r I_0}\cos(\Delta\beta) \tag{1.18}$$

where I_0 is the incident beam and I_r is the reference beam. $\Delta\beta$ is the difference in phase

between the two, and can be expressed as

$$\Delta\beta = \frac{2\pi}{\lambda}(l_r - l_0) \tag{1.19}$$

where λ is the vacuum wavelength of the reference laser beam, l_r is the optical path length of the reference beam, which is constant, and l_0 is the optical path length of the measurement beam. Since l_0 is the optical path length, it can be expressed through

$$l_0 = \int_0^L n(x, y, z, t)dl \tag{1.20}$$

where L is the absolute distance to the target and $n(x, y, z, t)$ is the refractive index along the optical path. As we have seen in Section 1.4.1.2, a movement of the target will induce a shift in the beat frequency recorded by the sensor. Intuitively, if the target distance is fixed and we vary $n(x, y, z, t)$ instead, we will see a variation in the beat frequency as if l_0 was altered. Figure. 1.11 shows an example of how an LDV system could be implemented to record acoustic fields. An acoustic source is placed between a reflector and the LDV. As the acoustic wave pass through the laser beam, the index of refraction is altered and the LDV "sees" this as a change in l_0.

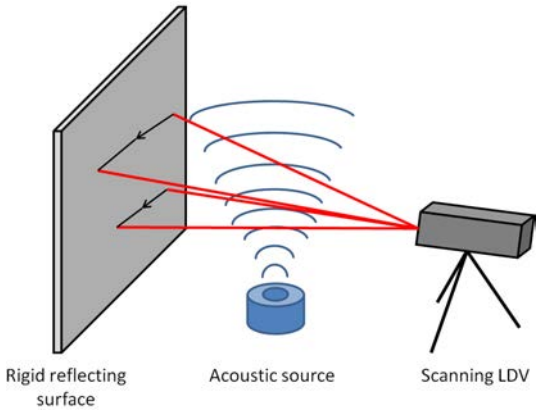

Figure 1.11: Schematic of an LDV scanning a reflective surface where acoustic waves alter the refractive index of the optical path

The LDV is a point measurement device, so in order to reconstruct the acoustic field, a scan has to be preformed. What we obtain is the 2D image of the three dimensional wave that propagates from the acoustic source. Other ways to reconstruct the acoustic field using a point measurement is to displace the laser around the acoustic source, or to displace the source. This would give us a complete profile of the acoustic field, scanned from all directions and altitudes.

Figure 1.12 shows one of the experimental results from Zipster et al [39] who recon-

structed ultrasound wave patterns that where trapped between a reflector and a glass plate. On the left is a schema of their experiment and on the right is a plot of the reconstructed acoustic field. When using an SLDV to scan a free field acoustic wave, the number of acoustic wave fronts traversed by the laser beam depends on the direction in which the laser points. By confining the acoustic wave, Zipster et al omitted this problem. Malkin et al [40] however, took into account this effect in their 2014 paper and provided a technique to scan an unconfined propagating acoustic field. Oikawa et al [42] made 3D

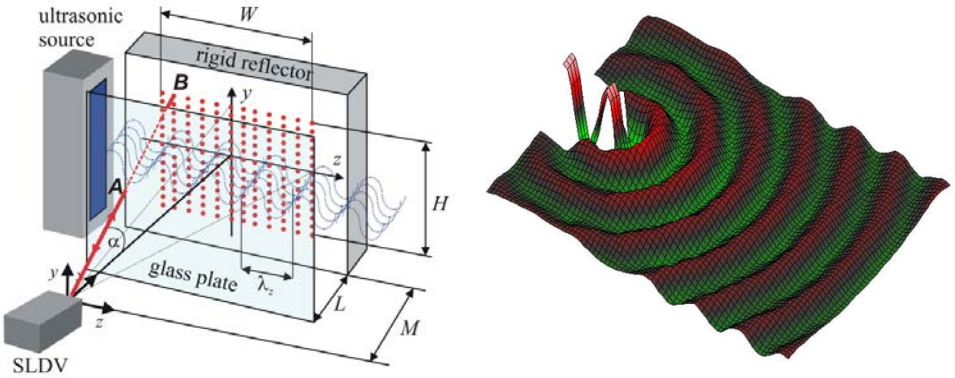

Figure 1.12: Schematic of experimental setup of SLDV (left) used to map a 40 kHz ultrasound and reconstructed 2D sound field (right) [39]

projections of sound fields already back in 2005. They placed an acoustic source pointing upwards, on a disk allowing them to turn the speaker around. Working with and LDV in an anechoic chamber they were able to scan the sound field and reconstruct 3D images using Computed Tomography (CT) techniques. One of the results is shown in Fig. 1.13.

1.4.2.3 Conclusion

Laser Doppler Interferometry has been applied to the measurement of sound fields. In principle, the LDV measure the change in optical path through the change in refractive index associated with an acoustic pressure wave. Different techniques has been proposed and today 2D and 3D images of the sound fields are produced. In order to construct 3D images of the sound field, tomographic signal processing methods are applied to the signals.

1.5 Optical Feedback Interferometry: Principles of Operation

Optical Feedback Inerferometry (OFI) is a well established non-contact measurement scheme with numerous areas of application. OFI is used for displacement measurements

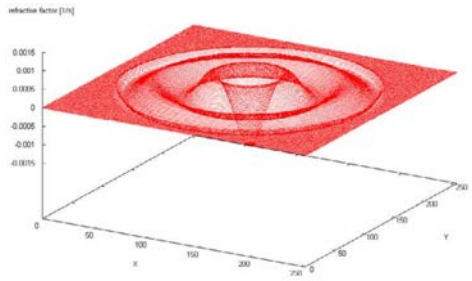

Figure 1.13: 3D reconstruction of sound field using an LDV and computed tomography [42]

such as vibrometry and velocimetry [43]–[47] and today picometric displacements are recorded using this sensing scheme [48], [49]. OFI is applied to other areas such as flow measurement [50]–[53], in particular in vivo measurements [54], [55] and absolute distance measurements [56]–[58]. Lately the sensing scheme has been applied to acoustic measurements through the acousto-optic effect, where substantial effort has been made by Urgiles et al [3], [59]–[61] to advance the subject. The first comprehensive modeling and measurement of the acousto-optic effect was however made by Bertling et al [1], opening the door to the acoustic domain using OFI sensors.

Optical Feedback Interferometry carries several advantages as a measurement scheme compared to other interferometric techniques. In OFI the laser itself acts as light source and detector at once, eliminating several elements needed in other interferometry sensing schemes. No need for beam splitters, optical fibers, brag cells or other expensive and often cumbersome units. A typical detector often needs as little as a single collimating lens, making it very compact. A suitable of-the-shelf laser can be acquired for relatively low cost (we use lasers ranging from $30\$ - 70\$$), and needs only a few electronic components to operate. In short, an OFI detector's size, price and simplicity combined with high precision makes it an excellent tool for non-contact measurements and acoustic measurements.

In this section the operating principles of the OFI sensing scheme are laid out. We will start by considering the free running laser and a propagating laser beam in free space. From there we will consider a reflected beam coming back from a distant target, and we will see how the laser is affected. These components are used to build a model of the interferometric system. Over the course of this section we will discuss the different parameters impacting the OFI measurement system in order to complete the model. The resulting Laser Power formula can be used to model and predict the behavior of the OFI sensing scheme as it is applied to different measurement configurations.

1.5.1 The Free Running Laser

Before diving into the physics of a semiconductor laser subjected to optical feedback, it can be very useful to look at the free running laser first. A schema of a Fabry-Perot laser cavity is presented in fig. 1.21. This laser consists of two facets, M_1 and M_2, with reflectivity coefficients r_1 and r_2 respectively. In between the two mirrors we find the gain medium of length l_c, where stimulated emission takes place [62].

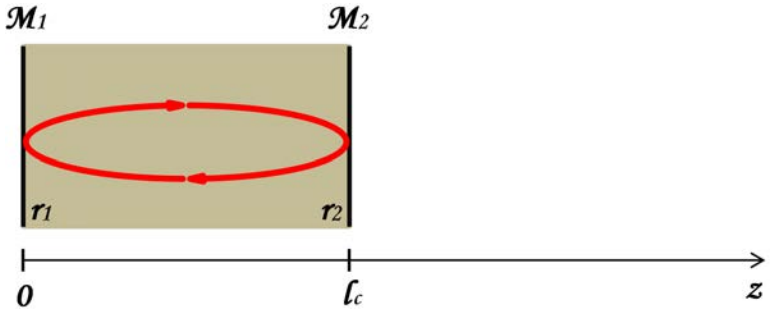

Figure 1.14: Schema of Fabry-Perot Laser Cavity

The forward propagating field in the z direction can be described by

$$E(z) = E_0 \, \mathrm{e}^{-jk_0 z} \mathrm{e}^{-\frac{1}{2}\gamma_0 z} \tag{1.21}$$

where $\gamma_0 = g - \alpha_\mathrm{p}$. Here, g is laser medium gain α_p is power loss due to losses in the cavity and k_0 is the wavenumber [63].

$$k_0 = \frac{2\pi}{\lambda} \quad \text{and} \quad \lambda = \frac{c}{\nu_0 n_\mathrm{eff}} \tag{1.22}$$

where c is the speed of light, λ is the laser's nominal wavelength, ν_0 is the mode and n_eff is the effective refractive index in the laser gain medium. In equation 1.21 the first exponent represents the unattenuated wave propagation and the second exponential term accounts for losses. The laser is constructed so that after a round trip time in the cavity, the electric field E_1 must be identical to E_0 in terms of phase and amplitude. The lasing condition is reached when the gain equals the losses after one round trip in the laser cavity. The field after a round trip time can be expressed as

$$E_1 = E_0 r_1 \, \mathrm{e}^{-jk_0 l_\mathrm{c}} \mathrm{e}^{-\frac{1}{2}\gamma_0 l_\mathrm{c}} r_2 \, \mathrm{e}^{-jk_0 l_\mathrm{c}} \mathrm{e}^{-\frac{1}{2}\gamma_0 l_\mathrm{c}} \tag{1.23}$$

resulting in

$$1 = r_1 r_2 \, \mathrm{e}^{-2jk_0 l_\mathrm{c}} \mathrm{e}^{-\gamma_0 l_\mathrm{c}} \tag{1.24}$$

and

$$\nu_0 = M\frac{c}{2l_c n_{\text{eff}}} \text{ with } M = 1, 2, 3, ... \tag{1.25}$$

where M is an integer. In eq. (1.23), the terms in the two last exponentials becomes negative as l_c changes its sign being the backwards running beam.

The threshold gain is found by solving the real part of eq.(1.24):

$$g_{th} = \alpha_p - \frac{\ln(r_1 r_2)}{l_c} \tag{1.26}$$

Equations (1.25) and (1.26) are the threshold conditions, meaning the necessary conditions for the laser to lase.

1.5.2 External Cavity Feedback

The three mirror model, depicted in fig. 1.15 is commonly used to describe the laser physics while undergoing optical feedback. The model adds an external cavity to the system, with length l_{ext}, delimited by the laser front facet M_2 and the target M_3 with reflectivities r_2 and r_3 respectively.

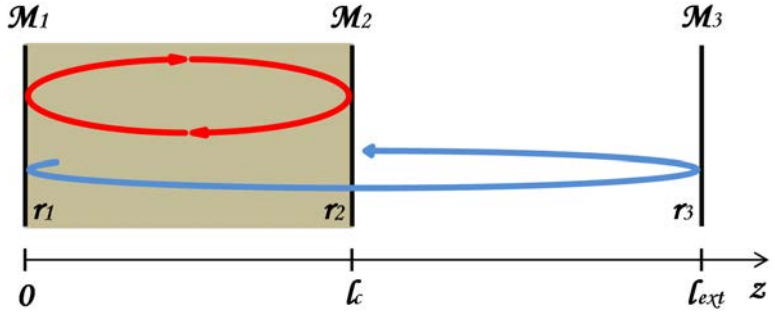

Figure 1.15: Schema of Fabry-Perot Laser Cavity with external feedback

When the laser described in section 1.5.1 reaches threshold, it starts to lase and a part of the emitted beam is reflected back into the laser where it couples with the lasing mode, as shown by the blue arrow in Fig. 1.15. The propagation equation for the free running laser, eq. (1.21) can be rewritten to contain the reflected electric field after optical feedback:

$$E_1 = E_0 r_1 r_2 \, \mathrm{e}^{-2jk_0 l_c - \gamma_0 l_c} + E_0 r_1 (1 - r_2^2) r_{\text{ext}} \, \mathrm{e}^{-2jk_F l_{\text{ext}}} \tag{1.27}$$

We recognize r_{ext} as the reflection coefficient from the target. $r_{\text{ext}} = r_3 \, \alpha_{p\,\text{ext}} \, f$ where r_3 is the target's reflectivity, $\alpha_{p\,\text{ext}}$ is the reflected field's attenuation and f is the fraction of light coherently coupled back into the laser [64]. When $r_{ext} << r_2$ we can neglect multiple

Figure 1.16: Schema of Fabry-Perot Laser Cavity, Equivalent Mirror Model

round trips [65]. Thus the threshold condition expressed in eq. (1.24) can be rewritten to

$$1 = r_1 r_2 \, \mathrm{e}^{-2jk_0 l_\mathrm{c} - \gamma_0 l_\mathrm{c}} + r_1 (1 - r_2^2) r_\mathrm{ext} \, \mathrm{e}^{-2jk_\mathrm{F} l_\mathrm{ext}} \tag{1.28}$$

which can be rewritten to

$$1 = r_1 r_2 \, \mathrm{e}^{-2jk_0 l_\mathrm{c} - \gamma_0 l_\mathrm{c}} \left[1 + \frac{r_\mathrm{ext}}{r_2} (1 - r_2^2) \, \mathrm{e}^{-2jk_\mathrm{F} l_\mathrm{ext}} \right] \tag{1.29}$$

where k_F is the external cavity wavenumber under feedback.

The three mirror model can be simplified by combining the front laser facet and the target into one equivalent mirror M_eq with reflectivity r_eq as shown in Fig. 1.16. The cavity distance between M_1 and M_eq becomes l_eq and can the reflectivity r_eq be written [65], [66]:

$$r_\mathrm{eq} = r_2 \left[1 + \xi \, \mathrm{e}^{-2jk_\mathrm{F} l_\mathrm{ext}} \right] \tag{1.30}$$

where ξ is recognized [62], [63] as

$$\xi = \frac{r_\mathrm{ext}}{r_2} (1 - r_2^2) \tag{1.31}$$

Following eq. (1.22), the exponential term in eq. (1.30) can be rewritten to

$$r_\mathrm{eq} = r_2 \left[1 + \xi \, \mathrm{e}^{-j2\pi\nu_\mathrm{F} \cdot \tau_\mathrm{ext}} \right] \tag{1.32}$$

where

$$\boxed{2\pi\nu_\mathrm{F} \cdot \tau_\mathrm{ext} = \phi_\mathrm{F} \quad \text{and} \quad \tau_\mathrm{ext} = \frac{2n_\mathrm{ext} l_\mathrm{ext}}{c}} \tag{1.33}$$

We recognize τ_ext as the round trip time for a photon in the external cavity, n_ext the refractive index of the propagation medium (usually air) and ν_F as the stable laser mode

when subjected to feedback. The lasing condition under feedback becomes

$$1 = r_1 r_{\text{eq}}\, \mathrm{e}^{-j2\pi\nu_{\text{F}}\cdot\tau_{\text{in}}}\, \mathrm{e}^{\gamma_{\text{F}} l_{\text{c}}} \tag{1.34}$$

where τ_{in} is the round trip time of a photon in the internal laser cavity

$$\tau_{\text{in}} = \frac{2n_{\text{eff}} l_{\text{c}}}{c} \tag{1.35}$$

and γ_{F} are losses in the external cavity. The phase change $\Delta\Phi$ of the laser after a round trip in the external cavity is well documented in the literature [58], [67], [68] and is expressed as

$$\Delta\Phi = \nu_{\text{F}} - \nu_0 + \frac{C}{2\pi\tau_{\text{ext}}} \sin(2\pi\nu_{\text{F}}\tau_{\text{ext}} + \arctan\alpha) \tag{1.36}$$

where α is the linewidth enhancement factor [67], [69] and C is the feedback parameter [67]

$$\boxed{C = \xi \frac{\tau_{\text{ext}}}{\tau_{\text{in}}} \sqrt{1+\alpha}} \tag{1.37}$$

The linewidth enhancement factor α essentially relates the laser phase change to its gain and is defined as the ratio between the real and imaginary part of the laser's refractive index. The feedback parameter C impacts the dynamics of the laser when it undergoes feedback and depends on the target reflectivity and distance. The phase change in eq.(1.36) should be equal to $M2\pi$ (where $M = 0, 1, 2, 3, ...$) to satisfy the laser operating condition. Assuming absence of multiple reflections, the laser frequency under feedback ν_{F} can be expressed as

$$\boxed{\nu_{\text{F}} = \nu_0 - \frac{C}{2\pi\tau_{\text{ext}}} \sin(2\pi\nu_{\text{F}}\tau_{\text{ext}} + \arctan\alpha)} \tag{1.38}$$

In many applications when measuring the laser signal we use the photodiode placed in the back of the laser packaging. The diode provides an image of the laser power by capturing the photons escaping through the laser's back facet. An expression of the laser power may be expressed through the equations derived by Lang and Kobayachi [70].

The laser rate equations under feedback [47], [63], [67], [70] can be written

$$\frac{\mathrm{d}E}{\mathrm{d}t} = \frac{1}{2}[G_N(N_c - N_0) - \frac{1}{\tau_{\text{p}}}]E + \frac{\xi}{\tau_{\text{ext}}} \cos[2\pi\nu_{\text{F}} + \phi(t) - \phi(t - \tau_{\text{ext}})] \tag{1.39}$$

and

$$\frac{\mathrm{d}N_c}{\mathrm{d}t} = \frac{J\eta}{e\Lambda} - \frac{N_c}{\tau_{\text{c}}} - G_N(N_c - N_0)E_0^2(t)\ . \tag{1.40}$$

Adding to our repertoire of τ's, we recognize τ_{p} and τ_{c} as the photon and carrier lifetimes respectively. Furthermore we recognize G_N as the stimulated emission gain factor, N_c

as the carrier density and N_0 as the inversion carrier density. η is the internal quantum efficiency, J is the density of the pumping current, Λ is the active layer thickness and e is the electron charge.

Under feedback the laser threshold gain g is shifted a quantity Δg [62], [65], [67]. The threshold gain is the gain where stimulated emission of photons exceeds the losses in the cavity and the lasing condition is achieved. The threshold current I_{th} is also shifted by a small amount ΔI_{th}.

$$\Delta g_{\mathrm{th}} = g'_{\mathrm{th}} - g_{\mathrm{th}} = -\frac{\xi}{l_{\mathrm{ext}}}\cos(\phi_{\mathrm{F}}) \tag{1.41}$$

where g'_{th} is the threshold gain under feedback. The change in injection current is

$$\Delta I_{\mathrm{th}} = \frac{eV_m}{T_s\kappa\Gamma}\Delta g_{\mathrm{th}} \tag{1.42}$$

where V_m is the volume of the active gain medium, T_s the rate of spontaneous recombination, Γ is the mode confinement factor, and the differential gain at threshold is denoted by κ.

The laser power can be calculated in several ways. Wang *et al* [65] derives the power from the laser intensity and show that the laser power depends both the intensity of the feedback, and on the spectral distribution of the laser diode under feedback. Coldren *et al* [71] obtains the laser power under feedback P_{F} from the laser current which can be expressed the following way

$$P_{\mathrm{F}} = \frac{\eta h\nu[I - (I_{\mathrm{th}} + \Delta I_{\mathrm{th}})]}{e} \tag{1.43}$$

Where h is Planck's constant. Putting in the expressions for ΔI_{th} and Δg_{th} we obtain

$$P_{\mathrm{F}} = \frac{\eta h\nu(I - I_{\mathrm{th}})}{e}\left[1 + \frac{eV\xi}{T_s\kappa\Gamma l_{\mathrm{ext}}(I - I_{\mathrm{th}})}\cos(\phi_{\mathrm{F}})\right] \tag{1.44}$$

This equation can be simplified, and we recognize the laser power equation as often found in the literature [72]

$$\boxed{P_{\mathrm{F}} = P_0[1 + m\cos(\phi_{\mathrm{F}})]} \tag{1.45}$$

where P_{F} is the power under feedback, P_0 is the nominal laser power without feedback and m is a modulation index that influence the amplitude and shape of the interferometric fringes.

$$m = C \times \frac{2\tau_{\mathrm{p}}c}{l_{\mathrm{ext}}\sqrt{1+\alpha^2}} \tag{1.46}$$

m depends mainly on two factors, the target reflectivity r_{ext} and the external cavity length l_{ext} which also can be expressed through the round-trip time τ_{ext}. We remember that the feedback quality parameter C from eq. (1.37) is expressed as

$$C = \frac{r_{\text{ext}}}{r_2}(1 - r_2^2) \times \frac{\tau_{\text{ext}}}{\tau_{\text{in}}}\sqrt{1+\alpha}$$

where we recognize ξ from eq. (1.31)

$$\xi = \frac{r_{\text{ext}}}{r_2}(1 - r_2^2)$$

Taking this into account we can rewrite m to

$$m = 4\xi\frac{\tau_{\text{p}}}{\tau_{\text{ext}}} \tag{1.47}$$

These equations sum up the main parameters necessary to accurately model Optical Feedback Interferometry. In most OFI applications we measure the oscillations of optical power through the laser's in-package photo diode. Other methods to measure the feedback is to measure the laser's terminal voltage or by measuring the laser frequency directly. The latter method requires an increased number of optical elements to function but provides measurements down to a few pm **donati_self-mixing_2018\IeC {\‘a}**, [48]. The frequency of the laser power oscillations, measured by the photo diode, tells us about the movement of the target, and the shape and amplitude of the signal tells us about the optical conditions. In the following sections we discuss some OFI system's behaviors when applied to different measurement situations.

1.5.3 OFI Measurement configurations

1.5.3.1 Vibrating Target Measurements

The Optical Feedback Interferometer is very versatile and is often used as a velocimeter or vibrometer. In the simplest of system configurations, shown in Figure 1.17, the laser points on a target that is moving along the optical axis. The target movement with velocity v will modify the external cavity length l_{ext} and with this in mind we can modify the laser Power Equation:

$$P_{\text{F}} = P_0\left[1 + m\cos(2\pi\nu_{\text{F}}\frac{2(l_{\text{ext}} + vt)}{c})\right] \tag{1.48}$$

where t is time and c is the speed of light. When the target moves, the expression inside the cos evolves, which has an impact on the laser power P. The resulting power oscillation

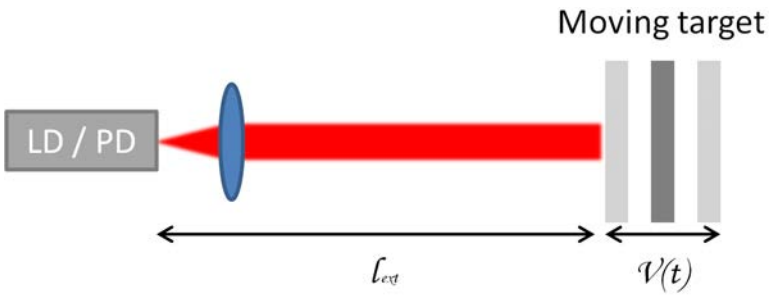

Figure 1.17: OFI Velicometer: Schema of single moving target scattering. The target is moving along the optical axis.

contains fringes which gives us information about the movement of the target. A fringe, such as those shown in Fig 1.18 will appear for each displacement of half a laser wavelength, $\lambda/2$. Thus by counting the appearance of fringes in time we can estimate the velocity of the target. The number of fringes counted gives us the distance the target moved. Figure 1.18 shows a simulation[1] of a laser power response where the laser measures a vibrating surface. As the target moves back and fort the fringes switch orientation; when the target moves away from the target, the fringes lean towards the right, and vice-versa when the target approaches the laser.

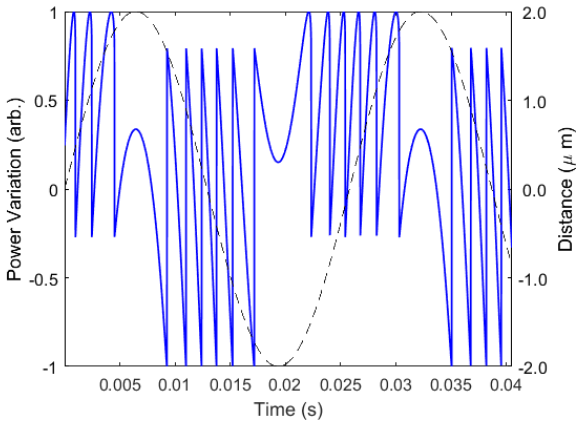

Figure 1.18: Simulation of laser signal (blue line). The laser measures a target moving sinusoidally with frequency of 40 Hz and amplitude 2 μm zero to peak (black line). $C = 2.5$ and $l_{\text{ext}} = 30$cm

In principle, the simplest technique is to count fringes in order to acquire information of the target movement. If the signal is noisy or degraded, as is often the case, other

[1]Using Kliese et al's numerical algorithm [68], which is explained in detail in chapter 2, Section 2.2.

techniques such as frequency analysis [73], [74] may give a better estimation of the velocity and displacement of a target.

1.5.3.2 Translating Target Measurements

A widely used velocimeter configuration is presented in Fig. 1.19. In this configuration the distance between the laser and a target surface is fixed but there is a relative translational displacement between the two.

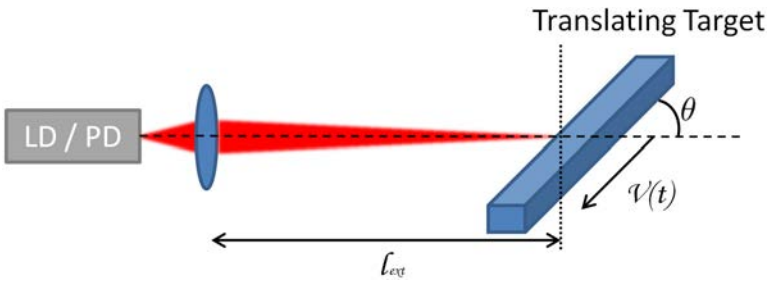

Figure 1.19: OFI Velocimeter: Schema of translating moving target scattering. The target is moving at an angle θ to the beam axis.

When the laser is pointing on a translating target, l_{ext} remains constant but we still observe fringes in the laser signal. This is due to the Doppler shift of the returning light, that is frequency shifted after reflection. For a target of constant velocity $v(t)$ the frequency of the appearing fringes can be calculated through

$$\boxed{f_{\text{D}} = \frac{2v\cos(\theta)}{\lambda}} \tag{1.49}$$

f_{D} is called the Doppler frequency, but is in reality a beat frequency that appears due to the difference between the lasing mode, and the Doppler shifted frequency of the returning photons. The angle θ is the incident angle between the laser and the direction of the moving target and λ is the laser wavelength. The Doppler shifted light impacts the Power Equation by adding another phase term [51].

$$\boxed{P_{\text{F}} = P_0[1 + m\cos(\omega_{\text{D}}t + \phi_{\text{D}})]} \tag{1.50}$$

The term ω_{D} contains the emission frequency ν_{F} which is slightly shifted due to the Doppler effect.

$$\omega_{\text{D}} = 2\pi\nu_{\text{F}}\frac{-2\,v\cos(\theta)}{c + v\cos(\theta)} = 2\pi f_{\text{D}} \tag{1.51}$$

where $\frac{-2\,v\cos(\theta)}{c+v\cos(\theta)}$ is the amount the emission frequency is shifted [51]. The phase term ϕ_{D} is added to account for the phase accumulated by the returning Doppler shifted photons

$$\phi_{\mathrm{D}} = 2\pi\nu_{\mathrm{F}}\left(1+\frac{c-v\cos(\theta)}{c+v\cos(\theta)}\right)\frac{\tau_{\mathrm{ext}}}{2} \tag{1.52}$$

where c is the speed of light. The emission frequency ν_{F} can be calculated taking into account the Doppler shift, giving

$$\nu_{\mathrm{F}} = \nu_0 - \frac{C}{2\pi\tau_{\mathrm{ext}}}\sin(2\pi\nu_{\mathrm{F}}t + \phi_{\mathrm{D}} + \arctan\alpha) \tag{1.53}$$

The configuration in shown in Figure 1.19 is one of the most widely used interferometric setups for velocimetry measurements and can be used to measure the velocity of almost any moving or rotating target. With the Power Equation, eq. (1.50), the measurement method can be extended to measure multiple target scatterings such as particles in a flow, as we will see in the next section.

1.5.3.3 Flow Measurements

The interferometric setup described in the previous section discussed the laser behavior when the laser measures relative movement of a translating solid target. In this section we will discuss how this setup is extended to be valid for flow measurements, and present a model of the laser behavior.

Several papers has been published regarding flow measurement using OFI, and the sensing scheme has been extensively used for measurements of liquid flux such as blood and flux in micro channels. De Mul et al [54], [75] used the sensing scheme to measure blood perfusion in tissue and to measure blood flow. Further work on this subject was published by Ozdemir et al for in vivo experiments [76]–[79]. J.Hast et al used the technique to measure the arterial pulse shape [80], [81]. Zakian et al contributed by measuring particle size [82]. Further advancements in the field were made by Norgia et al in measurements of blood flow and especially in vivo measurements [55], [83] Campagnolo et al, Zhao et al, Ramirez et al and Da Costa et al contributed substantially to the field in regards to measurements in micro channels, particle sizes and the use of VCSEL lasers [50]–[52], [84]–[88].

As shown in Fig. 1.20 a laser points at a flux of particles with velocity $v(t)$, at an incident angle θ to the laser beam. Here, the laser is focused at the center of the particle flux, which concentrates the beam's energy into a small probe volume (PV). The external cavity l_{ext} remains constant throughout the measurement.

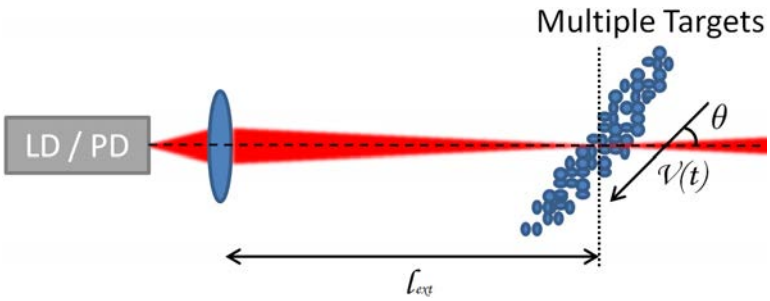

Figure 1.20: OFI Velocimeter: Schema of multiple targets, such as a flux of particles in a liquid. The flux is moving at an angle θ to the beam axis.

In this setup, each particle traversing the laser beam will contribute with a small portion of Doppler shifted light, reflected back into the laser cavity. The photo diode signal will thus be a product of the sum of all contributions from the different particles. The model is based on the equivalent cavity from section 1.5.2, and we consider that each particle has it's own reflectivity $r_{\mathrm{ext},i}$. The equivalent reflectivity $r_{\mathrm{eq}}^{'}$ for the system can be calculated by summing up all of the individual reflectivities.

$$r_{\mathrm{eq}}^{'} = r_2\Big[1 + (1 - r_2^2)\sum_i \frac{r_{\mathrm{ext},i}}{r_2}\exp(2\pi j f_{\mathrm{D},i}t + j\phi_{\mathrm{r2},i})\Big] \tag{1.54}$$

where, $r_{\mathrm{ext},i}$ and $f_{\mathrm{D},i}$ is the reflectivity and the Doppler frequency contribution of the i^{th} particle respectively. $\phi_{\mathrm{r2},i}$ is the phase difference due to the travel of the light through the external cavity from each particle and is expressed as

$$\phi_{\mathrm{r2},i} = 2\pi\nu_{\mathrm{F}}\left(1 + \frac{c - v_i\cos(\theta)}{c + v_i\cos(\theta)}\right)\frac{\tau_{\mathrm{ext},i}}{2} \tag{1.55}$$

where θ is the incident angle of the laser beam and v_i is the velocity of the i^{th} particle and $\tau_{\mathrm{ext},i}$ iis the round trip time associated with each particle. The Power Equation can thus be rewritten to reflect upon this measurement situation:

$$\boxed{P_{\mathrm{F}} = P_0\left[1 + \sum_i^N m_i\cos(\omega_{\mathrm{D}i}t + \phi_{\mathrm{D}i})\right]} \tag{1.56}$$

The angular frequency $\omega_{\mathrm{D}i} = 2\pi f_{\mathrm{D}}$ contains the Doppler frequency f_{D}, and $\phi_{\mathrm{D}i}$ is the phase accumulated by the Doppler-shifted light. We sum the contribution from each particle i, where m_i is the modulation index for each individual particle. In general the oscillating laser signal (P_{F}) is recorded and a frequency analysis on the signal is performed to determine the Doppler frequency f_{D}. Equation 1.49 is then solved for v to determine the velocity of the measured flux.

1.6 Optical Feedback Based Systems for Sound Acquisition

1.6.1 OFI Applied to the Acousto-Optic Effect

OFI has lately been applied to acoustic sensing through the acousto-optic effect. A small change in the refractive index of air induce a change in the optical path of the laser beam. Several recent papers published by Urgiles et al explore this effect using the OFI sensing scheme, [3], [59], [61] and acoustic signals and fields are recorded. Today 3D images of sound waves are reconstructed [3] from OFI measurements.

One of the first to research the acousto-optic effect using OFI was Bertling et al [1], who compared acoustic simulations to measurements acquired by an OFI sensor. In their experiment a laser beam was backscattered off a reflective surface at the same time as acoustic waves traversed the laser beam. Using displacement stages, the laser was moved from point to point in order to scan the entire sound field. The results are shown in Fig.1.21 and show an astounding similarity between the simulation and the acquired data. Later

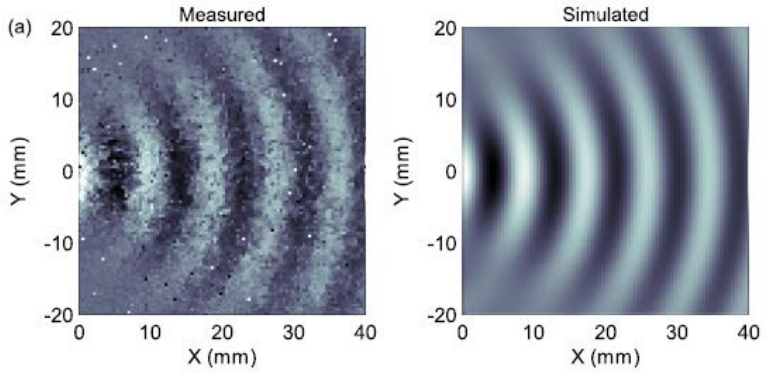

Figure 1.21: Comparison of acquisition using OFI to simulated sound field [1].

additions to the field made notably by Urgiles et al include 3D tomographic reconstructions of sound fields, measurements of near field behavior of acoustic sources and characterization of mixing of sound fields.

The laser power recorded by the interferometer can be calculated using the Power Equation

$$P_{\mathrm{F}} = P_0[1 + m\cos(\omega_{\mathrm{F}}\tau_{\mathrm{ext}})] \tag{1.57}$$

where we recognize τ_{ext} as the round-trip time between the laser and the target. τ_{ext} itself

is composed of a static and a dynamic component.

$$\tau_{\text{ext}} = \tau_0 + \delta\tau \tag{1.58}$$

where τ_0 is the nominal round-trip time and $\delta\tau$ depends on the amplitude of the refractive index of air:

$$\delta\tau = 2\int_0^L \frac{\delta n(z)}{c} dz. \tag{1.59}$$

The refractive index $n(z)$ is integrated from 0 to L which is the length of the external cavity, the factor 2 accounts for the round-trip and c is the speed of light.

Intuitively, the amplitude of the refractive index oscillates at the same rate as the acoustic wave. The oscillating refractive index will in turn make $\delta\tau$ oscillate, which impacts the expression inside the cos in eq. (1.57). Essentially, the oscillating power P_{F} images the pressure oscillation in the acoustic wave, given a linear phase to power conversion and that the optical path $<< \lambda/2$.

Philip E. Ciddor [89] published new equations for the refractive index in the visible and near infra red. The model is summarized as

$$\delta d_{\text{eq}} = L_{\text{ext}} \left(\frac{\partial n}{\partial p}\right)_{\lambda,\text{P}_0,\text{T}_0,\text{RH}_0,\text{R}_{\text{CO2},0}} \times \delta p \tag{1.60}$$

where δd_{eq} is the change in optical path, $\partial n/\partial p$ is the change in refractive index with regards to the change in pressure, and δp is the pressure difference in an acoustic wave, measured in Pa. λ is the laser wavelength, P_0 the initial atmospheric pressure, T_0 the temperature in Celsius, RH the relative humidity and $\text{R}_{\text{CO}_2,0}$ the CO_2 concentration. The conversion from acoustic pressure to distance can then be used to model and calibrate future OFI systems to increase viability an precision. In the next chapter of this thesis, the evaluation of the Ciddor model using an OFI sensor will be discussed.

It is expected that for a very small variation in the optical path ($<< \lambda/2$), the phase to power conversion gain is linearly coupled with the slope of the underlying interferometric fringe. In the next chapter, we will investigate the conversion from phase to power in order to validate this hypothesis.

1.6.2 Acoustic Particle Entrainment Measurements

Using the OFI-sensing scheme as an acoustic LIDAR has never before been attempted. However, in one application OFI is applied as an anemometer in a LIDAR configuration. The French company Epsiline (`http://www.epsiline.com`) use the OFI sensing scheme

to measure particle velocity in air [8], [90] in order to determine wind speeds. Their system use custom optics to focus the laser beam at a distance never before attained by the sensing scheme, where they measure the velocity of aerosol that traverse the laser beam. Their laser anemometer is deployed on top of wind mills where the point of measurement is in front of the turbine blades, before being affected by turbulence.

As discussed in Section 1.4.1, LDV setups has been used to measure the movement of particles in air as they were entrained by an acoustic wave. Valière et al has published extensive papers on the subject [12], [18] using classical LDV setups. His work draws knowledge and expertise from earlier publications where the subject of acoustic measurements through particle oscillations is discussed [17], [19], [21]. These applications are based on classical interferometer setups and operate at relatively short distances.

In Section 1.5.3.3 we saw how OFI is applied to the measurement of flow. The sensing scheme has been applied in a wide range of situations, ranging from blood perfusion [54], [75] to fluid and particles in micro channels [50]–[52], [84]–[87], [91]. Signal processing adapted to fluid measurements has been developed and is applied in these papers.

Using the OFI-sensing scheme as an acoustic LIDAR is now within reach with current building blocks available to us. A sensor with a similar configuration as the one used by Epsiline will enable us to detect the presence and velocity of particles at a great distance. The discussion in Section 1.4.1 shows us that acoustic measurements are possible using classical interferometers at a relatively short distance. Signal processing techniques adapted to the OFI-sensing scheme are already developed, especially in regards to fluid measurements.

When an acoustic pressure wave impinge on a particle in air, it will exert a force on it, making it oscillate. We intend to measure this oscillation using the OFI-sensing scheme in a LIDAR configuration. As in fluid measurements, the particle velocity can be measured through frequency analysis of the laser signal. The Doppler shift induced by the velocity of an acoustically entrained particle being measured by an OFI sensor will exhibit an oscillatory movement.

$$f_{\mathrm{D}}(t) = \frac{2\vec{v}(t)}{\lambda} \tag{1.61}$$

where $\vec{v}(t)$ is the particle velocity and λ is the laser wavelength. Signal processing techniques may then be applied to retrieve the acoustic wave frequency and amplitude.

The advantage of using OFI to measure acoustic waves by particle entrainment is the low cost and simple setup. The advantages of using lasers to measure acoustic entrainment has been documented in section 1.4.1. The major advantage is the non intrusiveness of this technique. Since the point of measure is dematerialized, very small zones can equally

be scanned on order to obtain data from places that are to small to position a sensor. Equally, hazardous areas may benefit from such technology as measurements are done at a distance.

In this PhD we present a demonstration of the OFI Acoustic LIDAR through simulations and experiments. In doing so we demonstrate the capacity to record and interpret acoustic signals from moving aerosol in air using OFI. First we present a first-order acoustic model to predict the movement of the particles entrained by acoustic waves. The acoustic model is compared to acquisitions of real particle velocities using an intensity probe. We show that the model is in good agreement with acquisitions. Furthermore we present a numeric model for generating synthetic interferometric signals from acoustically entrained particles. The model is compared to signals acquired thought experiments, and we show a good agreement between the two. To the best of our knowledge this has never been done before using Optical Feedback Interferometry.

1.7 Chapter Conclusion

In this chapter we have covered the basic principles of sound, and some of the major sound acquisition systems on the marked as well as a few minor ones. We have briefly discussed their advantages and disadvantages, and in what settings they are used. We have learned that the vast majority of acoustic detectors are transducer based and have to be placed in the sound field in order to record a signal.

The main challenges related to "classic" microphones and sound acquisition devices are that they are intrusive; there is a degradation of the moving parts; and they have a limited dynamic range due to inertia and the mass of the moving parts.

Interferometric techniques have been developed to measure acoustic waves and fields, using LDV and PIV techniques. These techniques offset the problems related to classical diaphragm based detectors. The major advantages of optical systems are their capacity to measure acoustic waves without perturbing the sound field; and their ability to perform remote acquisitions.

The research objectives of this PhD are 1) to explore the possibility of developing a Class 1 microphone[2] using and Optical Feedback Interferometer measuring the acousto-optic effect, and 2) to develop an experimental demonstrator for the remote acquisition of acoustic waves using and Optical Feedback Interferometer in a LIDAR configuration.

To achieve these objectives we perform research on the interferometric fringe's shape

[2]see Chapter 2, Section 2.3 for definition

and it's impact on measurements of optical path variations; we propose a model based on Philip E. Ciddor's equations for calculating the refractive index of air, which translates an acoustic pressure variation into an equivalent distance variation; we study the validity of this model and whether or not it stays within the norms of a Class 1 microphone; we also determine the lowest acoustic power detectable by our interferometric system.

In terms of remote acquisition we propose a first order acoustic model of the movement of particles entrained by acoustic waves; we propose a demodulation algorithm for recovering the acoustic information from an OFI sensor signal; we propose an experimental demonstrator to validate the acquisition method; which is extended to long distance remote acquisitions.

Chapter 2

Acoustic Sensing By Acousto-Optic Effect Using Optical Feedback Interferometry

Contents

2.1 Introduction

In this chapter we present research on the OFI microphone which is the result of an ambitious industrial goal to design and develop an acoustic acquisition device using the

OFI sensing scheme. Being an active and innovative member of the metrology and measurement community, ACOEM and it's department of innovation has taken an interest in Optical Feedback Interferometry. They are currently producing high performance and high sensitivity audio acquisition equipment for use in the industry for monitoring and maintenance purposes. Typical examples of monitoring are recognizing and detection of gas leaks in refineries through audio signatures, preventive monitoring of machines and detection and localization of hazards such as accidents or gun shots. They deliver a wide range of expertise in the acoustic and vibrometry domains, and are continuously evolving their products.

Optical Feedback Interferometry has been demonstrated as a means of measuring acoustic waves and acoustic fields. An acoustic pressure wave propagating through air will induce a small change in the refractive index which can be measured by the OFI-sensor. The small size of the sensor combined with the use of tomographic scanning techniques has yielded 3D reconstructions of sound fields. These result are of great interest to ACOEM as it becomes possible to characterize and measure sound-fields without perturbing them. Furthermore, a laser is not subjected to the same mechanical constraints as a classical microphone. Such constraints are inertia, degradation of moving parts and the continuous need of recalibration.

The overall goal for the OFI scheme applied to acousto-optic measurements was to create a replacement of existing Class 1 Sonometers. These audio acquisition devices are extremely linear, precise, and exhibits outstanding performances in a wide range of atmospheric conditions. A given measurement at any atmospheric condition in the pressure range of 65 to 108 kPa, temperature range of -10 to $+50$°C and humidity range of 10% to 90% relative humidity, should not deviate more than ~ 0.5 dB from the same measurement at a set of reference atmospheric values (outlined in Table 2.2).

2.2 The Impact of the Fringe Shape in Sub$-\lambda/2$ Sensing

2.2.1 Introduction

In 2003 Giuliani *et al* [45] devised a non-contact vibrometer where the system was designed to maintain the laser phase at an operating point through an electronic feedback loop, a method called phase locking. In Giuliani's approach the operating point is set to the half fringe, as it allows a large measurement dynamic. Measurements of down to 0.1 nm were reported. The advantage of this system was that there would be no drift in signal amplitude for a given measurement due to changes in optical conditions and there would

be no fringe jumps.

As explained by Taimre *et al* [67], for sub-$\lambda/2$ displacements, the target's movement is directly reproduced in the interferometric signal in an analog fashion. The shape of the fringe has an impact on measurements in the sub-$\lambda/2$ regime. Lukashkin et al [92], inspired by the approach in [45], regulated the mean distance between the laser and an oscillating target in order to fix an operating point around which the system would operate. This served to reduce distortions of the signal due to the fringe shape.

A deeper knowledge of these effects is beneficial for the further development of systems such as Giuliani's. One application would be for acousto-optic measurements where the reflecting surface needed for the OFI effect is known, and the laser response has been characterized. The detection capacities of these types of OFI systems could be ameliorated by locking the phase at a point where the fringe slope is steeper than on the half-fringe point. This would increase the signal gain amplitude for a given excitation.

In this section we present a dedicated experiment showing the impact of the fringe shape on small signals. We demonstrate experimentally that the signal amplitude is linearly coupled to the slope of the fringe. Furthermore we model an OFI system operating in the sub-$\lambda/2$ regime using Kliese's algorithm [68]. Finally, we show the algorithm's performance in the sub-$\lambda/2$ regime through accurately simulating the experimental results.

2.2.2 OFI model and governing equations

One of the first concise, and most frequently used models for the OFI sensing scheme was proposed by Lang et Kobayashi [70] using modified laser rate equations. The model was simplified by Petermann [66], supposing quasi static conditions. A concise algorithm based on the Three Mirror Model was developed by Kliese et al in 2014 [68]. The Three Mirror Model [58], [66]–[68] is described in Chapter 1. This model is an extension of the two mirror laser model in which a phase condition is satisfied: the optical field in the laser has the same phase after one round trip [67], [68]. In the Three Mirror Model, the laser is forced to change its emission frequency ν_{f} under feedback in order to satisfy the phase condition. The phase of the light returning into the laser is calculated using through the excess phase equation eq. (1.38) [58], [67], [68], rewritten here in terms of phase.

$$\phi_{\mathrm{F}} - \phi_0 + C\sin(\phi_{\mathrm{F}} + \arctan\alpha) = 0 \tag{2.1}$$

$\phi_{\mathrm{F}} = 2\pi\nu_{\mathrm{F}}\tau_{ext}$ is the phase response which is the external round-trip phase at the perturbed frequency. $\phi_0 = 2\pi\nu_0\tau_{\mathrm{ext}}$ is the phase stimulus which is the external round trip phase of the free running laser [67]. ν_0 is the laser's free running emission frequency, ν_{F} is the perturbed laser frequency and α is the linewidth enhancement factor [69]. The feedback parameter

C from eq.(1.37) describes the coupling strength between the laser and the external cavity [64], [67], [93], and can be written as

$$C = \frac{\tau_{\text{ext}}}{\tau_{\text{in}}} \epsilon \sqrt{\frac{R_{\text{ext}}}{R_2}} (1 - R_2) \sqrt{1 + \alpha^2}. \tag{2.2}$$

Here τ_{in} is the laser cavity round-trip time for a photon, τ_{ext} the external cavity round-trip time. R_2 is the reflectivity of the front facet of the laser, R_{ext} is the ratio of the reinjected over the emitted power and ϵ is the fraction of reflected light coupled coherently back into the laser [64], [68].

In our model we use the solver in [68] to compute the excess phase equation, eq. (2.1), and thus calculate the laser power eq. (2.9) as the laser beam strikes a moving target. To calculate the phase ϕ_{F} in eq. (2.1) the solver discriminate between two regimes of C. The first regime is for weak feedback, $C \leq 1.0$, where the right hand side of eq. (2.1) is monotonic and a unique solution of ϕ_{F} can be found. The second regime is for moderate or high feedback $C > 1.0$, and several solutions for eq. (2.1) exist. In the weak feedback regime the solution for eq. (2.1) is found using a bounded root finding algorithm. The bounds denoted ϕ_{min} and ϕ_{max} are obtained by considering $\sin(\phi_{\text{F}} + \arctan\ \alpha)$ from eq. (2.1) which is periodic between $+1$ and -1. We can thus find ϕ_{min} and ϕ_{max} by substituting $+1$ and -1 respectively for the mentioned sine function. The bounds are thus

$$\phi_{\text{min}} = \phi_0 - C \tag{2.3}$$

$$\phi_{\text{max}} = \phi_0 + C \tag{2.4}$$

Figure 2.1, taken from [68], shows the two bounds and the point where the right hand side of eq. (2.1) crossed 0.

In the case of moderate or strong feedback, $C > 1.0$, there may be several solutions to eq. (2.1). The bounds are found by taking the derivative of eq. (2.1) and setting the right hand side to equal 0. Then solving for ϕ_{F}.

$$0 = \frac{\partial}{\partial \phi_{\text{F}}} \left[\phi_{\text{F}} - \phi_0 + C \sin(\phi_{\text{F}} + \arctan \alpha) \right] \tag{2.5}$$

$$= C \cos(\phi_{\text{F}} + \arctan \alpha) + 1 \tag{2.6}$$

Now we can solve eq. (2.6) for ϕ_{F} and use it's second derivative's sign as differentiations for peak and trough locations. This yields

$$\phi_{\text{min}} = (2m + 1)\pi + \arccos(\frac{1}{C}) - \arctan(\alpha) \tag{2.7}$$

$$\phi_{\text{max}} = (2m + 3)\pi + \arccos(\frac{1}{C}) - \arctan(\alpha) \tag{2.8}$$

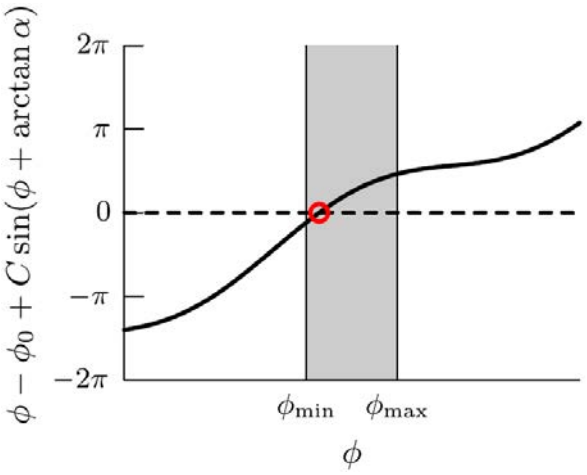

Figure 2.1: Plot of right hand side of eq. (2.1) where $C = 0.8$. The bounds $\phi_{\min}$ and $\phi_{\max}$ are marked.

where the integer $m \in \mathbf{Z}$. Take care not to confuse the integer m in this equation with the modulation index m in eq. (2.9). Figure 2.2, presented in [68], shows the $\phi_{\min}$ and $\phi_{\max}$ for the left-most solution.

The right hand side of eq. (2.1), is plotted in Fig. 2.2, where the circles show the stable possible lasing modes, and the crosses show the unstable modes. For a given integer m, the valid solutions are found between the trough and peak of the plotted line. The values of m can be determined by considering the upper and lower bounds of m, $m_{\text{lower}} < m < m_{\text{upper}}$.

The possible values of the integer m are determined by finding the leftmost and rightmost solutions of ϕ_{F} that satisfy certain conditions. To find m_{lower} we substitute eq. (2.8) into eq. (2.1) and solve for m. The bound is chosen by considering the leftmost peak position that is greater than 0, as we can see in Fig. 2.2. The upper bound, m_{upper}, is found similarly by determining the rightmost trough position that is below 0.

The algorithm also accounts for path dependence (hysteresis) which often occurs during harmonic motion measurements. The hysteresis effect makes so that the solutions to eq. (2.1) that are found when a target moves one direction, are different than the solutions found when the target comes back to is original position. This subject is detailed in [68].

In Chapter 1 in Section 1.5.2, the formula for calculating the laser's optical power under feedback is derived.

$$P_{\text{F}} = P_0[1 + m\ \cos(\phi_{\text{F}})], \tag{2.9}$$

Here,

$$m = 4\frac{r_{\text{ext}}(1 + r_2^2)}{r_2}\frac{\tau_{\text{p}}}{\tau_{\text{in}}} \tag{2.10}$$

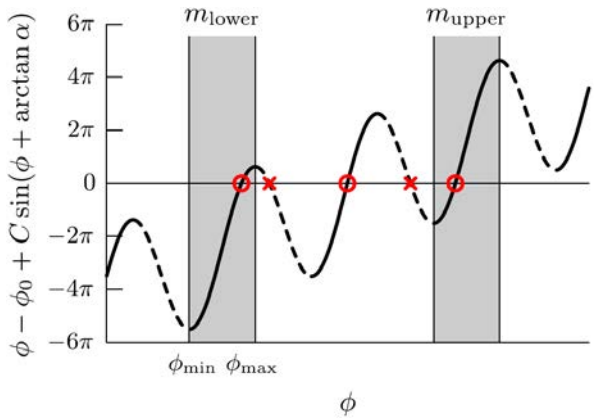

Figure 2.2: Plot of right hand side of eq. (2.1) with $C = 8$. Stable and unstable solutions are marked by solid an broken lines, respectively. The stable solutions are marked by circles. Unstable solutions are marked by crosses. The lowest and highest regions where solutions can exist are marked by m_{lower} and m_{higher}. The bounds for the lower region are marked by ϕ_{min} and ϕ_{max}.

is the well known modulation index described in Section 1.5.2 (not to be confused with the integer m from the previous paragraphs), P_{F} is the laser power under feedback and P_0 is the laser power without feedback. m depends heavily on the target reflectivity r_{ext}, and determines the amplitude of the fringes. For small displacements (a few half wavelengths) it can be considered as constant. However, for displacements with larger amplitudes, m can vary significantly because of variations of the amount of light being coupled back in the cavity. Such variations may be due to Speckle effect or defocusing amongst others [94]. In our experiments the optical conditions are set to remain unchanged and in simulations we choose to keep this term constant.

2.2.3 Experiment

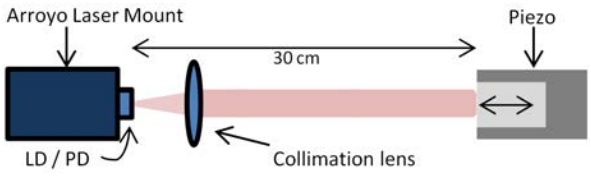

Figure 2.3: Experimental setup. Pizeo modulated at two separate frequencies.

A distributed feedback laser diode (ML720J11S) that emits a transverse and longitudinal single mode at 1310 nm is mounted on an Arroyo Instruments laser mount, including a temperature control driven by a ThorLabs TED 200C. The laser beam is focalized 0.3 me-

ters from the laser source by a ThorLabs C230TMD-C lens. The target is the metal surface of the PI P-753.2CD piezo transducer, driven by a E-665.CR LVPZT-Amplifier. The setup is schematized in Fig. 2.3. The input voltage for the piezo controller is set to 2.24 V_{pp} which generate 8 interferometric fringes. These fringes are visualized in the first plot in Fig. 2.4. The oscillation frequency is 8 Hz.

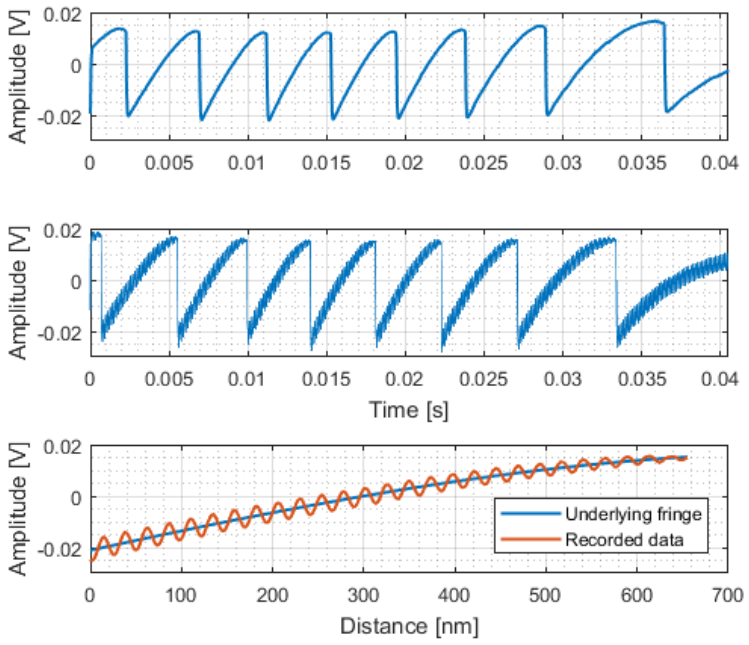

Figure 2.4: Experimentally acquired laser responses measured in Volts. **Top**: Fringes generated by moving target modulated at 8 Hz with amplitude 5.02 μm zero to peak. **Middle**: Fringes generated by moving target modulated at 8 Hz and at 7 kHz with amplitudes 5.02 μm and 110 nm respectively. **Bottom**: Zoom on fringe number 3 from the left in the middle plot. Fringe with small oscillations on top. The underlying fringe has been approximated by a 3^{rd} degree polynomial.

By modulating the piezo transducer at two separate frequencies simultaneously, we are able to observe the effects of the fringe's shape in the OFI signal at small displacement amplitudes. This is achieved by adding a small 7 kHz oscillation with an amplitude of 1 V_{pp} to the 8 Hz main oscillation. The small oscillation corresponds to a movement of approx. 110 nm peak to peak. The second plot in Fig. 2.4 shows the smaller oscillation superposed on top of the fringe. By using the piezo amplifier's manual offset, we can also move the mean position the piezo manually in order to set the desired operating point on the fringe.

2.2.4 Numerical simulations

Using Kliese's algorithm [68] we simulate the OFI system's power response at different cavity lengths, all within one fringe. The feedback parameter eq. (2.2) is empirically set to $C = 2.5$ for an external cavity length of $l_{\text{ext}} = n\lambda_{\text{laser}}/2 \approx 0.3$ m so that the simulated fringes resemble as much as possible the measured ones.

In the simulations we modify the position of the operating point by modifying l_{ext}. We simulate three scenarios where the operating point is at three different positions, and for each operating point position we simulate a small sinusoidal target displacement of amplitude 110 nm and frequency 7 kHz. Figures 2.5 and 2.6 shows the output power variation as the target moves back and forth around each operating point.

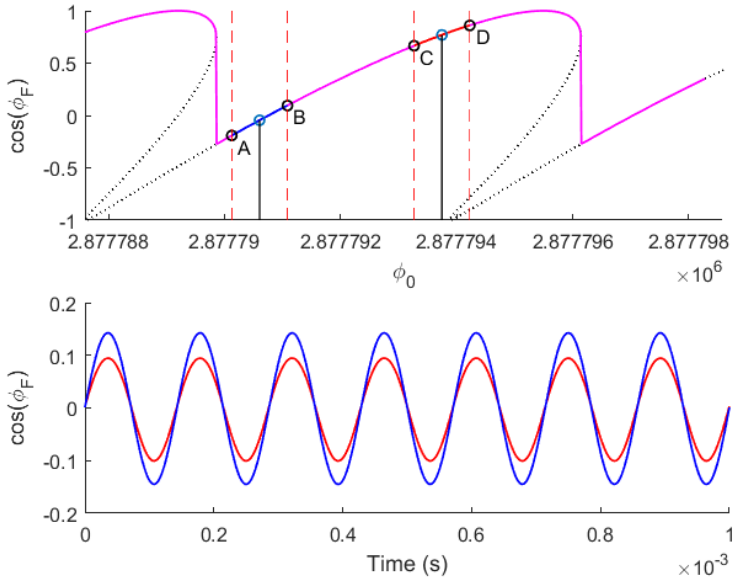

Figure 2.5: Simulation of laser power response (arb. units) as function of operating point. **Top figure**: Black dotted line: Phase development $\cos(\phi_{\text{F}})$, Purple line: corresponding fringes, Blue and red lines: part of fringe traveled. **Bottom figure**: Blue line: Power response between positions A and B, Red line: Power response between positions C and D.

2.2.5 Discussion

The simulations presented in Fig. 2.5 show that the slope of the fringe has an effect on the phase-to-power conversion gain, and thus the amplitude of the detected signal. By setting

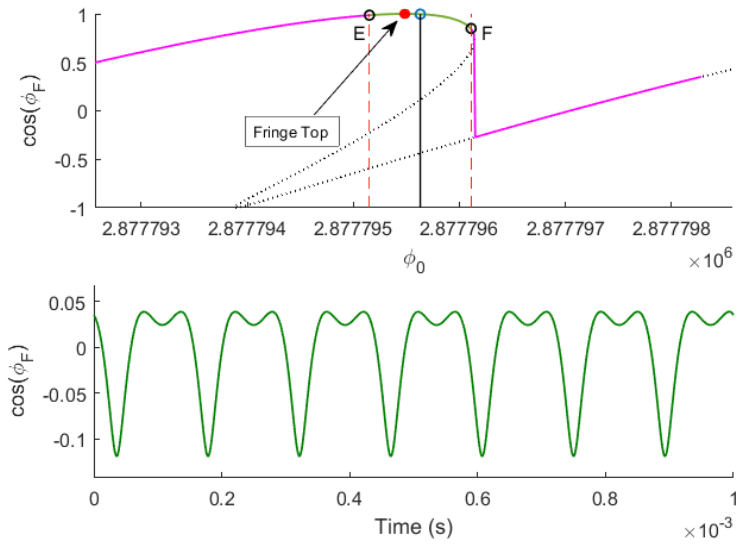

Figure 2.6: Simulation of laser power response (arb. units) as function of operating point. **Top figure**: Black dotted line: Phase development $\cos(\phi_F)$, Purple line: corresponding fringes, green line: part of fringe traveled. The top of the fringe ($\cos(\phi_F) = 1$) is marked with a red spot. **Bottom figure**: Power response between positions E and F.

the operating point between positions A and B in Fig. 2.5 the gain is higher than between positions C and D by a factor 1.47. Furthermore one can estimate the fringe slopes over the parts that produced the interferometric signals by drawing a straight line from position A to B and then from C to D. The slope between positions A and B is calculated to 0.3 whereas the slope from C to D is 0.2. In applications such as the one in [45], locking the operation point to the beginning of the fringe would thus be more beneficial when measuring very small changes in the optical path.

By further moving the operating point we can completely distort the output signals as shown in Fig. 2.6. Positions E and F have been placed on top of the fringe, right before the discontinuity. The simulation of the oscillation between these two positions confirm comments from [92], where the authors stated that placing the operating point on the top of the fringe would distort their signal.

To further validate the performance of Kliese's algorithm [68] in the sub-$\lambda/2$ domain we have compared the acquired signal to a simulation, as shown in Fig. 2.7. In the simulation we replicated the piezo's real movement while setting other experimental parameters such as l_{ext} and C equal to those in the experiment. Figure. 2.7 is a zoom on fringe number 3 from the left in Fig. 2.4. For both the simulated and acquired signal, the fringe's slow amplitude change is removed by a 1^{st} order Butterworth high-pass filter with a cutoff frequency of 6 kHz, thus leaving only the 7 kHz component.

Figure 2.7 offers a good visualization of how well Kliese's algorithm [68] works in the sub-$\lambda/2$ regime as there is clear agreement between the experimental and simulated result. We observe how the amplitude of the 7 kHz oscillation diminishes towards the top of the fringe (towards the right) in both the experiment and in the simulation, followed by a distortion of the signal before the fringe discontinuity.

In order to demonstrate that the signal amplitude of a sub-$\lambda/2$ oscillation is linearly dependent on the slope of the underlying fringe we study the last plot Fig. 2.4. We have extracted the third fringe in of the middle plot, and we have approximated the underlying fringe by a 3^{rd} order polynomial. The x-axis is converted to meters in order to reflect the target displacement of an half laser wavelength of 655 nm, which generate one fringe.

The linear relationship is found by comparing the peak-to-peak amplitude variation ΔV over the full fringe and the variation of slope of the fringe β. We have normalized both quantities with regard to their average value over the full fringe ($< \beta >$ and $< \Delta V >$). The normalized values

$$\beta_{\text{norm}} = \frac{\beta}{< \beta >} \tag{2.11}$$

and

$$V_{\text{norm}} = \frac{\Delta V}{< \Delta V >} \tag{2.12}$$

are shown in the first plot Fig. 2.8. The second plot in the figure shows the result for the simulated signal. The recorded and the simulated signals provide similar results: The signal amplitude decrease at the same rate as the slope of the underlying fringe. Thus we have demonstrated that the relationship between the amplitude of a sub-$\lambda/2$ signal and the fringe's slope is linear.

Since the linear relationship between the slope of the fringe and the signal amplitude is demonstrated, an interesting solution would be to set the operating point where this slope

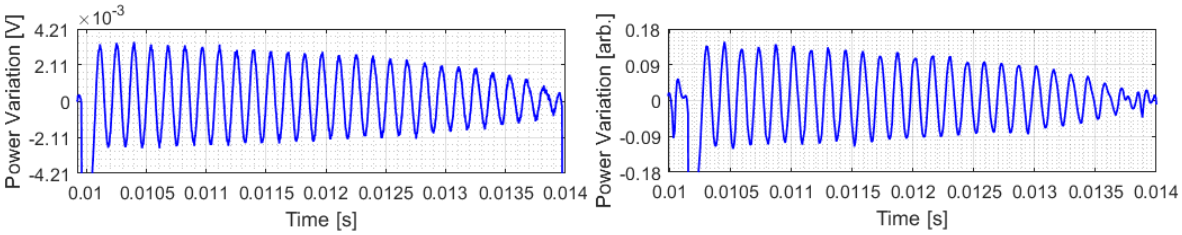

Figure 2.7: Comparison of measured interferometric signal (**left**) and simulation (**right**). The fringes have been removed using a high-pass filter, leaving only the 7 kHz oscillation in the signal. The amplitude of the 7 kHz oscillation is greater at the beginning of the fringe than at the end. The simulation result is remarkably true to the experiment.

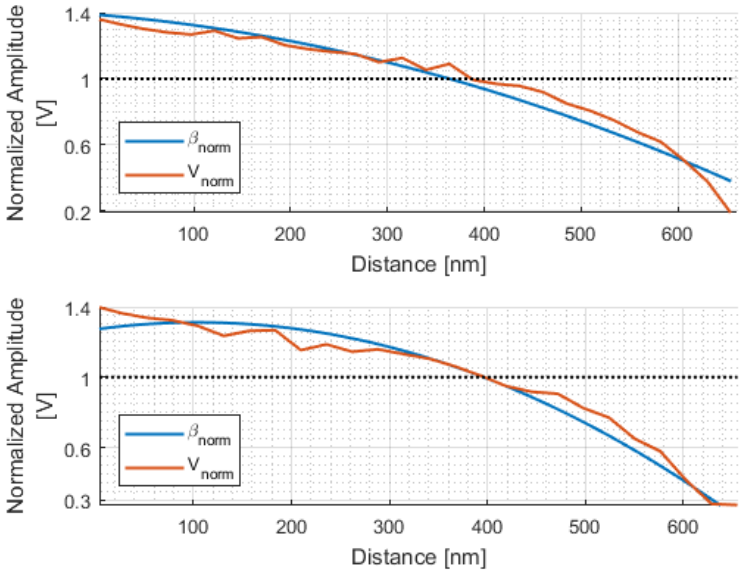

Figure 2.8: Evolution of the slope of the fringe and the evolution of the amplitude of the oscillations. **Top**: Based on signal from experiment (top plot in Fig. 2.7). **Bottom**: Based on simulated signal (bottom plot in Fig. 2.7).

is at the highest, that is to say in the fringe discontinuity. However, with large coupling coefficient C, maintaining such an operating point is difficult while controlling it with an open loop injection current command. Nevertheless, in order to demonstrate the validity of this hypothesis we have composed an experiment in which we degraded the strength of the feedback coupling by defocusing the laser beam. We estimated $C \sim 0.8$ using [68]. We then used the piezo amplifier's manual actuator to shift the mean position of the piezo, and hence the fringe operating point. The piezo was then modulated at 100 Hz at 3 mV peak to peak which corresponds to an amplitude of 8 nm peak to peak, which is the smallest stable oscillation we can produce with our system. First, the operating point was set approximately to the middle of the fringe. Then, the operating point was set in the discontinuity.

The first plot in Fig. 2.9 is an acquisition of the fringes obtained with the coupling factor $C \sim 0.8$. Estimations of the operating point positions for the following acquisitions are marked in black and red. The second plot shows the time-domain acquisition of the laser power variations while the operating point is within the black zone. The third plot shows the time-domain signal when the operating point is set within the red zone, in the discontinuity. As expected, the amplitude is higher in the last plot. The frequency - domain of the two signals were calculated and analyzed. The peak of the 100 Hz component of the signal produced mid-fringe had an amplitude of -98.82 dBV and a noise level of -107 dBV.

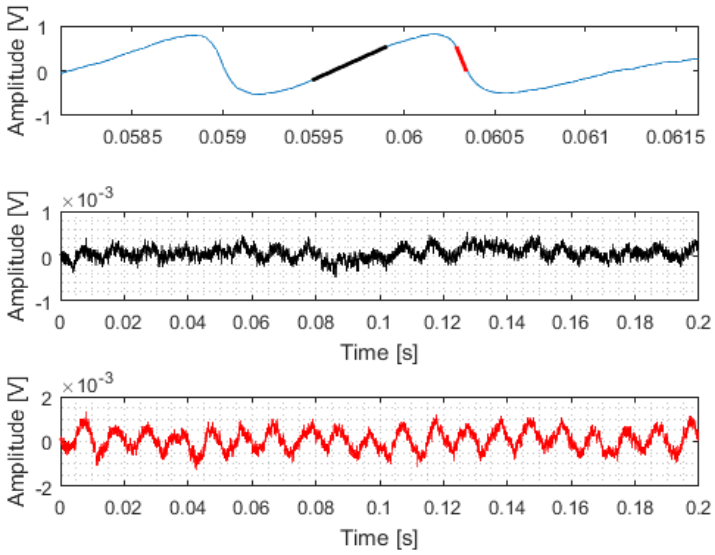

Figure 2.9: **Top**: Shape of fringes used in experiment. Comparison between operating point placed mid-fringe (**Middle**), and operating point in phase jump (**Bottom**). A barely detectable displacement signal gains amplitude by clever positioning. Piezo movement: 8 nm_{pp}. Marked in red and black in top plot: Approximate operating point zones for the two plots.

Thus the peak is only 8.18 dB above the noise floor. With the operating point positioned in the discontinuity, the amplitude of the 100 Hz was -80.93 dBV, 17.8 dB above the noise floor of -98.73 dBV.

While the C increases it implies towards a steeper and steeper intra-fringe zone. However, a steep slope will limit the dynamic range of the measurement. If a displacement is larger than the intra-fringe zone allows, the operating point will jump to a new stable mode. Further studies of the laser dynamics for higher feedback levels will clarify the limitations and benefits of such a system.

This result opens up for new investigations in the sub-$\lambda/2$ OFI sensing domain, with several exciting questions to investigate such as; The dynamic range dependency to the feedback conditions; The upper limitation of C, and; The determination of an optimal intra-fringe condition that could be achieved while modifying the feedback coupling. One could also imagine a system similar to the one employed in [45] to lock the phase onto the fringe jump, and thus exploit the higher phase-to-power gain factor. Further research shall clarify these questions and further advance the OFI sensing scheme.

2.3 Measurements of the Acousto-Optic Effect

2.3.1 Introduction

The acousto-optic effect was introduced in Chapter 1, Section 1.4.2 and several systems for measuring the phenomenon were discussed. A question who's answer is still eluding the research community is "Can we quantify the acousto-optic effect using Optical Feedback Interferometry?". Bertling et al [1] and Urgiles et al [3], [59]–[61] made several excellent demonstrations of the OFI sensor's capacities, and 2D and 3D tomographic images of acoustic fields were made. However, an exact measurement of the acoustic amplitude using OFI has not yet been presented.

In acoustic metrology the recording device must be perfectly characterized. Thus a method for quantifying the acousto-optic effect is needed. In earlier papers published on the subject of acousto-optics, limited attention was given to the amplitude of the acoustic fields. It sufficed to send acoustic waves with enough power to record an SM signal of sufficient amplitude to record the phenomenon.

In this section we will propose a model to quantify the acousto-optic effect. The model is based on Philip E. Ciddor's equations of the refractive index of air [89]. Ciddor's equations are applied to estimate the changes in refractive index in an acoustic wave, which are then converted into an equivalent optical path variation. This optical path variation will, from the lasers point of view, be seen as a simple vibration who's amplitude is proportional to the acoustic pressure under a set of given atmospheric condition.

As mentioned in Section 2.1 a goal for the OFI microphone was to create a replacement of existing Class 1 Sonometers.

These microphones have a large operating operating dynamic going from 20 dB to 140 dB. The sensitivity to atmospheric pressure in the range of 65 and 108 kPa should be such that a given measurement should not yield an error greater than ± 0.4 dB, compared the same measurement made at a set of reference atmospheric conditions (listed in table Table 2.2). The same goes for temperatures between -10 and $+50$°C where the error should be inferior to ± 0.5 dB compared to the same acquisition made at the reference atmospheric conditions. In the humidity range of 10% relative humidity to 90%, the error should not exceed ± 0.5 dB.

Furthermore, we present a study of the minimal detection limits of an acoustic wave by an OFI system measuring the acousto-optic effect. A challenge is vibrations perturbing the measurement as well as acoustic leakage perturbing our results. The lowest detectable acoustic sound pressure will be measured using an improved setup of [95] with vibration

reduction in mind. The is setup similar to those in [1], [3], [59]–[61] with special attention to the generation of planar acoustic waves, and the reduction vibrational perturbations.

2.3.2 Theory

2.3.2.1 Ciddor's Model for the Refractive Index of Air

The refractive index of air influences the time it takes for light to travel between two points in a transparent medium. Philip E. Ciddor [89] made an exhaustive model to precisely calculate the refractive index of light under given conditions. His model operates in the visible and near infrared, even for small pressure variations. The equations have their roots in several earlier published papers where attempts to create a mathematical model for calculating the refractive index of air have been proposed. Several of these papers have been cornerstones throughout several decades of the twentieth century for calculating the refractive index. With the evolution of technology, the then outdated equations were proven to be in need of modification, which motivated Ciddor to write his paper. As the first line in Ciddor's abstract goes, "The precision of modern length interferometry and geodetic surveying far exceeds the accuracy, which is ultimately limited by the inadequacy of currently used equations for the refractive index of the atmosphere.". Ciddor's equations are funded on previous work and are adopted to match reported measurements of the refractive index with minimal error. The equations should apply to a wide range of conditions, ranging from -40 °C to $+100$ °C, from 80 kPa to 120 kPa and from 0% relative humidity to 100%. They should also apply to a wide range of wavelengths, ranging from 300 nm to 1690 nm. In our experiment we mainly work with monochromatic lasers with a wavelength of 1310 nm, well within the operating range of the equations.

The parameters commonly used to derive the refractive index of air (temperature, relative humidity, air pressure and CO_2 content) where those used by Edlén [96], [97]. Measurements made by Birch and Downs [98] show that Edléns equations are erroneous by several parts in 10^7, whereas the refractive index of air should be known to at least a few parts in 10^8, as stated by Ciddor [89]. The new equations developed by Ciddor agree with Birch and Downs' corrections to their previous paper [99], to 1 part in 10^8, which is within their experimental uncertainty.

Owens [100], like Edlén determined the refractivity of each component of moist air, i.e dry air and water vapor, at known, standardized conditions. Ciddor largely used the same approach in his equations but with the addition of an equation from Peck and Reeder [101] for the refractivity of dry air. He also added an extension of Erickson's equation [102] for the relative refractivity of water vapor. Finally his paper incorporates a correction to the absolute value of pure water vapor that initially was given by Barrel and Sears [103].

Ciddor originally used MATHCAD to numerically calculate the numerous equations needed to find the refractive index. Today the Ciddor equations have been implemented in several scripting languages ranging from Fortran to Python and some are readily available online. We have implemented his equations in MATLAB® as a callable function where we input the parameters Pressure, Wavelength, Temperature, Relative Humidity and CO_2 content. The function then spits out the refractive index based on those parameters. The National Institute of Standards and Technology of the U.S Department of Commerce (`www.NIST.gov`) has implemented Ciddor's equations in an online calculator along with further documentation on the equations for interested readers. The calculator is found at `https://emtoolbox.nist.gov/Wavelength/Ciddor.asp`.

2.3.2.2 OFI Sensing Using Ciddor's Model

The refractive index n is incorporated into the OFI equations. We consider the impact of a change in n, on the round trip time of a photon traveling through air. The photon travels back and forth between the laser and an external target. In Chapter 1, Section 1.6 the OFI power equation is expressed as a function of an oscillating air refractive index, where equations 1.57 through 1.59 decompose the parameters making up the equation. A reminder is presented here.

$$P_{\mathrm{F}} = P_0[1 + m\cos(\omega_{\mathrm{F}}\tau_{\mathrm{ext}})] \tag{2.13}$$

where P_{F} is the laser power under feedback, P_0 is the initial laser power of the free-running laser, m is a modulation index and τ_{ext} is the round-trip time between the laser and the target.

$$\tau_{\mathrm{ext}} = \tau_0 + \delta\tau \tag{2.14}$$

where $\tau_0 = 2l_{\mathrm{ext}}/\frac{c}{n_0}$ is the nominal round-trip time of a photon, c is the speed of light and n_0 is the nominal refractive index of unperturbed air. In turn, $\delta\tau$ depends on the amplitude of the refractive index of air, which is a function of acoustic pressure (in Pa) as the acoustic wave travels through the external cavity:

$$\delta\tau = 2\int_0^{l_{\mathrm{ext}}} \frac{\delta n(z)}{c} dz \tag{2.15}$$

The refractive index $n(z)$ is integrated from 0 to the length of the external cavity l_{ext}. The unknown shape of the acoustic wave throughout the external cavity makes the integral necessary. The factor 2 accounts for the round-trip.

If one considers the acoustic wave to be perfectly planar, eq. (2.15) can be simplified by removing the integral, as $n(z)$ would be constant throughout z. $\delta n(z)$ can thus be

expressed as a function of time

$$\delta n(t) = \delta n_{\max} \sin(\omega_{\mathrm{a}} t) \tag{2.16}$$

where $\omega_{\mathrm{a}} = 2\pi f_{\mathrm{a}}$ with f_{a} as the acoustic frequency, and $\delta n_{\max}$ the peak modulation amplitude of the refractive index in a given acoustic wave. Equation (2.15) can thus be expressed as

$$\delta\tau(t) = \frac{2 l_{\mathrm{ext}} \delta n_{\max} \sin(\omega_{\mathrm{a}} t)}{c} \tag{2.17}$$

Putting all that back into eq. (2.13) yields

$$P_{\mathrm{F}} = P_0 \left[1 + m \cos\left(\omega_{\mathrm{F}} \left(\frac{2 n_0 l_{\mathrm{ext}}}{c} + \frac{2 l_{\mathrm{ext}} \delta n_{\max} \sin(\omega_{\mathrm{a}} t)}{c} \right) \right) \right] \tag{2.18}$$

Where n_0 and $\delta n_{\max}$ are calculated using Ciddor's equations. We thus see that the change of air refractive index, changes the laser power under feedback.

In order to quantify the acousto-optic effect, the change in refractive index (which is a function of acoustic pressure) is converted into an equivalent distance. In other words, some amount x of acoustic pressure is "seen" by the laser as some amount y of optical path change. The proposed model is simple and reads

$$\delta d_{\mathrm{eq}} = l_{\mathrm{ext}} \left(\frac{\partial n}{\partial p} \right)_{\lambda, P_0, \mathrm{T}_0, \mathrm{RH}_0, \mathrm{R}_{\mathrm{CO2},0}} \times \delta p \tag{2.19}$$

where δd_{eq} is the equivalent distance, $\partial n / \partial p$ is the change in refractive index with regards to the change in pressure, and δp is the pressure difference in an acoustic wave, measured in Pa. λ is the laser wavelength, P_0 the initial pressure, T_0 the temperature in Celsius, RH the relative humidity and $R_{\mathrm{CO_2},0}$ the CO_2 concentration.

δp and l_{ext} are known parameters, but $\partial n / \partial p$ has to be calculated. It is found using our callable MATLAB® function containing Ciddor's equations, and the result is valid only for a given set of initial atmospheric parameters.

As mentioned, the Class 1 microphone's sensitivity derivation should be very small under varying atmospheric conditions. The maximum allowed variations are shown in Table 2.2. If the variation of the refractive index exceeds any of these error margins, adaptive measures would have to be taken when using the acousto-optic effect to measure acoustic waves. Using Ciddor's model, we've simulated the refractive index over the entire range of operation for a Class 1 microphone.

The highest and lowest refractive index in this range is listed in Table 2.1. From this table we gather that next to pressure, the temperature is the biggest impactor on the

	n	Pressure	Temperature	Relative Humidity	CO_2 concentration
High:	1.0003	108 kPa	$-10°C$	10%	450 ppm
Low:	1.0002	65 kPa	$50°C$	90%	450 ppm

Table 2.1: Highest and lowest refractive index

refractive index. At low temperatures the air is denser, which increases the refractive index. For high temperatures it's the opposite, and thus the extreme values of n are found at the extreme values of T. The CO_2 concentration is held fixed at 450 ppm, as in Ciddor's paper, as this parameter has almost no impact on n.

More important for our application is the rate of change in the refractive index, the $\partial n/\partial p$. So the real question to ask, is whether $\partial n/\partial p$ remains within the Class 1 microphone's sensitivity limits when we change the atmospheric parameters. Or in other words, would a given acoustic wave have the same impact on the optical path variation at different atmospheric conditions?

To find out we will compute the rate of change in $\partial n/\partial p$ for all the possible values of temperature, pressure and relative humidity, within the specified ranges for a Class 1 microphone. For each parameter (P, T, RH) the evolution of $\partial n/\partial p$ is computed while the other parameters remain constant. Thus the dependency of the $\partial n/\partial p$ to one parameter must be computed for all possible values of the two others.

Figure 2.10 shows the evolution of $\partial n/\partial p$ as RH for T= 292 K and $p = 89$ kPa, as well as its average value and max amplitude. Equation 2.20 shows how we calculate the relative rate of change in $\partial n/\partial p$, as compared to its average value against relative humidity RH

$$Q(RH) = \frac{\Delta \frac{\partial n}{\partial p}(RH)|_{\mathrm{p,T}}}{< \frac{\partial n}{\partial p}(RH)|_{\mathrm{p,T}} >} \tag{2.20}$$

For this particular temperature and pressure, the relative rate of change Q is 0.0024% when altering RH from the minimum to the maximum value.

This operation now has to be done for all combinations of pressures p and temperatures T. Once all $Q(RH)$ are calculated, we repeat the entire process but this time we find $Q(T)$ for all combinations of relative humidity RH and p as shown in eq. (2.21).

$$Q(T) = \frac{\Delta \frac{\partial n}{\partial p}(T)|_{\mathrm{p,RH}}}{< \frac{\partial n}{\partial p}(T)|_{\mathrm{p,RH}} >} \tag{2.21}$$

Then finally we repeat the process to find $Q(p)$ for all combinations of T and RH as shown

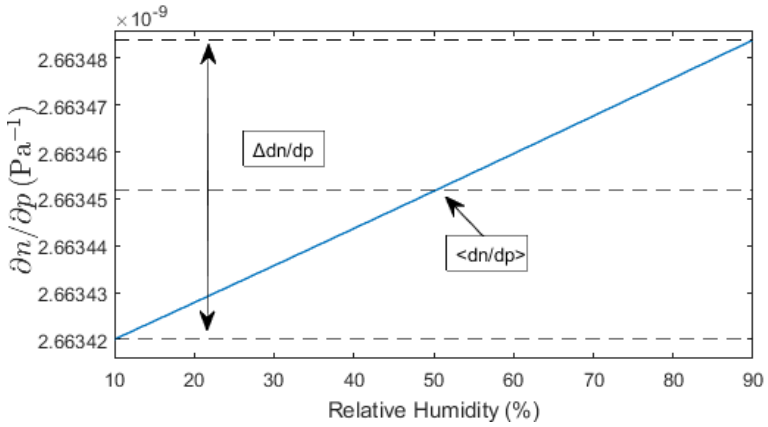

Figure 2.10: Change in $\frac{\partial n}{\partial p}$ at varying relative humidity RH at temperature $T \sim 19°\text{C}$ and pressure $p \sim 89$ kPa.

in eq. (2.22).

$$Q(p) = \frac{\Delta \frac{\partial n}{\partial p}(p)|_{\text{T,RH}}}{< \frac{\partial n}{\partial p}(p)|_{\text{T,RH}} >} \tag{2.22}$$

Figure 2.11 shows the evolution of $\partial n/\partial p$ at each temperature and pressure in the validity range of a Class 1 microphone. An arrow marks the example calculated in Fig. 2.10 and eq. (2.20). The strongest variation of $\partial n/\partial p$ is found at $T = 50°\text{C}$ and $p = 65$ kPa and is equal to 0.012%.

Figure 2.12 shows the variation of $\partial n/\partial p$ at all possible combinations of T and RH within the range of a Class 1 microphone. As we vary the pressure we observe that the maximum change amounts to 0.06%.

Figure 2.13 shows the variation of $\partial n/\partial p$ when we vary the temperature. As we've deducted from Table 2.1, the temperature has a high impact on the refractive index. Figure 2.13 tells us that regardless of the pressure and relative humidity, $\partial n/\partial p$ will change an average of 20.7% when moving from the lowest to the highest temperature. In turn, this translates into a $\sim$ 20.7% difference in equivalent displacement in eq. (2.19) at any given atmospheric condition over the range of allowed temperatures.

Table 2.2 displays the tolerances for a class 1 microphone according to the IEC61672[1] norms. The microphone definitions state that the measured sound level displayed by the instrument at any atmospheric pressure shall not exceed ± 0.4 dB from the value measured at the reference atmospheric conditions (displayed in the fourth column in the table). The same goes for temperature and relative humidity that should not deviate by more than ± 0.5 dB between a given measurement and the same measurement at the reference

[1] `https://webstore.iec.ch/publication/5708`

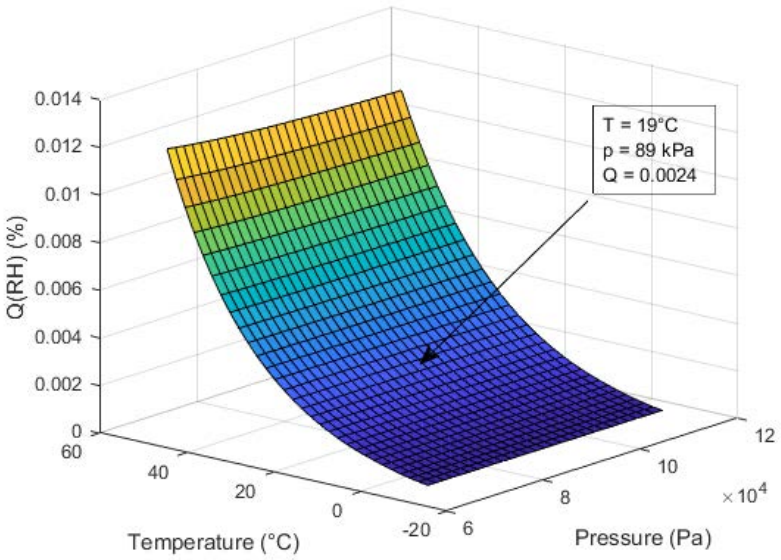

Figure 2.11: Change in $\frac{\partial n}{\partial p}$ expressed in % over the entire range of RH, for all combination of T and p.

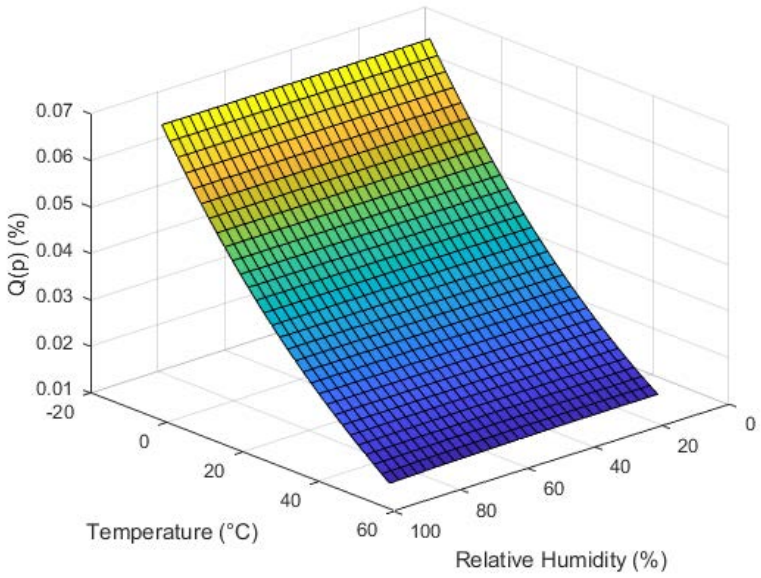

Figure 2.12: Change in $\frac{\partial n}{\partial p}$ expressed in % over the entire range of p, for all combination of T and RH.

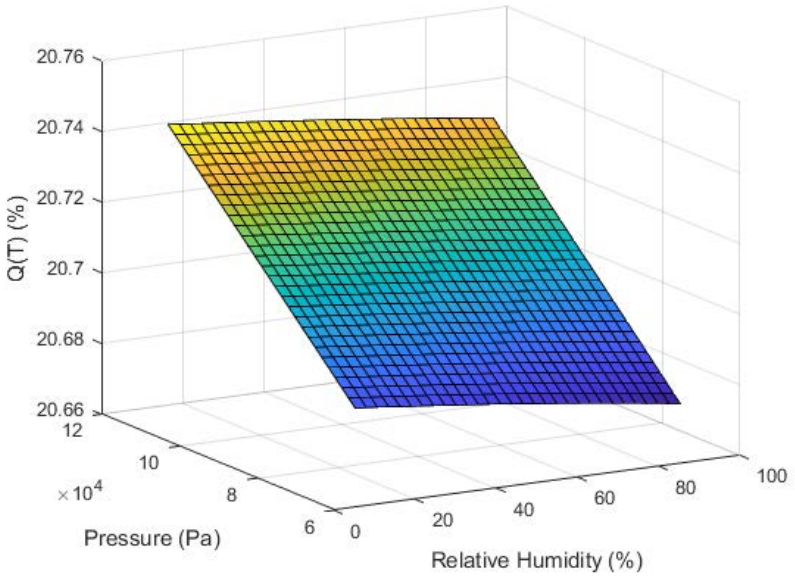

Figure 2.13: Change in $\frac{\partial n}{\partial p}$ expressed in % over the entire range of T, for all combinations of p and RH.

	Class 1 microphone definitions	Max error model prediction	Operating range	Atmospheric reference values
P	±0.4 dB	±0.005 dB	65 - 108 kPa	101.325 kPa
T	±0.5 dB	±1.64 dB	−10 - +50°C	23°C
RH	±0.5 dB	±0.001 dB	10 - 90 %RH	50%

Table 2.2: Comparison of maximum allowed variation in T, P and RH over the entire operating range of a Class 1 microphone, compared to model prediction of highest allowed acoustic wave.

atmospheric conditions.

To determine whether we meet the specifications of a class 1 microphone or not, we consider only the highest acoustic pressure within it's operating range: 140 dB = 200 Pa. At this sound pressure, the impact of the errors calculated in equations (2.11)-(2.13) on the measured signal will be maximized. The measured acoustic pressure p_{err} containing an error due to the atmospheric conditions is calculated as

$$p_{\text{err}} = p_{\text{re}} + Q \times p_{\text{re}} \tag{2.23}$$

where P_{re} is the real acoustic value. The error Err in dB is calculated as

$$\begin{aligned} \text{Er} &= p_{\text{err}}(\text{dB}) - p_{\text{re}}(\text{dB}) && (2.24) \\ &= 20 \log_{10}(1 + Q) && (2.25) \end{aligned}$$

Table 2.2 displays the deviation in dB for the highest acoustic pressure of 140 dB. We observe that the errors for relative humidity and atmospheric pressure are very small. On the other hand, when changing the temperature the error is amplified beyond the allowed limits.

Since the error is linearly coupled with the acoustic pressure, it diminishes as we measure lower pressures. However, a future device measuring the acousto-optic effect to record acoustic waves can compensate the error by integrating a thermometer that measure the temperature in the vicinity of the detector. Thermometers can be made very small and are easy to integrate into almost any device. The detector's response to an acoustic wave can thus be corrected using the thermometer.

2.3.3 Experiment: Acousto-Optic Effect Quantification and Lower Detection Amplitude of Acoustic Waves

A Distributed Feedback laser diode (1310P5DFB) emitting a transverse and longitudinal single mode at 1310 nm is mounted on an Arroyo Instruments laser mount. The mount includes a temperature control that is driven by a ThorLabs TED 200C. The laser beam is collimated by a ThorLabs C230TMD-C lens and aimed at a 1×1 cm large silicon wafer covered in silicone oxide, 200 mm away from the laser source.

The surface of the wafer is highly reflective and acts as a mirror. Due to it's light weight, the wafer can be fixed to the front facet of a PI P-753.1CD vibrating piezo, using double sided tape. A heavy weight such as a mirror would perturb the Piezo's operation. The wafer allow it to operate normally.

The piezo is driven by an E-665.C LVPZT Piezo amplifier, controlled by an HP 3325A function generator. A Thorlabs KS1D Kinematic mount is used to facilitate the alignment of the piezo to provide an efficient optical reinjection. The KS1D Kinematic mount sits on a Thorlabs 0.01mm translation stage which is fixed in place on the optical table, after alignment of the laser beam. The KS1D Kinematic mount is also fixed to the optical table using a set of metal rods after alignment.

A Hall sensor incorporated inside the piezo housing measures the position of the piezo. The piezo amplifier's monitor output provides an image of the position through an analog signal. The output is connected to a Tektronix DPO 4050 oscilloscope where the piezo position is read in terms of voltage. A conversion factor of $1.5 \cdot 10^{-6}$, as provided by the equipment data sheet, is multiplied with the output signal to obtain the position in meters.

The acoustic waves are injected into a cylinder of diameter 55 mm and length 750 mm. The waveguide's diameter $\varnothing_{\mathrm{w}} < \lambda_{\mathrm{acoustic}}/2$ is smaller than a half acoustic wavelength $\lambda_{\mathrm{acoustic}}$, rendering the acosutic waves planar as they travel through the guide. This is essential to assure a homogeneous pressure, and thus refractive index, throughout the laser beam.

The acoustic wave is generated by a Visatron FRS 8 speaker that is mounted inside an acoustic impedance adapter of length 130 mm at the end of the waveguide. The acoustic impedance adapter and waveguide fixed together using thermal glue, and placed on two pedestals fixed in place on the optical table. The waveguide is isolated from the pedestals using vibration absorbing foam. The Laser and it's temperature controlled mount is fixed on the optical table. This configuration greatly reduces parasitic vibrations, as the speaker and the waveguide are isolated from the optical components.

The dimensions of the waveguide renders it suited for the low frequency range in the acoustic domain. The upper acoustic frequency limit is 3 kHz. With higher frequencies we cannot guarantee a homogeneous planar acoustic wave.

The speaker is driven directly by an Agilent 33210A function generator. A G.R.A.S 46AE metrologic microphone is inserted into the waveguide over the laser beam, flush with the inner wall as to not perturb the pressure wave. The acoustic signal is acquired by an ACOEM 04dB acquisition card connected to the microphone.

Two 352C18 accelerometers are positioned on the piezo casing and laser housing in order to record the relative displacement between the two as the acoustic waves passes by. The signals are acquired using an ACOEM 04dB acquisition card. Once acquired, the accelerometer signals are integrated two times before being added to one another to compute the relative displacement between the mirror and the laser.

To determine the minimal detection level of the system, continuous sinusoidal acous-

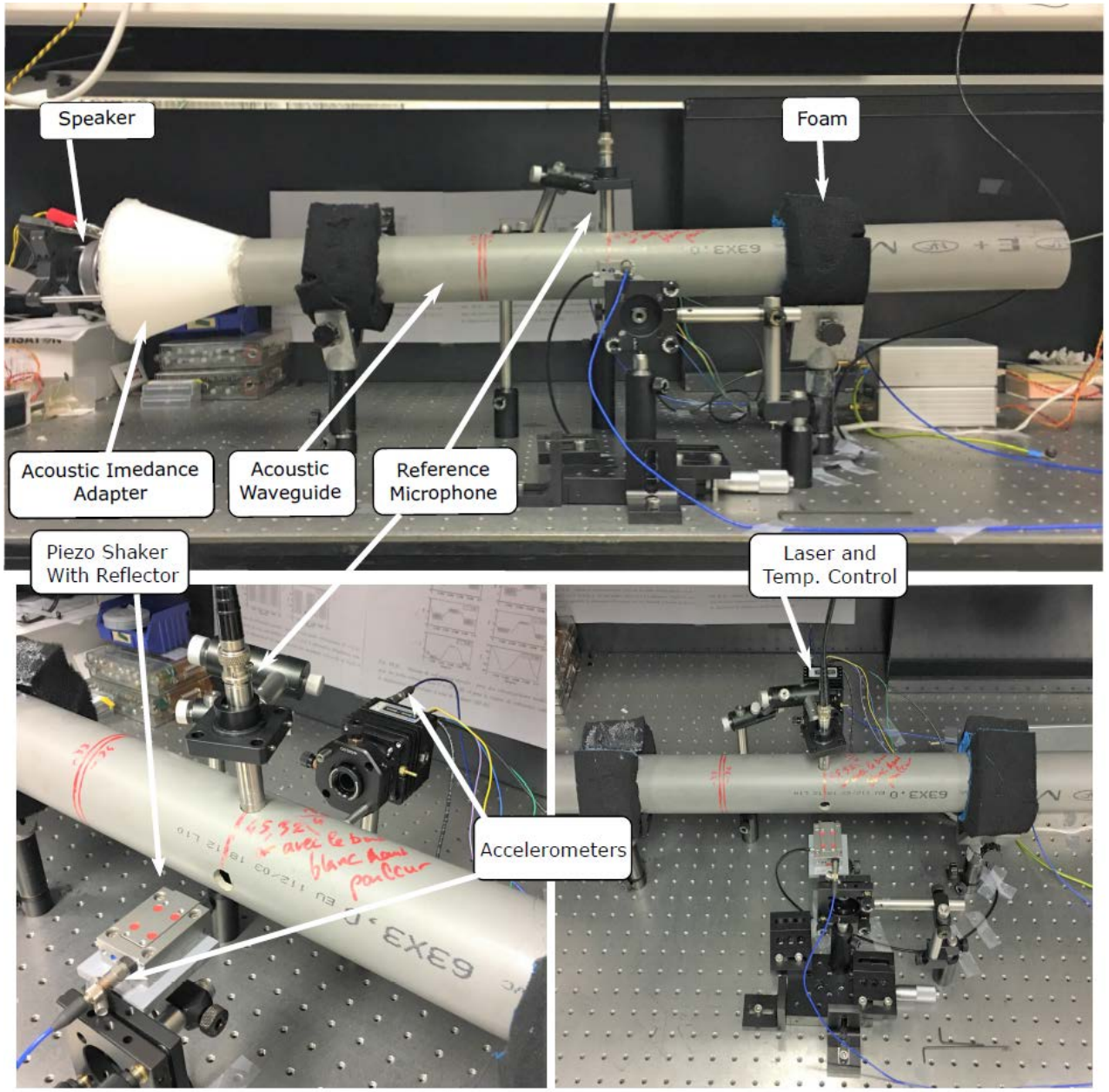

Figure 2.14: Photos of experimental setup.

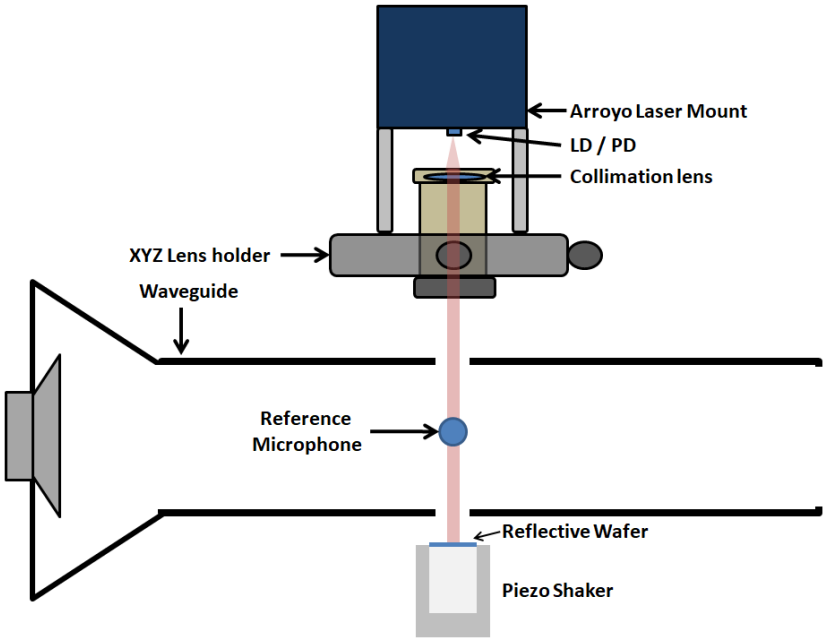

Figure 2.15: Schema of experimental setup.

tic signals at different frequencies are sent through the waveguide and the OFI signal is recorded for different signal amplitudes.

Two reference measurement enables us to correlate the acoustic pressure to a measurable mechanical displacement. The acoustic waves are recorded using the reference microphone, and the exact movement of the piezo is measured by the Hall sensor. The correlation is done in two steps. First an acoustic wave is sent through the laser beam, and the SM-signal amplitude is recorded. Then the acoustic signal is cut, and the piezo is actuated. It's vibration amplitude is set so that the SM-signal amplitude equals that of the acoustic recording. The vibration amplitude is recorded by the Hall sensor.

Since the SM-signal amplitude is equal in both steps, the optical path variation due to the change in refractive index must be equal to the piezo's vibration amplitude. The acoustic pressure can thus be converted to an equivalent distance δd_{eq} using the model. The equivalent distance calculated by the model is then compared to the Hall sensor's measurement of the piezo's displacement.

Figure 2.15 displays a schema of the experiment.

2.3.4 Method

The two experiments presented in this section share the same experimental setup. For clarity we start by outlining the steps for each experiment separately. The results are presented in Section 2.3.5, however some experimental input parameters are provided in this section.

2.3.4.1 Quantification of the Optical Path Variation using Ciddor's equations

As previously established, the OFI sensor responds to changes in the optical path. These changes can be generated by several means. In order to quantify the the acousto-optic effect, we will utilize the experiment outlined in the previous section to stimulate the sensor using acoustics and vibrations. We will compare the laser response from an acoustic stimuli to the response from a vibration measurement. The method is outlined in this section and the results are discussed in Section 2.3.5.

To quantify the acousto-optic effect a two step procedure is followed. First an acoustic wave is sent through the waveguide and laser beam. The acoustic amplitude is measured by the reference microphone which is inserted into the waveguide, directly over the laser beam. The acoustic signal from the reference microphone and the SM-signal are simultaneously recorded by the oscilloscope.

The accelerometers placed on the piezo's outer casing and on the laser mount's casing record the relative displacement between the laser and the wafer, induced by the acoustic waves.

In the second step, the pizeo is actuated at the acoustic frequency, and it's vibration amplitude is set so that the SM-signal amplitude is equal to the one measured in the previous step. The two acquisitions have to be done in the shortest possible time, one after the other. This minimizes the risk of changes in the optical conditions between experiments.

An image of the piezo's displacement is provided by the piezo's internal Hall-sensor. The SM-signal is acquired simultaneously as the piezo's displacement signal. The acquisition parameters used to record the various signals are displayed in Table 2.3.

Since the OFI-sensor measures changes in the optical path, when the laser response to the vibration measurement is equal that of the acoustic pressure measurement, we consider that the optical path variation is the same between the two measurements.

The acoustic pressure acquired by the reference microphone is then used to calculate the theoretical equivalent displacement using the model outlined in Section 2.3.2.2. The

Acquisition Parameters		
	Acoustic	**Piezo**
Sampling frequency f_s (kHz)	50	50
Number of samples	10^4	10^4
Excitation frequency f_a / f_vib(kHz)	2	2
Acoustic pressure / Vibration amplitude	4.115 $\mathrm{Pa}_{0-\mathrm{peak}}$	0.46 $\mathrm{nm}_{0-\mathrm{peak}}$

Table 2.3: Acquisition parameters for experiment to quantify the acousto-optic effect

estimation of the equivalent displacement is then compared with the displacement measurement made by the Hall-sensor.

Equation (2.26) is used to calculate the equivalent displacement δd_eq. The input parameters are listed in Table 2.5

$$\delta d_\mathrm{eq} = l_\mathrm{ext}\left(\frac{\partial n}{\partial p}\right)_{\lambda,P_0,\mathrm{T}_0,\mathrm{RH}_0,\mathrm{R}_{\mathrm{CO2},0}} \times \delta p \tag{2.26}$$

2.3.4.2 Lower Detection Limit of Acoustic Waves

The lower detection limit is measured for several frequencies and the experimental setup remains unchanged from before. The process is straight forward; the acoustic generation is set to it's minimal output level and acoustic waves at a chosen frequency is produced. The acoustic signal is recorded by the reference microphone and by the OFI-sensor simultaneously.

After each acquisition the acoustic power is incremented. The accelerometers record the relative displacement between the laser and the reflector for each acquisition.

The acoustic amplitude at the excitation frequency is found in post processing by calculating the Fourier Transformation on the reference microphone's signal. The SM-signal response at the acoustic frequency is found using Welch's algorithm in order to reduce noise, and thus better detect the acoustic signal acquired by the laser.

The algorithm essentially divides the signal into smaller sections and calculates an FFT on each section. The output power density estimation is the average between each of the calculated spectra. An overlap of 50% between consecutive each section is chosen. This method is efficient in order to reduce spectral noise, since the noise is averaged out between each consecutive FFT.

Acoustic frequency f_a	500 Hz	1.2 kHz	2 kHz	2.7 kHz
Sample frequency f_s	5 khz	10 kHz	10 kHz	10 kHz

Table 2.4: Input parameters for experiment. Number of samples: 10^4.

To determine the lower level of detection for the OFI-sensor, we then plot the SM-signal's power density estimate at the acoustic frequency against the acoustic amplitudes recorded by the reference microphone.

The experiment was repeated at four different acoustic frequencies. Table **??** shows the general acquisition parameters and the acoustic frequencies used for the four experiments.

2.3.5 Results and Discussion

The results from the two experiments outlined in the previous method are presented in this section. First we present the results from the quantification of the optical path variation using Ciddor's equations. Then the results from this experiment are discussed.

Quantification of the Optical Path Variation using Ciddor's equations

As explained in Section 2.3.4.1 an acoustic signal and a vibrometry signal generating equal SM-signal amplitude responses are acquired. Figure 2.16 compares the SM-signals from the vibrometry acquisition and the acoustic acquisition. The 10 first periods of the acquired SM-signals are displayed. The acoustic acquisition is displayed in red and the vibrometry acquisition in blue.

The average amplitude of the acoustic acquisition and the vibration acquisition is 85.7 mV and 82.2 mV zero to peak perspectively. There is a small amplitude difference $\Delta V = 3.5$ mV zero to peak between the two, but it is not possible to tune more accurately the piezo amplitude.

According to the piezo datasheet, the conversion coefficient from measured volts to displacement is 0.0056 nm/mv, then we use it to calculate the equivalent displacement induced by the pressure change as displacement.

$$d_{\text{eq}}(85.7 \text{ mV}) = \boxed{0.48 \text{ nm}} \tag{2.27}$$

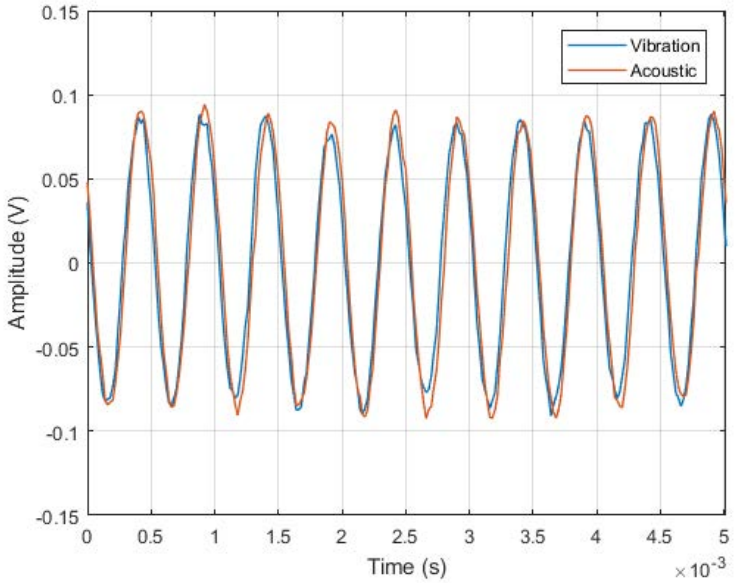

Figure 2.16: Laser response to 0.46 nm zero to peak vibration (blue) and 4.115 Pa zero to peak planar acoustic wave (red). Frequency: 2 kHz for both signals.

Parameter		**Value**
Laser wavelength	$\lambda =$	1310 nm
Atmospheric pressure	$P_0 =$	101325 Pa
Acoustic pressure	$\delta p =$	4.115 Pa
Temperature	$T =$	23° C
CO_2 concentration	$R_{\mathrm{CO2}} =$	450 ppm
External cavity length	$l_{\mathrm{ext}} =$	0.55 m

Table 2.5: Input parameters for equivalent distance estimation

Now that we've established what piezo displacement is necessary to produce an SM-signal with the same amplitude as for the acoustic measurement, we can compare it with the theoretical model.

To do this we use Eq. (2.28) to calculate the theoretical displacement. The input parameters used are listed in Table. 2.5.

$$\delta d_{\mathrm{eq}} = l_{\mathrm{ext}} \left(\frac{\partial n}{\partial p} \right)_{\lambda, P_0, \mathrm{T}_0, \mathrm{RH}_0, \mathrm{R}_{\mathrm{CO2},0}} \times \delta p \tag{2.28}$$

The external cavity length equals the diameter of the waveguide and δp is set equal to the recorded acoustic pressure. Table 2.6 displays the experimental result and the result from

the model.

Model:	4.115 Pa ⇒ 0.59 nm
Measurement:	4.115 Pa ⇒ 0.48 nm
Relative displacement:	30 pm

Table 2.6: Comparison between model and measurement

The accelerometers are used to calculate relative movement between the laser and the wafer during acoustic acquisition. The accelerometer signals are filtered around the acoustic frequency using a 20^{th}-order bandpass filter in order to remove a DC-offset in the acquired signal. The cutoff frequencies are $f_{\text{low}} = 1.5$ kHz and $f_{\text{high}} = 4$ kHz.

The signals are integrated twice to recover the displacement in meters. The two signals are then added to one another to calculate the relative displacement. The average relative displacement between the piezo and the laser during acoustic acquisitions is shown in Table 2.6: $d_{\text{relative}} = 3.01 \cdot 10^{-11}$ m which is 30.1 pm and thus neglectable with regard to the estimated optical path change.

As shown in Table 2.6, the experimental results deviate some from the prediction of the model. The amplitude of a 4.1 Pa zero to peak acoustic wave is estimated to generate a 0.59 nm optical path variation using the model. However, the experimental measurement shows an equivalent optical path variation of 0.48 nm. The model predicts an equivalent displacement that is 1.22 times greater than the measurement.

We have investigated the reason that could induce this difference:

- Using the accelerometers we calculate a small relative displacement during acoustic acquisitions between the accelerometers. At 30.1 pm, this acoustically induced variation should not have a notable impact on the measurement.

- The reflective wafer is fixed to the front of the piezo shaker using double sided tape. A small vibration induced in the wafer, however, may go undetected by the accelerometer as it is positioned on the back of the piezo casing. Nevertheless, during acoustic acquisitions the piezo's Hall-sensor did not register a movement of the piezo.

- When the piezo is set in motion, it is assumed that the wafer follows the motion of the piezo. If the wafer does not perfectly follow the piezo's motion, this could be a source of error. The current state of the experiment makes it complicated to verify this hypothesis. We would have to measure the actual movement of the wafer using a non contact measurement tool. If we put an accelerometer on the wafer we change its response.

- The relative standard deviation RSD was calculated on the displacement signal from the piezo actuator's Hall-sensor, and it amounts to RSD = 8.5%. This could indicate a

small lack of precision in the Hall-sensor's output. The vibration measurement made by the laser resulted in an RSD = 3.65%. Since we recorded 200 periods, the lack off precision should be diminished as we average over all the periods, however. The smallest RSD was measured for the acoustic measurement, at RSD = 2.32%.

- The dimensions of the acoustic impedance adapter and the waveguide should generate planar acoustic waves at the chosen frequency of 2 kHz. However, the microphone measurement is a point measurement, whereas the laser integrates the entire optical path to measure the acoustic wave. In the case where the acoustic waves are inhomogeneous, the defects in the wave would go undetected by the microphone. This puts a question mark on the accuracy of the reference measurement.

- The holes drilled in the waveguide for passing the laser beam are smaller than 2 cm in diameter and should not affect the acoustic wave. Currently we have no reliable way of estimating potential edge effects in and around these holes. Thus there may be variations in the refractive index in these zones that go uncounted for.

Lower Detection Limit of Acoustic Waves

The results from the experiments to determine the lower detection limits of our system are presented in Fig. 2.17. Each subfigure in Fig. 2.17 represents a single frequency measurement at incrementing acoustic powers. The acoustic frequencies are displayed in Table **??**.

The responses to the acoustic amplitudes are approximated using 7^{th} order polynomials and the approximations are superposed on top of the raw data. The high order was chosen because the lower order polynomials provided poor fits and would greatly diverge for the lower acoustic powers. The polynomials helps guide the asymptotic lines, marked in red in Fig. 2.17. The intersection of the asymptotic lines is estimated as the lower detectable acoustic power at the given frequency.

Table 2.7 displays the key results from the experiments. It shows for each frequency the minimum acoustic level detected; the power of the minimum detected frequency in the SM-signal; the estimated noise floor of the sensor at the acoustic frequency; and the equivalent distance the acoustic pressure should yield using the model discussed in the previous section.

The noise floors for the respective measurements are as the horizontal asymptotic line. The amplitude of these lines are displayed in Table 2.7.

In order to reach the low sound pressure levels, we had to remove the acoustic amplifier. Thus, the most powerful acoustic wave generated was thus only 79.95 dB_{rms}. For this reason there was little relative motion measured between the laser and the wafer using the

Frequency	Minimum acoustic detection	SM signal power at acoustic frequency	Noise Floor	Model: equivalent distance
500 Hz	67 dB_{rms}	−76.16 dBV	−77.84 dBV	8.38 pm
1.2 kHz	35 dB_{rms}	−79.50 dBV	−80 dBV	0.21 pm
2.0 kHz	48 dB_{rms}	−84.25 dBV	−85.45 dBV	0.94 pm
2.7 kHz	39.5 dB_{rms}	−84.50 dBV	−86.6 dBV	0.35 pm

Table 2.7: Experiment results acoustic detection

accelerometers.

The signals from the two accelerometers are then added to one another to calculate the relative displacement. A part from one single acquisition, the relative motion of the system was so small to be detected by the accelerometers indicating no significant relative displacement. The exception is found at 1.2 kHz at the strongest acoustic amplitude of 66.55 dB_{rms}, where the accelerometers measured a relative motion of 9.1 pm. All other measurements show no detectable movement.

Both Fig. 2.17 and the key elements presented in Table 2.7 indicates that the minimal detectable acoustic power is frequency dependent. We consider it unlikely that the OFI-sensor's detection capacities depends on the frequency. As stated by Taimre et al [67] and shown is Section 2.2, a sub-$\lambda/2$ optical path variation is reproduced in the SM-signal in an analog fashion. The frequency of the optical path variation should not have an impact on the signal amplitude, as opposed to the amplitude of the excitation. Thus, we discuss on the potential reasons that led to this results :

- The laser's temperature is held constant using the thermistor in the laser mount. The laser power supply is set to deliver a fixed current. However, any change in either injection current or laser temperature will change the point of operation on the fringe and thus the SM-signal amplitude. However, considering we consider the stability of the system to be sufficient to only exhibit minor variations in repeatability.

-As mentioned before, the wafer is attached to the piezo using double sided tape, covering the entire back side of the wafer. If the acoustic waves were to vibrate the reflective wafer, it may go undetected by the accelerometers. This leaves us with uncertainty regarding the displacement data. If the perturbations are great enough, this may have an impact on the detected signal.

However, at very low acoustic amplitudes, a parasitic vibration in the wafer should be minor. As discussed in the previous section, the reference microphone measures de acoustic power in one single point while the laser beam integrates the change in refractive index throughout the entire length of the external cavity, including the contribution of the wave

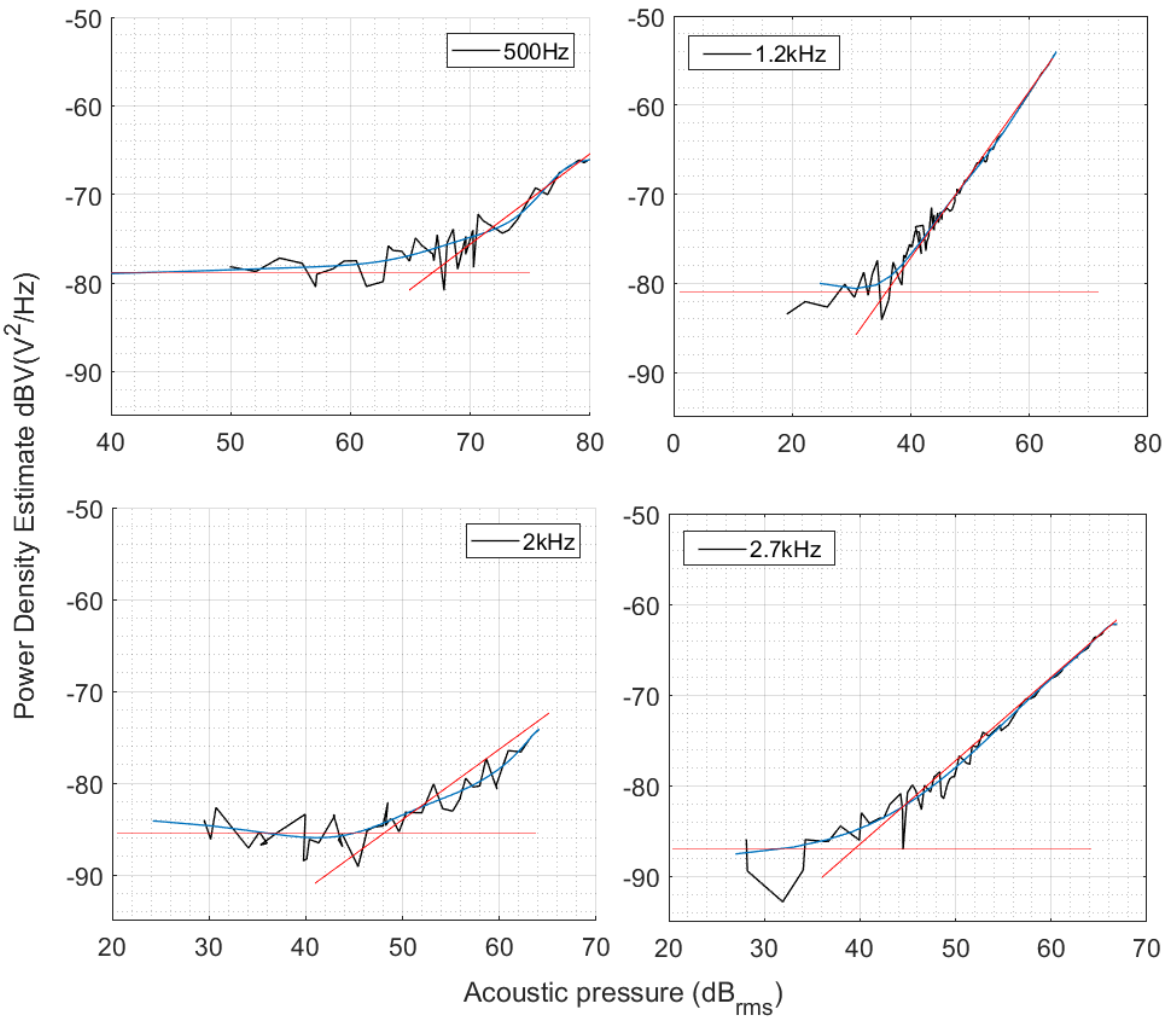

Figure 2.17: OFI-sensor response to acoustic levels at acoustic frequencies 500 Hz, 1.2 kHz, 2 kHz and 2.7 kHz. The black jagged lines is the acquire data, the blue solid line is a 7^{th}-order polynomial approximation and crossing of the red asymptotic lines determine the lowest detectable acoustic power.

outside the waveguide. If the wave is not homogeneous, this would impact the detected result.

-We believe that the frequency dependency most likely comes form acoustic effects inside the waveguide. We may have an inhomogeneous acoustic field throughout the laser beam, which is different in the line of measure by the laser, from the point of measure by the reference microphone. As mentioned before, we also have to consider that there might be edge effects in the holes drilled in the guide for passing the laser beam.

The four acquisitions demonstrated in this section shows however, that low acoustic pressures are detectable. Amongst the acquisitions the lowest detectable acoustic amplitude was 35 dB_{rms}. This is a 48 dB_{rms}-improvement on the earlier published results of 83 dB_{rms} [95] using a similar experimental setup.

Table 2.7 shows the estimated equivalent displacement using the model based on Ciddor's equations. The results from these experiments, however, puts a question mark on these estimations. In the previous section we saw that the estimated equivalent distance was calculated to be 1.23 times greater that the measured displacement. The validity of this result must be evaluated with the findings from this experiment in mind.

The experimental setup is currently pushed to its limit of operation. A future version of this experiment is thus to apply necessary ameliorations to the experimental setup which shall lead to the validation of the model based on Ciddor's equations. These ameliorations should also remove the frequency dependence of the detection amplitude.

Finally, an increase of optical path would further improve the minimal detection amplitude. The longer integration of the change in refractive index would have a greater impact on the detectors lower sensitivity limit. However, this must be done knowing that the acoustic field is homogeneous throughout the laser beam.

2.4 Chapter Conclusion

In this chapter we've discussed OFI-sensing in the sub-$\lambda/2$ domain, where optical path variations are smaller than the half laser wavelength. Typical sensing domains are vibrometry and acoustics through the acousto-optic effect, where the optical path variations are smaller than a half laser wavelength.

Through experiments and simulations we have demonstrated the impact of the slope of the interferometric fringe on sub-$\lambda/2$ optical path variations. Using the model published by Kliese et al [68], we show that the phase to amplitude conversion gain for such small variations depends on the slope of the fringe. We show that the a steep slope has a positive

impact on the conversion gain, and thus the signal amplitude, as opposed to a flat slope.

The model is supported by experiments and we show that there is linearity between the slope of the fringe and the resulting signal amplitude for a given measurement. This indicates that by closely controlling the operating point on the fringe, we can position it where the signal response is the highest. Typically, the fringe slope is higher at the beginning, meaning this would be an optimal position to set the operating point to maximize detection.

As the slope of the fringe impacts the conversion gain, we have performed an experiment where we positioned the operating point in the fringe jump, between two fringes. The slope is much steeper in between the fringes than on the fringes themselves.

The simulation and the experiments were performed in the weak and moderate feedback regimes. Further research would need to be performed in order to validate this for the strong feedback regime.

A future perspective generated from this experiment is that OFI vibrometers measuring sub-$\lambda/2$ optical path variations may benefit from an increased sensitivity, by placing the operating point in between two fringes. Thus one may drastically increase the sensor's sensitivity. Future research must include a study of the system stability at different feedback parameters C.

A model for calculating the optical path variation in a sound wave, based on Ciddor's equation for the refractive index of air has been proposed. The model takes atmospheric parameters and the acoustic pressure as input. An experiment has been put in place to demonstrate the efficiency of this model and to measure the lowest detectable acoustic pressure amplitude by our OFI system.

For a 2 kHz acoustic wave of 4.115 Pa zero to peak amplitude, the model based on Ciddor's equations estimate an optical path variation of 0.59 nm zero to peak. This value is 1.23 times higher than the measured optical path variation of 0.48 nm, using the piezo's internal Hall sensor.

Using the same experimental setup, we've shown that the smallest detectable acoustic amplitude is different between the four acoustic frequencies tested. The lowest detectable acoustic amplitude that was obtained at 1.2 kHz is 35 dB_{rms}. This value remains 15 dB above them minimum requirement of with a class 1 microphone, which is 20 dB.

Considering the limits of the laser microphone presented in this chapter with regards to the class1 microphone that was the research objective. It has been decided that the performance will not be met in the time frame of this PhD and it has been preferred to pursue towards a different sound acquisition approach that is presented in Chapter 3.

Chapter 3

Acoustic LIDAR: Particle Entrainment Measured by Optical Feedback Interferometry

Contents

3.1 Introduction

The word aerosol is an abbreviation of "aero solution" which are small solid particles or liquid droplets suspended in air. An aerosol is small enough to be completely entrained by the acoustic wave. Acting as a retro diffusing target, the aerosol (or aerosols) will reflect a sufficient amount of light for the OFI scheme to detect it's movement. Thus we propose using Optical Feedback Interferometry to demonstrate the possibility of detecting acoustic waves at a distance, based on the movement of aerosol in air.

This sensor draws inspiration from two main sensing applications where the OFI sensing scheme is used. Firstly, we use technology co-developed with the company Epsiline. Their optical anemometer measures wind speed using the OFI sensing scheme. In their application they focus a laser beam into a fixed point in space. When particles traverse this point, a signal burst containing a Doppler frequency is detected by the laser. The signal is acquired and processed to extract the particle velocity from the Doppler frequency.

Secondly we draw inspiration from the fluidic and micro-fluidic domain. In this sensing domain fluid velocities and densities are measured using the OFI sensor. Signal processing techniques such as the weighted moment method is used in order to obtain the velocity information from the flow [51]–[53].

In this chapter we present a demonstrator of the Acoustic LIDAR by Optical Feedback Interferometry. In principle we measure the oscillating velocity of a particle entrained by an acoustic wave. We will build a LIDAR application similar to that of Epsiline, even using their optics to demonstrate possibility of long distance operation. The signal processing algorithms are based on the weighted moments method which initially has been developed for applications in fluid measurements.

First, we present an established model for estimating the acoustic pressure from the velocity of the oscillating particulate medium through which the sound wave is moving. The model is then used to convert a measured velocity oscillation into an acoustic pressure. Although the model is well established in the acoustic domain, it is validated experimentally using an intensity probe, a device measuring the particle velocity in an acoustic wave. Further on we propose a modification to the OFI Power Equation, (1.50) and (1.56), adapting them to model a flow of particles with oscillating velocity.

The acoustic model and modified OFI Power Equation is finally combined to create a simulation of an OFI system's behavior when measuring the velocity of a flow of aerosol being modulated by acoustic waves. The simulation is enriched to reflect upon the Gaussian shape of the laser beam, and the random behavior of particles in air.

A signal processing algorithm is developed to acquire the acoustic signal that set the

particle flow in motion. The algorithm will first be used to demodulate the synthetic acoustic signal issued by our simulation. Then it will be applied to real signals acquired in a dedicated experiment.

We present two main experiments with different configurations. Firstly we will measure the frequency response of the acquisition scheme using a short operating range. The frequency response of the particle flow and laser system is measured and compared to the model. Then we will present a long range experiment, where use the optical setup from Epsiline's OFI anemometer. In this setup a laser beam is focused at 11.5 m from the laser.

3.2 Acoustic Model

3.2.1 Theory

Sound can be considered as a material wave. A sound wave thus needs a surrounding molecular matter to propagate. In a material at rest the acoustic wave propagates by slightly displacing the particles in the propagating medium, who will in turn set into motion adjacent particles before returning back into their resting position. This chain reaction of particles transferring their energy from one to another makes the wave propagate, and is called a longitudinal wave. In air and in water this is the major form of acoustic propagation.

J. K. Taylor [104] stated that if a particle is small enough, it will follow the flow of the surrounding molecular matter. As acoustic frequency or particle size increases, the ability to follow the surrounding matter's movement decreases. Taylor evoked the frictional force given by the Stokes-Cunning-Ham law, modifying the particle's ability to be entrained. Temkin and Leung [105] proposed equations for the velocity of a rigid sphere in a sound wave. They looked at different fluid configurations such as inviscid fluids (having no or negligible viscosity), incompressible fluids, and viscous incompressible fluids. Clerker et al [23] and Zhou et al [106] propose models incorporating forces such as the Stoke drag force, unsteady viscous drag and the effect of a pressure gradient on a particle.

Acoustic fields in closed spaces are notoriously difficult to model as there are reflections coming off the surrounding surfaces. Acoustic reflections coming from a wall, nearby table or floor will modify the acoustic field in the point of measure. Modeling a complex acoustic field is outside the scope of this work.

Thus we propose a model that is normally valid for a progressive, far-field sound wave, for calculating the velocity of a particle being entrained by an acoustic wave. In the model we will consider an unperturbed, one dimensional plane acoustic wave traveling in a single

direction. Since we operate with very small aerosol ($\varnothing \approx 3$ μm as is explained in the experiment Section 3.6), we assume that the particles follow the surrounding molecular matter. Taylor [104] estimates that a 3 μm particle with a relative density $\rho_{\text{rel}} = 2.5$ to that of air will be perfectly entrained by an acoustic wave up to 5 kHz.

Since the model is a first order approximation for the particle behavior, we have omitted the Stoke drag force and the unsteady viscous described in [23] and [106]. We also consider planar acoustic waves. The acoustic pressure for a far field, planar acoustic wave [107] can can be expressed as

$$p = \rho c_{\text{air}} v \tag{3.1}$$

Where p is the acoustic pressure, ρ is the density of air and v is the particle velocity which is equal to the velocity of the surrounding molecular matter (the *particular* velocity). This expression is derived in the the acoustic literature [107], and a basic overview is offered here. The Helmholtz equation for an acoustic wave can be expressed as

$$\nabla^2 \underline{\mathrm{p}} = \frac{1}{c_{\text{air}}^2} \frac{\partial^2 \underline{\mathrm{p}}}{\partial t^2} \tag{3.2}$$

Where $\underline{\mathrm{p}}$ is the acoustic pressure in the time domain, c_{air} is the speed of sound in air and t is time. In the frequency domain the acoustic pressure can be expressed as

$$p(M,t) = \Re\Big(p(M,\omega)e^{j\omega t}\Big) \tag{3.3}$$

where M is a spatial point and ω is the angular frequency. The wave equation can thus be expressed as

$$\nabla^2 \underline{\mathrm{p}} + \frac{\omega^2}{c_{\text{air}}^2} \underline{\mathrm{p}} = 0 \tag{3.4}$$

Let consider a small volume, far enough from the acoustic source so that the radius of the curvature of the wave front can be considered as much larger than the size of the volume. Under this condition, the solution of the wave equation can be expressed in the form of a plane wave

$$p(M,\omega) = A_p e^{-jkx} \tag{3.5}$$

where A_p is the amplitude of the acoustic pressure in the volume, k is the wavenumber in the direction of propagation, $k = \frac{\omega}{c_{\text{air}}}$ and x the coordinate along the direction of

propagation.

The Euler equation, given in its general vector form can be expressed as

$$\rho \frac{d\vec{\underline{v}}}{dt} = -\vec{\nabla}\underline{p} \tag{3.6}$$

where ρ is the density of air and $\vec{\underline{v}}$ is the particular velocity in the time domain. Using eq. 3.6, the particular velocity v can be expressed in the frequency domain, in the direction of the wavefront as

$$j\omega\rho v = -\frac{\partial p}{\partial x} = jkp = j\frac{\omega}{c_{\text{air}}}p \tag{3.7}$$

Which gives rise to the well known impedance relationship between p and v

$$p = \rho c_{\text{air}} v \tag{3.8}$$

By solving for v, we convert an acoustic pressure into a velocity

$$v = \frac{p}{\rho c_{\text{acoustic}}} \tag{3.9}$$

Using this simplified model we can convert a particle velocity oscillation into pressure (and vice versa), which essentially indicates the amplitude of the sound wave that sat the particle into motion in the first place.

3.2.2 Validation of Acoustic Model

To validate the model we use an intensity probe utilizing a microphone duplet. The probe is a G.R.A.S Type 50 AI Intensity Probe with G.R.A.S 12AB power module and a 1/4" type 26AA Microphone Duplet. The ensemble is connected to a Data Translation DT9837 24-bit acquisition card with a fixed sampling frequency $Fs = 52.7$ kHz. The microphone duplet is first placed at around 25 cm from a Visaton W 200 speaker driven by a dynavox VT-80 stereo amplifier. The data is acquired using the dBFA acquisition software from ACOEM. Matlab is used for processing and plotting. The velocity data is extracted from dBFA using the method described in Annex A.

The loudspeaker sends continuous sound waves in the direction of the microphone duplet, and we consider the waves to be plane. Two acquisition sessions are performed. In the first session, a series of continuous sound waves at $f_{\text{a}} = 700$ Hz are recorded by the

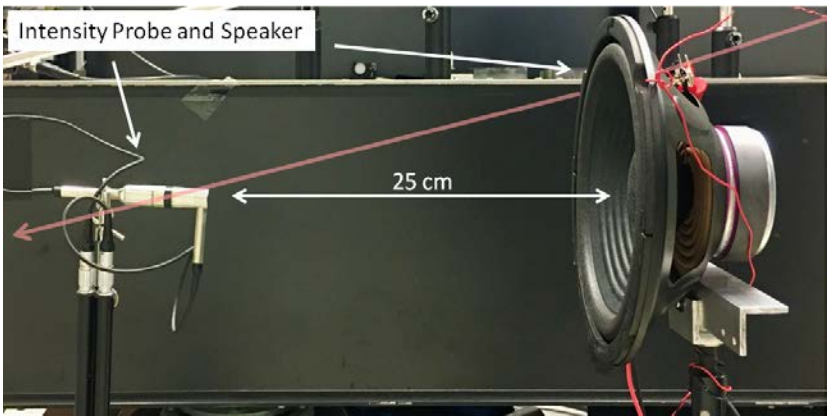

Figure 3.1: Photo of experiment to validate theoretical model. The red arrow indicates the laser beam that is used in later experiments.

microphone duplet at increasing acoustic powers ranging from 6.2 $\mathrm{Pa_{RMS}}$ to 11.9 $\mathrm{Pa_{RMS}}$. In the second session continuous sound waves at different frequencies ranging from 50 Hz to 3 kHz are recorded.

Figure 3.2 shows a comparison between the recorded data from the first session and the model. The recorded data shows linearity between the acoustic pressure and the particle velocity, just as the model. The model shows a slightly lower velocity output per acoustic pressure than the measurement. This offset amounts to an average of 0.0035 $\mathrm{m/s_{RMS}}$ below the measured value. This difference is explained by the complexity of the acoustic field in the vicinity of the detector, which biases the recording. As sound waves bounce of nearby walls, the floor and other obstacles, the acoustic field will change it's attributes in the point of measure. This is seen in the results from the second recoding session, demonstrated in Fig. 3.3

Figure 3.3 compares the measurement made by the intensity probe at different frequencies to the model. The line shows the probe measurement and the green line shows the model. The two lines are in good agreement except for the lower frequencies of 50 to 200 Hz.

The speaker's near-field is a region in which the acoustic field has a complex behavior and the particle velocity and acoustic pressure are not in phase. Also, the acoustic energy bounces back and forth within the vibrating surface of the source, without escaping or propagating [3]. The near-field can be estimated as

$$z = \frac{D^2 - \lambda_\mathrm{a}}{4\lambda_\mathrm{a}} \tag{3.10}$$

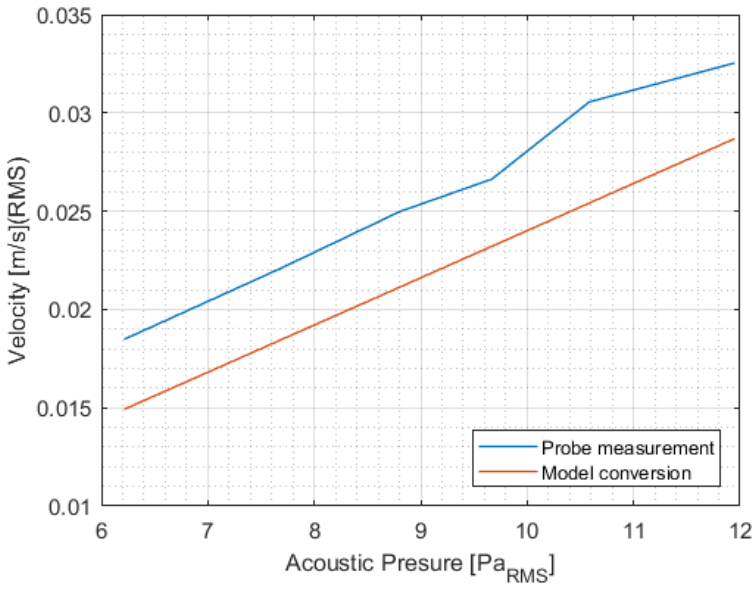

Figure 3.2: Particle velocity measurement at $f_a = 700$ Hz

where $D = 18.5$ cm is the inner diameter of the speaker and λ_a is the acoustic wavelength. At 50 Hz the acoustic wavelength $\lambda_a = 6.68$ m and the near-field is estimated to be $z = 10.7$ cm. Our acoustic model is linearly dependent on the pressure, and the acoustic frequency does not affect the estimated amplitude. The measurement however, shows that there are other things going on that are not accounted for in the model.

The near-field estimation is generic and does very likely deviate from the specific near field of the Visaton W 200 speaker used in our experiment. The high velocity response for the lower frequencies can possibly be attributed to near-field effects.

Although imperfect we can conclude that the model does a good job at approximating the the real acoustic velocity, for an unperturbed acoustic wave. The differences between the acquired data and the model can be attributed to the complex acoustic field that is established around the point of acquisition. The only way of precisely qualify the model's performances would be to put the experiment in an anechoic chamber.

Through the two experiments presented in this section, we show that the model sufficiently approximates the real unperturbed acoustic field. The model is deemed sufficiently accurate as a first approximation of the particle velocity. Later on we will use the model to generate synthetic OFI signals based on the movement of particles entrained by acoustic waves.

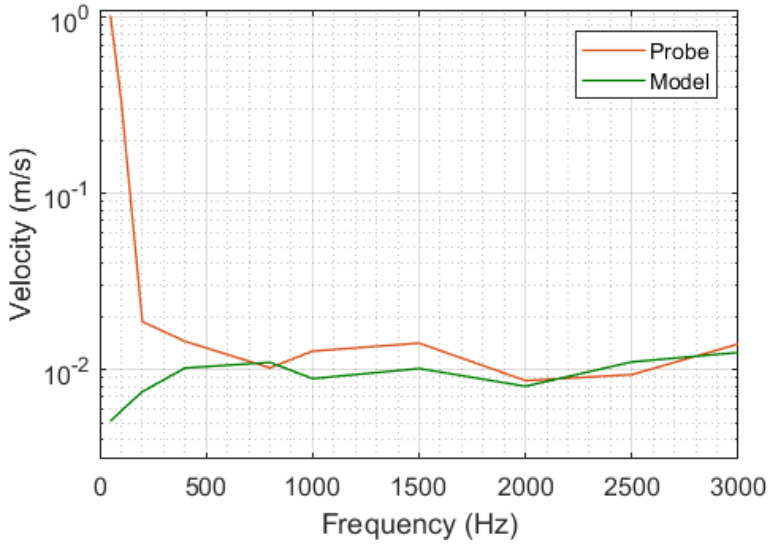

Figure 3.3: Particle velocity measurement at frequencies ranging from 50 Hz to 3 kHz, represented by the acoustic powers.

3.3 Integration of Acoustic modulation in the OFI Power Formula

The theory and model surrounding a laser subjected to optical feedback has been outlined in Chapter 1, Section 1.5 with a precise description of feedback from multiple particles in Section 1.5.3.3. An equation for the laser power was derived, eq. (1.56) which reads

$$\boxed{P_{\mathrm{F}} = P_0\left[1 + \sum_{i}^{N} m_i \cos(\omega_{\mathrm{D}i}t + \phi_{\mathrm{D}i})\right]}$$

Where P_{F} is the laser power, P_0 is the initial laser power without feedback, $\omega_{\mathrm{D}i}t = 2\pi f_{\mathrm{D}i}t$ is the Doppler frequency $\phi_{\mathrm{D}i}$ is the phase shift due to the Doppler shift of the light and N is the number of particles.

In this section we will provide an expansion of the OFI model to account for periodic modulations of the Doppler frequency f_{D} due to periodic velocity modulations of a particle flow. In modifying the Power Equation, we show how eq. (1.56) is not adapted to model velocity modulated particle flows in it's current state.

To demonstrate, let's consider a flow of particles where the particle velocity is modulated periodically by an acoustic pressure wave with frequency f_{a}. The particle velocity can be

expressed as

$$v = v_0 + \Delta v_{\max} \cos(2\pi f_{\mathrm{a}} t) \tag{3.11}$$

where $\Delta v_{\max}$ is the amplitude of the velocity change and t is time. Classically This expression would be inserted into the Doppler formula to find the Doppler frequency:

$$f_{\mathrm{D}}(t) = \frac{2[v_0 + \Delta v_{\max} \cos(2\pi f_{\mathrm{a}} t)] \cos(\theta)}{\lambda} = f_{\mathrm{D},0} + \Delta f_{\mathrm{D,max}} \sin(2\pi f_{\mathrm{a}} t) \tag{3.12}$$

where $\Delta f_{\mathrm{D,max}} \sin(2\pi f_{\mathrm{a}} t)$ is the changing component of the Doppler frequency with $\Delta f_{\mathrm{D,max}}$ as the amplitude of the frequency variation. To express the variation of Doppler frequency in the OFI Power Formula, consider the phase change induced by the Doppler shift as expressed as

$$\phi_{\mathrm{F}}(t) = 2\pi \int f_{\mathrm{D},0} + \Delta f_{\mathrm{D,max}} \cos(2\pi f_{\mathrm{a}} t) dt \tag{3.13}$$

$$\phi_{\mathrm{F}}(t) = 2\pi f_{\mathrm{D},0} t + \frac{\Delta f_{\mathrm{D,max}}}{f_{\mathrm{a}}} \sin(2\pi f_{\mathrm{a}} t) \tag{3.14}$$

The result in eq. (3.14) can now be used to make a new Self-Mixing Power formula:

$$P_{\mathrm{F}} = P_0 \left[1 + m \cos\left(2\pi f_{\mathrm{D}0} t + \frac{\Delta f_{\mathrm{D,max}}}{f_{\mathrm{a}}} \sin(2\pi f_{\mathrm{a}} t) + \phi_{\mathrm{D}} \right) \right] \tag{3.15}$$

Equation (3.15) contains the expression $2\pi f_{\mathrm{D}0} t$ as expected, and the SM-signal frequency is modulated by a sinusoidal function $\frac{\Delta f_{\mathrm{D,max}}}{f_{\mathrm{a}}} \sin(2\pi f_{\mathrm{a}} t)$. Through this formula we observe that the oscillation frequency of P_{F} changes periodically.

The amplitude of the frequency change change is determined by the coefficient $\Delta f_{\mathrm{D,max}}/f_{\mathrm{a}}$. The amplitude remains constant regardless of the acoustic frequency f_{a}. Finally we adapt eq.(3.15) to the multiple scattering regime of an aerosol flow, which gives

$$\boxed{P_{\mathrm{F}} = P_0 \left[1 + \sum_i^N m_i \cos\left(\omega_{\mathrm{D},0i}\, t + \frac{\Delta f_{\mathrm{D,max},i}}{f_{\mathrm{a}}} \sin(2\pi f_{\mathrm{a}} t) + \phi_{\mathrm{D},i} \right) \right]} \tag{3.16}$$

Where P_{F} is the laser power under feedback, P_0 is the initial laser power and m_i is a feedback coefficient depending mainly on the target reflectivity among other parameters. The angular frequency $\omega_{\mathrm{D},0i} = 2\pi f_{\mathrm{D},0i}$, and $\phi_{\mathrm{D}i}$ is the phase accumulated by the Doppler-shifted light. The oscillation $(\Delta f_{\mathrm{D,max,i}}/f_{\mathrm{a}}) \sin(2\pi f_{\mathrm{a}} t)$ is the amplitude of the Doppler frequency shift and is can simply be expressed as Δf_{D}.

A final remark is offered to the Doppler equation in terms of incident angles of sound waves on a flow of particles traveling along a given direction. Let consider that the incident

angle of between the flow and the laser is θ_1 and the incident angle an impinging acoustic wave is θ_2. When calculating the Doppler frequency, these two angles has to be accounted for separately as shown

$$f_{\mathrm{D}} = \frac{2v_0 \cos\theta_1}{\lambda_{\mathrm{laser}}} + \frac{2\Delta v \cos\theta_2}{\lambda_{\mathrm{laser}}} \tag{3.17}$$

Where v_0 is the initial particle velocity at incident angle θ_1 to the laser beam and Δv is the velocity change at incident angle θ_2 to the laser beam. The additional velocity component added to the aerosol has to be projected onto the laser axis with it's own angle, as the axis of oscillation may differ from that of v_0.

3.4 System Model: Particle Flow and Laser Response

In this section we model the response of an OFI system measuring a flow of scattering particles. The particles' velocity is modulated by an acoustic wave, and the laser power response is processed by adequate tools to recover the original acoustic signal. These tools are presented in a separate section. We start by giving an example aimed at visualizing the OFI signal generation process. Then data from the experiments is incorporated into the model, giving us a point of reference for later comparison with experiments. The experiments are presented in a separate section.

Let us first consider a 2-dimensional probe volume (PV hereafter) through which there is a horizontal flow of particles traveling along the x-axis as shown in Fig. 3.4. The PV is arbitrary set to 1 m length, and the flow has a Gaussian shape where the particle velocity is greater in the middle than at the edges. An acoustic traveling wave impinges upon the flow in it's traveling direction, thus modulating the velocity of the particles.

A 1-dimensional laser beam traverses the flow in the direction opposite to it's travel, marked by a red arrow in Fig. 3.4. For simplicity we suppose 0° incident angle between the laser and the flow. The section of the laser beam that traverse the flow responsible for gathering information of the flow's movement.

The result shown in Fig. 3.5 is the evolution of the particle velocity distribution inside the laser beam in Fig. 3.4, in time. Each horizontal line is calculated using the velocity equation, eq. (3.9), derived in section 3.2. At each time stamp t the equation produces a 1-dimensional distribution of particle velocities.

This visual representation is useful for understanding the particle velocity inside the laser beam probe volume as it evolves in time. It also offers a vision on how the data is generated and processed by the model. The datasets containing velocity information are generated in the form of the dataset in Fig. 3.5 where each horizontal line contains the

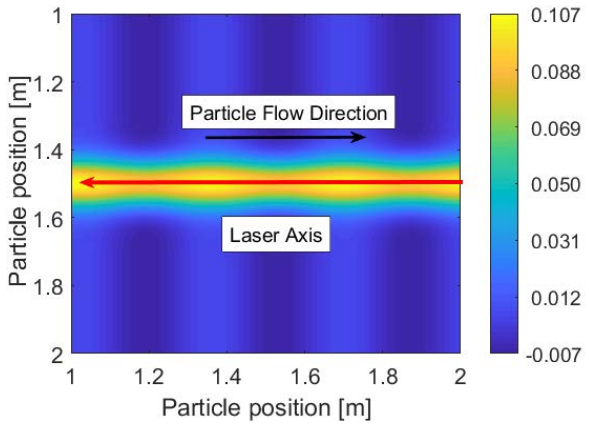

Figure 3.4: 2-D simulation sound field moving thorough particles flowing towards the right. The vertical colorbar represents velocity in m/s. The laser beam traverse the flow towards the right. The acoustic frequency is 1 kHz, the acoustic pressure oscillation $\Delta p_{\max} = 2$ Pa$_{\text{rms}}$, initial flow velocity $v_0 = 0.1$ m/s and $\Delta v_{\max} = 0.0069$ m/s.

velocity distribution of the particles at a given time t.

To further develop how the system model functions, we will discuss the simulations displayed in Figures 3.6 and 3.7. The length of the PV in these simulations is set to 2 cm, which is closer to the width of the particle flow we measure in Section 3.6. Equation (3.9) is employed to simulate the velocity of a single particle and Fig. 3.6 shows the simulation result. The entrained particle achieve an additional velocity $\Delta v_{max} = \pm 0.013$ m/s along the laser axis due to the acoustic wave.

The next step is to add more particles to the simulation. We use eq. (3.9) to calculate the velocity distribution of 1000 equally spaced scatterers throughout the PV. As the acoustic wave moves through the 2 cm PV, the pressure throughout is not equal at the beginning and at the end. Fig. 3.7 shows two extracts of the simulation. In the first plot at $t = 0.16$ ms, the velocity distribution is gradually rising from the left to right which indicates a pressure difference over the length of the PV of a traveling acoustic wave. The second plot is an extract of the particle velocity at $t = 0.4$ ms. Here the pressure descends from left to right, indicating that the wave has moved.

The the complete dataset from which the plots in Fig. 3.7 was extracted can now be used to compute the laser power P_{F} at a given time t using eq. (3.18). Here, we've included a spatial term $kz_i = 2\pi/\lambda_{\text{acoustic}} \times z_i$ that accounts for the phase difference between each individual particle as the acoustic wave propagate through the flow.

$$P_{\text{F}} = P_0 \left[1 + \sum_i^N m_i \cos\left(\omega_{\text{D},0,} t + \frac{\Delta f_{\text{D,max},i}}{f_{\text{a}}} \sin(2\pi f_{\text{a}} t - kz_i) + \phi_{\text{D},i} \right) \right] \tag{3.18}$$

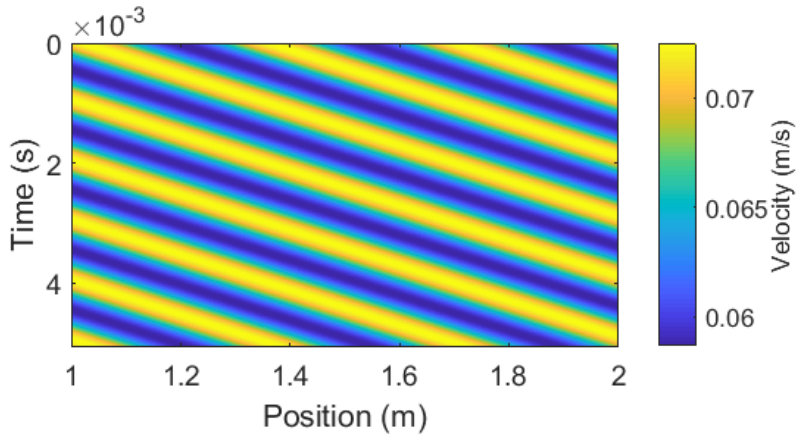

Figure 3.5: Simulation of velocity distribution of 1000 particles entrained by a traveling wave. Simulation of 1 spatial dimension (x-axis) in time (y-axis). Each horizontal line in the plot is the particle velocity distribution at a given time. The particles are evenly distanced over the 1 meter PV extension. Input parameters to eq. (3.9): $f_a = 1$ kHz, average flow velocity $v_0 = 0.1$ m/s, $z = 1$ m, $t = 0$ ms to 5 ms, $\Delta p_{max} = 2$ Pa_{RMS}, $p_0 = 101325$ Pa, $c_{air} = 340$ m/s, $R_s = 287.058$ J/kg K and $T = 293.15$ K. The velocity variation is $\Delta v_{max} = 0.0069$ m/s.

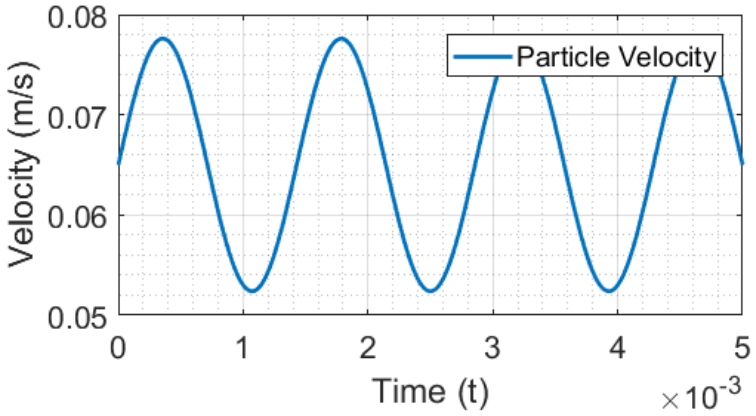

Figure 3.6: Simulation of a moving particle. The acoustic frequency $f_a = 700$ Hz, the acoustic pressure $\Delta p_{max} = 5.16$ Pa zero to peak, and the velocity component in the laser beam direction $v_0 = 0.066$ m/s. Other constants were set; Atmospheric pressure $p_0 = 101325$ Pa, velocity of sound in air $c_{air} = 340$ m/s, $R_s = 287.058$ J/kg K and $T = 293.15$ K.

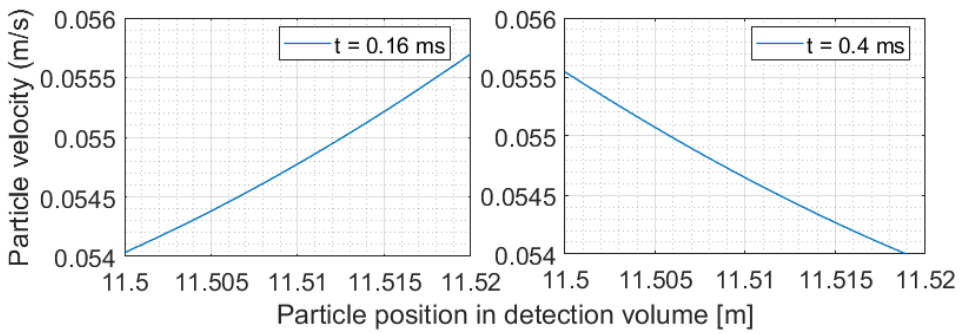

Figure 3.7: Extract of particle velocity simulation of 1000 moving particles at $t = 0.16$ ms and $t = 0.4$ ms. The acoustic frequency $f_a = 700$ Hz, the acoustic pressure $\Delta p_{max} = 5.16$ Pa zero to peak, and the velocity component in the laser beam direction $v_0 = 0.066$ m/s.

The last term in eq. (3.18) is calculated using eq. (1.55), shown below, and accounts for the phase of the Doppler shifted photons due to the movement of the target.

$$\phi_{D,i} = 2\pi\nu_F \left(1 + \frac{c - v_i \cos(\theta)}{c + v_i \cos(\theta)}\right) \frac{\tau_{ext,i}}{2}$$

Here, c is the speed of light and the round trip time of the photons $\tau_{ext\,i} = 2z_i/c$ where z_i is the position of the i^{th} particle in the PV in meters.

The simulation result shown in Fig. 3.8a, shows the frequency spectrum of the laser signal produced by the dataset in Fig. 3.7, based on the parameters discussed in the previous paragraphs. The Doppler peak is centered around 100 kHz which corresponds to a central velocity $v_0 = 0.066$ m/s around which the particles oscillate. The peak is wide accounting for the range of particle velocities presented in the signal over time. The lowest frequency peak is at 72.93 kHz and the highest is at 128.2 kHz. These values corresponds to the Doppler frequencies generated from the velocities $v_0 \pm \Delta v_{max}$.

Comparably, in the absence of acoustic modulation as shown in Fig. 3.8b the Doppler peak is precisely at 100 kHz. This is because all the particles move at the same constant velocity $v_0 = 0.066$ m/s. For simplicity, the modulation index is set constant to $m = 1/N$ for N particles in both simulations.

These results mark our ability to model the SM-signal behavior generated from an oscillating particle flow. The process of retrieving the acoustic information is explained in Section 3.5. But before getting there we will further develop the model in order to produce signals closer to what one would expect from a real system.

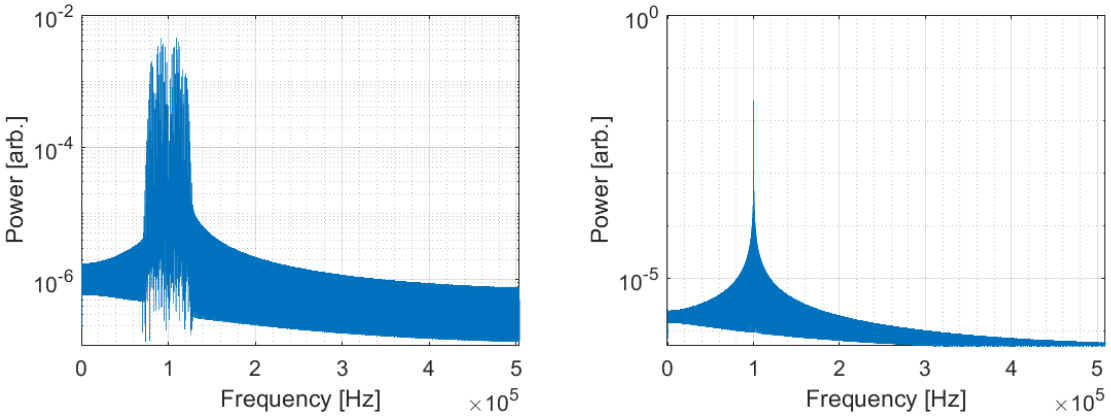

(a) Sound wave modulating aerosol velocity (b) No sound

Figure 3.8: Comparison of FFT's of output signals with presence of and absence of a 700 kHz acoustic wave with amplitude 5.16 Pa. PV = 2 cm.

3.4.1 Noise Addition

The modulation index m_i in eq. (3.18) has previously been set to $m = 1/N$ for simplicity. The index is a measure of several parameters and strongly depends on the external cavity length l_{ext} and the target reflectivity R_{ext} [1], [67].

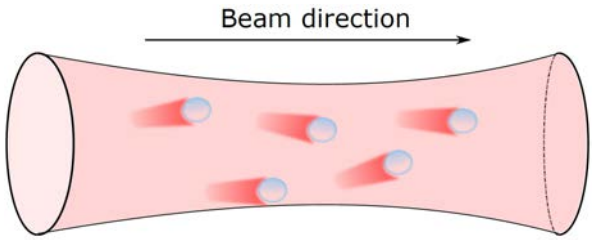

Figure 3.9: Illustration of 3-D effect achieved by ascribing an individual modulation index m_i to each reflective particle.

Figure 3.9 shows a section of the laser beam with reflective particles inside it. Each particle has a slightly different reflectivity from one another due to particle size, position and composition. Depending on the angle of intersection with the surface of the droplet, the light may be reflected, deflected or transmitted. Also, light from one particle may diffract into another, or completely block the incoming or outgoing light.

When simulating each particle with it's own randomized value of m_i, a 3-D effect is created. Each particle will add some variability to the resulting SM-signal due to the randomized value of m_i. This variation is similar to what one would expect from particle

scatterings in a 3-D volume, despite the simulation being 1-dimensional.

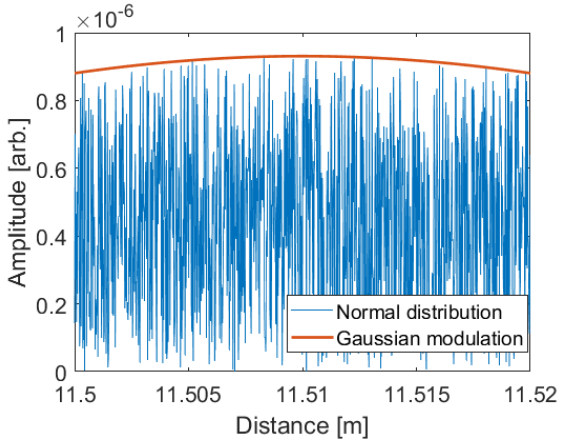

Figure 3.10: Randomly generated m_i for each particle in the PV (horisontal axis) at some time step t.

Random noise is added to m_i, for each particle in the PV, through a normal distribution. Each particle may take any value $m_{r,i} \in [m_{\min}, m_{\max}]$ where $m_{\min} = 0$ and $m_{\max} = 0.95 \cdot 10^{-6}$ (arb.units). The normal distribution is modulated by a Gaussian distribution to simulate the Gaussian shape of the laser beam, as shown in Fig. 3.10. Thus the light reflected from a particle may be of greater amplitude in the middle of the PV, where the laser beam is focused, than at the edges.

The modulation index attributed to each individual particle should change in time, as the particle moves. To incorporate this, the modulation index m_i will update it's value for each time-step t. A new randomized set of m_i values is generated for each time step in the simulation. The amplitude range of m_i is set to be relatively small to reflect that a very small amount of light is back scattered from each individual particle. A particle will not drastically change it's reflectivity from one time step to the next as is the case when a new randomized m_i is ascribed for each time step. To account for this, the changing values of m_i is smoothed numerically out to make the change more gradual. Thus each particle will have it's own modulation index m_i that changes slowly, but randomly in time, as shown in Fig. 3.11a. The figure shows the value of m_i in time for the 11 first particles in the PV. There are 1000 time steps in the section, giving a good overview of the gradual change of m_i for each particle in time.

Implementing these values in our simulation, renders the SM signal noisy, which eventually is more true to what we would acquire during experiments. Figure 3.11b shows the first 0.5 ms of the synthetic SM-signal using randomized m_i values. Although the frequency of these fringes remains largely constant throughout the plot, we observe a heavy

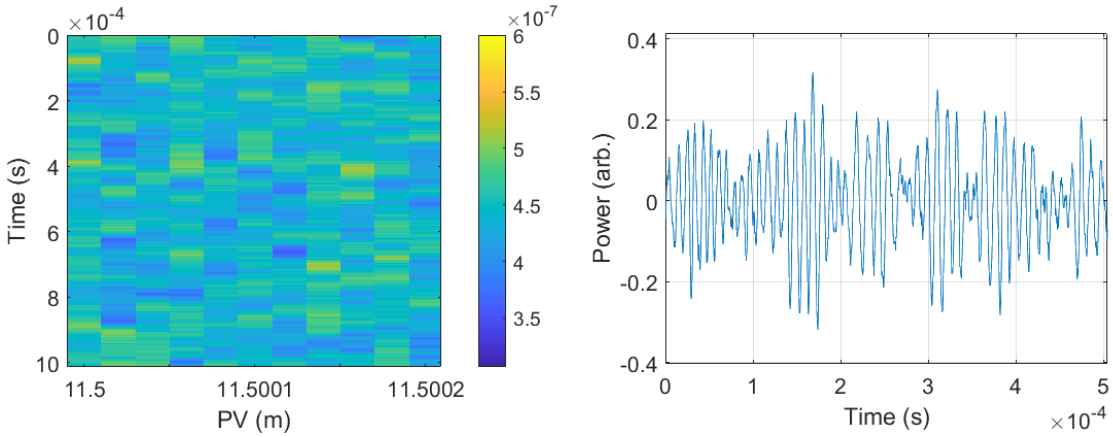

(a) Randomly generated m_i parameter values

(b) Synthetic SM-signal

Figure 3.11: **Left**: Zoom on randomly generated m_i values for the first 11 particles (x-axis) in the PV during 1 ms (y-axis). **Right**: Synthetic SM-signal with randomly generated m_i for each particle.

modulation of their amplitude.

Figure 3.12 shows an FFT of the same signal that produced the spectrum in in Fig.3.8a, but with an individual modulation index m_i for each particle. The spectrum contains a lot more noise and the signal to noise amplitude is about half of the signal to noise amplitude in Fig. 3.8a.

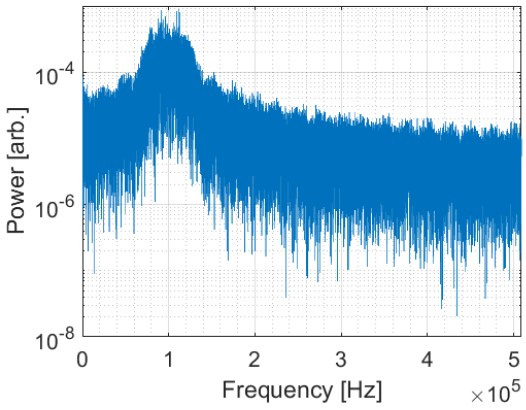

Figure 3.12: FFT of simulated SM signal generated from the velocity distribution in the dataset in Fig. 3.7. The modulation index m_i for each particle is randomly generated

To recover the acoustic data from the SM signal, the signal now has to be demodulated. The procedure is explained in the following section where we will process the signal generated in this section.

3.5 Signal Processing

3.5.1 Weighted Moments

A robust way to efficiently calculate the instantaneous Doppler frequency in an SM-signal is needed. The weighted moment method calculates the average frequency in a spectrum with respect to it's power within a chosen frequency range [53]. In short, the weighted moment is the ratio of the first order moment to the zeroth order moment as shown in eq. (3.19). Several research papers on micro fluidics and flow measurements have been published using this method to find the Doppler frequency in an SM-signal.

Finding the Doppler frequency generated from a flow of particles in air is inherently similar to finding the Doppler frequency in microfluidic measurements. The weighted moments method can thus be applied to find the Doppler frequency in our SM-signals.

$$\bar{f} = \frac{M_1}{M_0} = \frac{\int_{f_1}^{f_2} f \cdot P(f)\, df}{\int_{f_1}^{f_2} P(f)\, df} \tag{3.19}$$

Here $\bar{f}$ is the average frequency in a spectrum, f_1 and f_2 delimits the frequency range upon which to calculate the weighted moments and $P(f)$ is the power of the frequency f. An example of how the weighted moment method works is shown in Fig. 3.13. Here a synthetic SM-signal is generated from a virtual particle flow with velocity $v_0 = 0.13$ m/s in the direction of the laser. The flow is modulated by a $\Delta p_{\max} = 5.159$ Pa zero to peak acoustic wave, and noise is added to the signal through randomly generated modulation indexes m_i. The power spectrum shown in Fig. 3.13 is of a section of the synthetic SM-signal: the first 0.2 s. We see a Doppler lobe with it's peak around the 190 kHz mark with a full width half maximum (FWHM) spread of around 54 kHz.

Through the weighted moments method we have calculated that the average frequency $\bar{f} = 188$ kHz in this example. From here we extrapolate and see that when the Doppler frequency f_{D} changes, so does $\bar{f}$. There are however some pitfalls. If there is no clear Doppler frequency, or if the SNR of the Doppler Peak is low, the result may be erroneous. Remember, $\bar{f}$ is the *average* frequency with respect to the power of the frequencies in the frequency range $[f_1, f_2]$. If other frequencies within this range exhibit a significant power compared to the rest, $\bar{f}$ will be drawn towards these frequencies.

In Section 3.5.3 we will cover the processes of demodulating SM-signals generated from particles with constant and non-constant velocities. We will also cover a method of SM-signal spectrum-weighting in order to more easily detect and calculate the Doppler frequency using weighted moments.

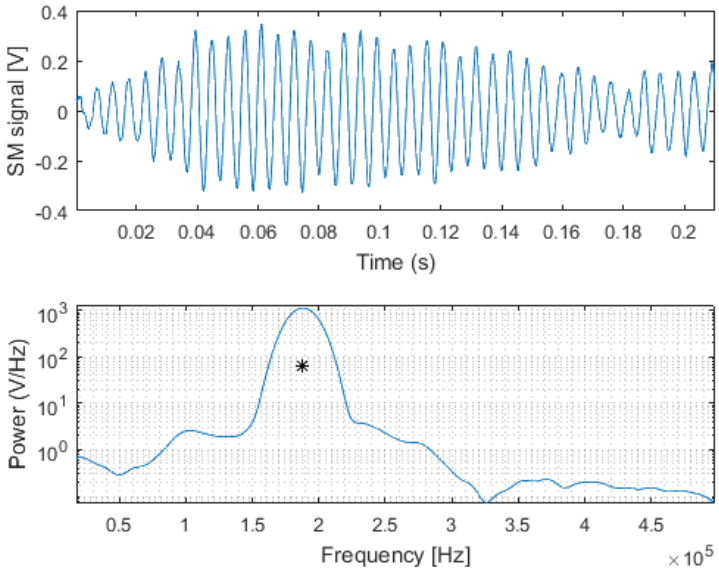

Figure 3.13: Visualization of weighted moment calculation on section of SM signal. Top plot: SM signal plotted in blue. Bottom plot: Power spectrum of the SM-signal. The average frequency $\bar{f} = 188$ kHz, is marked with a star.

3.5.2 Frequency Limits

As an acoustic wave passes through the particle flow, the particles are accelerated then slowed down, periodically with the frequency of the acoustic wave, and the Doppler frequency shifts up and down. The acoustic information is thus recovered through analysis of the Doppler peak's change in time using the method discussed in the previous section.

This implies that we need to calculate the Doppler frequency (ideally several times) over the course of an acoustic period in order to sample the velocity variation in the particle flow.

One particular point which has the potential to make life difficult when calculating a Doppler frequency is that the acquisition window over which this calculation is done must cover a sufficient number of Doppler periods. When there is noise in the signal, as is the case during experiments, few periods makes it difficult to correctly resolve the Doppler frequency.

This brings about a limitation on the minimum Doppler frequency (or flow velocity), necessary for the correct demodulation of a given acoustic signal. Let consider an acquisi-

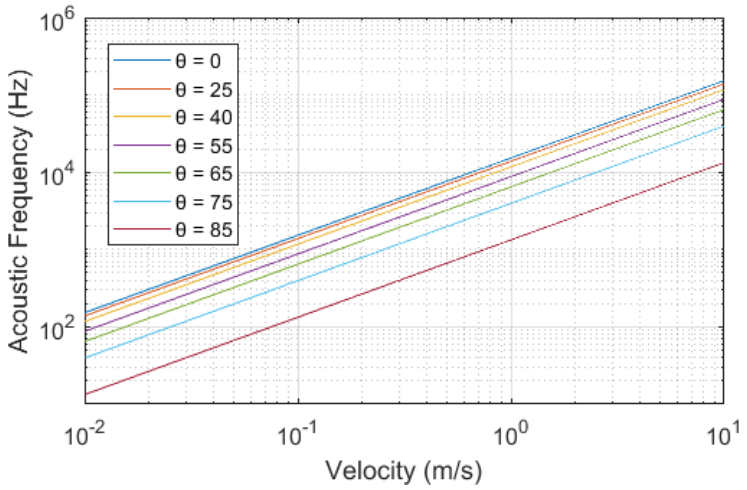

Figure 3.14: Maximum allowed acoustic frequency as function on flow velocity v_0 and incident angles θ.

tion window T_{aq}

$$T_{\text{aq}} > 50T_{\text{D}} < \frac{T_{\text{a}}}{10} \tag{3.20}$$

where T_{D} is the Doppler period and T_{a} is the acoustic period. Based on experience, we propose to set the limit that this window must contain at least 50 periods in order to properly calculate the frequency. We also consider that it is required a minimum of 10 measurements of the frequency per acoustic period. These values are empirical and subjective, based on our own experience using the weigthed moment method, and probably lower values could be acceptable. However it is important to remember that we intend here to reconstruct acoustic waves which in the real world are not perfectly periodic and stationary.

This effectively imposes the Doppler frequency to be superior to 500 times the acoustic frequency. Between consecutive spectral analysis' on consecutive temporal windows, we overlap the windows by 90%. Thus we can reduce the Doppler frequency to

$$f_{\text{D}} > 50 \times f_{\text{a}} \tag{3.21}$$

The Doppler frequency is in turn a product of the input angle θ between the laser and the particle flow direction, and the target's velocity, as we observe in eq. (1.49). Thus we can plot the upper limits of detection for an acoustic frequency based on the velocity of a particle flow and the angle of intersection between the laser and the flow.

Figure 3.14 shows the limits on f_{a} as a function of particle velocity, at different incident angles. This shows that for high acoustic frequencies, the flow velocity must be high

in order to generate a sufficient number of Doppler periods. This can be optimized by adjusting the incident angles of the laser with regard to the flow direction.

3.5.3 Demodulation Process

The first step to demodulate the SM-signal and retrieve the acoustic information, is to detect the Doppler peak. A frequency analysis of the entire SM-signal will provide us with a Doppler lobe containing a mix of all the Doppler frequencies f_{D} and it's shifts throughout the acquisition. The center of the peak corresponds to v_0. By performing a frequency analysis using Welch's method the resulting frequency spectrum is smooth and contains a clear Doppler peak as seen in the first step in Fig. 3.15. The diagram in Fig. 3.15 contains an overview of the steps performed to demodulate the SM-signal.

After the central Doppler frequency is found, the frequency window delimited by f_1 and f_2 is determined. These frequencies constitute the frequency window on which to calculate the weighted moments in the next step. The frequencies are either set to some static value such as $\bar{f} \pm 50$ kHz (or some other value), or dynamically set to span some percentage on either side of $\bar{f}$. The dynamic configuration gives

$$f_1 = \bar{f} - X \times \bar{f} \tag{3.22}$$

$$f_2 = \bar{f} + X \times \bar{f} \tag{3.23}$$

where X is some number from 0 to 1. This will widen the window as $\bar{f}$ increases and shorten the window when $\bar{f}$ decreases.

The latter frequency window configuration is advantageous as it dynamically ascribes a window on which to calculate the weighted moments. The Doppler frequency lobe widens as f_{D} increases and shortens as f_{D} decreases. For high f_{D} a wider frequency window ensures that the entire Doppler lobe is accounted for when calculating the weighted moments, and vice versa for low f_{D}.

After the initial frequency window configuration, the time domain signal is divided into short temporal windows. The frequency window constituted by f_1 and f_2 is shifted for each time $\bar{f}$ is calculated on one of the temporal signal windows. Thus, if f_{D} were to change due to turbulence or other factors, we are ensured that the frequency window follows.

The temporal window length has to be chosen with care as to optimize the number of samples and fringes in regards to the acoustic period. An overlap of around 90% is chosen between the consecutive windows. Equation (3.19) is subsequently performed on each time domain window as seen in Fig. 3.15, step 2). The output from eq. (3.19) is stored and can be represented as a set of oscillating Doppler frequencies as shown in step 3).

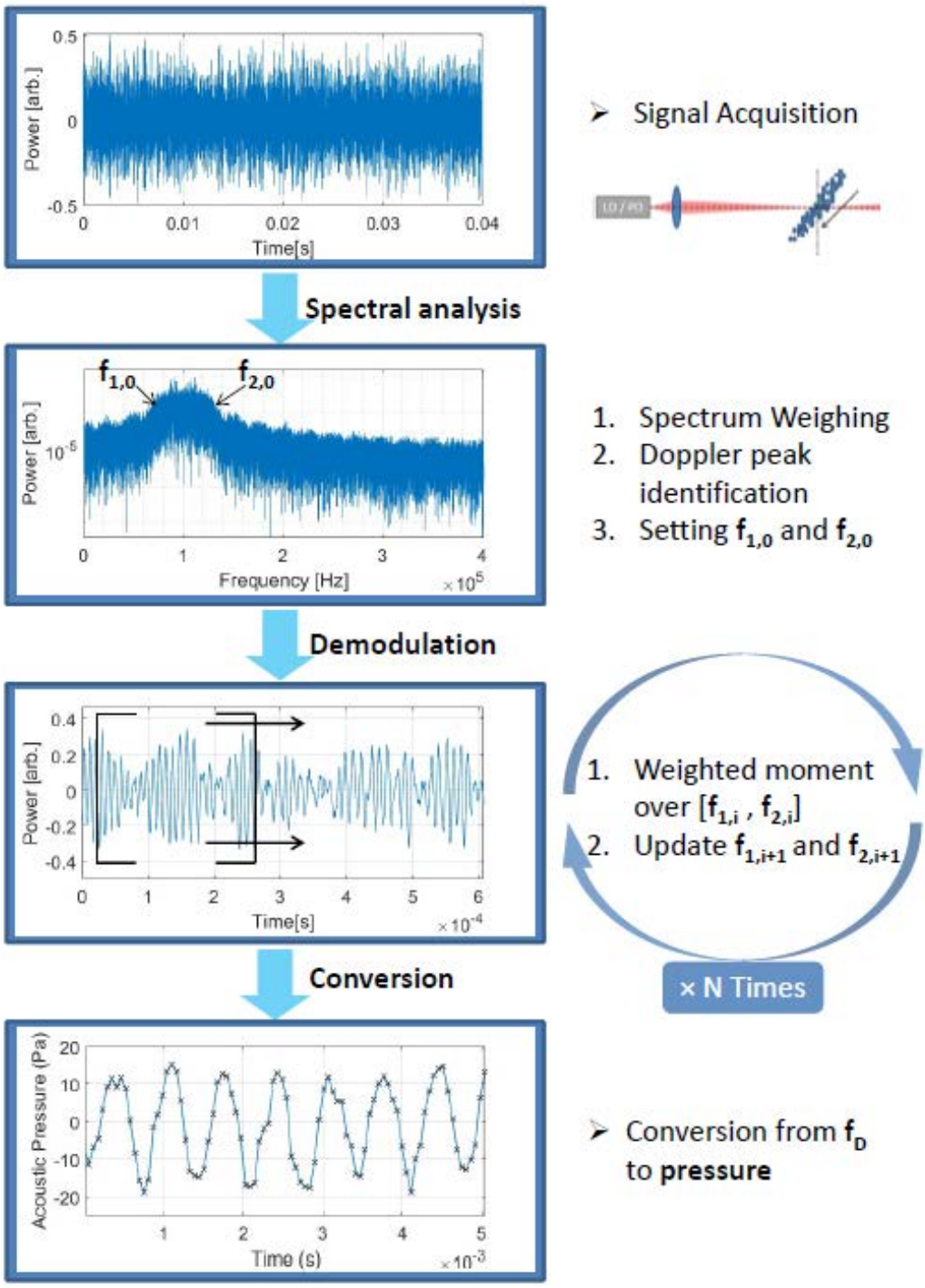

Figure 3.15: Diagram of acoustic frequency recuperation through demodulation using weighted moments on the time domain signal containing the modulated Doppler frequency

The 4^{th} and last step in Fig. 3.15 shows the FFT of the data output from the weighted moments. We observe a peak at the acoustic frequency (Which is 1 kHz in this example). The synthetic signals used to produce the data in Fig. 3.15 are clear and easy to demodulate. The temporal change of f_{D} is easy to follow only by looking at the plot, rendering the frequency analysis in step 4) less important. Real signals may be more noisy and complex. Thus a frequency analysis of the demodulated signal is an efficient way to determine the acoustic frequency and amplitude.

3.5.3.1 Demodulation Using Weighted Spectra

The weighted moment is affected by the power of the different frequencies in the spectrum. A completely flat spectrum containing nothing but the Doppler frequency is therefore favorable[1] when demodulating the signal. Any unwanted frequencies of significant power apparent in the spectrum, will bias the outcome of $\bar{f}$.

The analog acquisition system connected to the laser is responsible for retrieving and amplifying the laser signal before it can be store numerically. It has it's own frequency response and will add it's own distortions and noise to the laser signal.

Figure 3.16a shows a frequency analysis using Welch's method on two sensor signals. The first one, in blue is the reference spectrum, P_{ref}, of the acquisition system. It is made by acquiring the sensor signal in the absence of a particle flow and acoustics. It's the unperturbed laser signal reflecting only the natural frequencies present in the acquisition system. The red curve is the spectrum of an SM-signal, P_{sig}, acquired from an aerosol flow with acoustic waves traveling through it.

The shape of P_{ref} as shown in Figure 3.16a exhibits a powerful low-frequency response before flattening out between 150 kHz and 450 kHz. It then drops at ~ 450 kHz which is the amplifier cutoff frequency.

The shape of P_{sig}, although with a higher baseline of noise, has the same general shape plus the addition of a Doppler lobe centered around 120 kHz. The low frequencies generated from the acquisition system are present and will inevitably bias the weighted moment calculation. The average frequency $\bar{f}$ will be drawn to the left, towards the lower frequencies due to their high power.

The solution to this problem is quite elegant and avoids the use of filters: When demodulating an SM-signal, only the movement of the Doppler peak is recorded. Therefore we can in essence "straighten out" P_{sig} by applying a set of weights to each of the bins. The weights are applied to each bin in the spectrum, and the amplitude of each weight is

[1]Such as the spectra in Figures 3.8a and 3.12

governed by P_{ref}.

The weighing is done through the logarithmic subtraction of the reference spectrum P_{ref} from the carrier spectrum P_{sig}, which effectively means dividing (in linear) P_{sig} by P_{ref}:

$$P_{\text{W}}(\text{dBm}) = P_{\text{sig}}(\text{dBm}) - P_{\text{ref}}(\text{dBm}) \Rightarrow \boxed{P_{\text{W}} = \frac{P_{\text{sig}}}{P_{\text{ref}}}} \tag{3.24}$$

Where P_{W} is the weighted spectrum. The resulting spectrum in Fig. 3.16b shows a removal of the low frequencies without touching the Doppler lobe as would be the case with classical filtering.

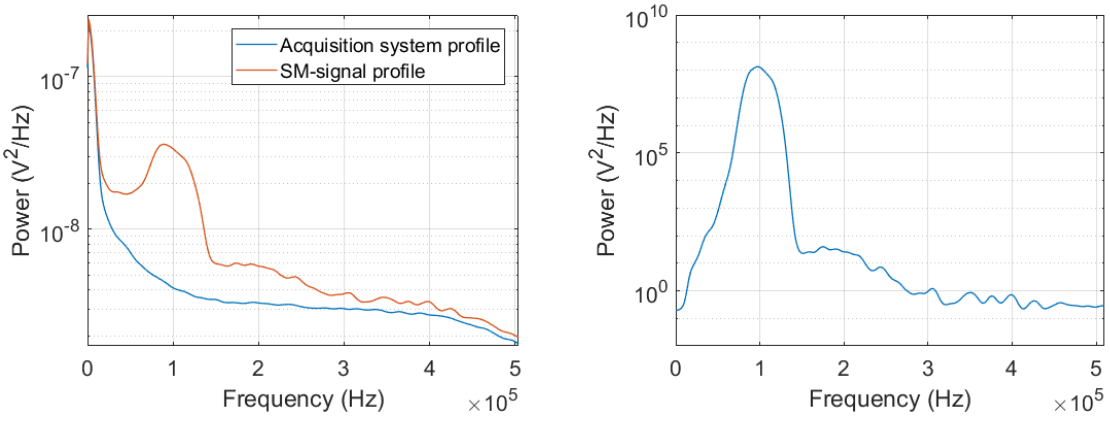

(a) Signal and system frequency spectra

(b) Weighted frequency spectrum.

Figure 3.16: **Left**: Frequency spectrum of acquisition system with and without SM-signal generated from aerosol flow. **Right**: Weighted frequency spectrum of SM-acquisition with Doppler frequency from particle flow.

The process of weighing the SM-signal power spectrum using the noise spectrum is applied during demodulation. Essentially eq. (3.24) is applied to each temporal window. That is to say, before each weighted moment calculation, the spectrum itself is weighted using eq. (3.24), leaving only the Doppler frequency f_{D}.

3.6 Experiments

The performance of the acoustic LIDAR depends on several parameters, among which the particle's movement in response to acoustic waves is a major factor. The first set of experiments is designed to study the frequency response of the system for a range of acoustic frequencies.

Preliminary experiments are performed at close range. Then the system is expanded and we acquire signals at a distance of 11.5 m. At longer distances the system may become instable. An experiment is made to study the effects of target reflectivity. The experiment shows that there is an optimal configuration, where the signal to noise amplitude is at it's highest.

After this preliminary study, we proceed to acquire acoustic signals at a distance of 11.5 m from the laser source. Through these experiments we we validate the OFI sensing scheme in a LIDAR configuration as an acoustic detector. We also highlight challenges related to long distance acquisitions and repeatability.

3.6.1 System Demonstrator: Frequency Response Characterization

A Thorlabs 1310P5DFB laser diode with wavelength $\lambda = 1310$ and an integrated photo diode is mounted in on a PCB circuit board attached to a Thorlabs 30 mm rectangular cage. The circuit board contains a custom laser driver circuit and circuit to amplify output signal from the photo diode. The electric signal from the amplification circuit is recorded by a Tektronix DPO 4034 Oscilloscope. The oscilloscope is controlled by Matlab.

A Thorlabs C245 TMD-C aspheric lens focus the laser beam at distance of 73 cm. The point of measure, called the probe volume (PV hereafter), is placed at the exit of an aerosol conduct that points vertically towards the ground. The laser beam intersect the PV at an incident angle of $\theta = 80°$ to the flow traveling direction.

The aerosol is generated by a JM Liquifog Ultrasonic Liquid Atomizer that creates a mist of water droplets, where the most frequent droplet size is expected to be $\varnothing \approx 3$ μm. The mist generator operates by focusing ultrasonic waves of frequency $f_{\mathrm{a}} = 1.6$ MHz in a focal point positioned 50 mm above the vibrating surface of the device. The device is submerged in a container under 50 mm of water as shown in Fig. 3.17, and the amount of mist is controlled by a dedicated circuit. The container is sealed but contains an exit point for the water droplets and an entry point for an air current. A velocity regulated ventilator placed in the entry point of the container controls the velocity of the aerosol.

The aerosol flows through a silicone conduct of diameter $\varnothing = 8$ mm and length 175 cm and exits vertically towards the ground through the laser beam. The long neck of the particle guide reduces turbulence in the flow at exit points, where it is close to laminar flow.

A Visaton W 200 speaker is placed at 25 cm from the PV, at a $\theta_2 = 55°$ angle to the laser beam, facing the PV. The speaker is driven by a dynavox VT 80 stereo amplifier

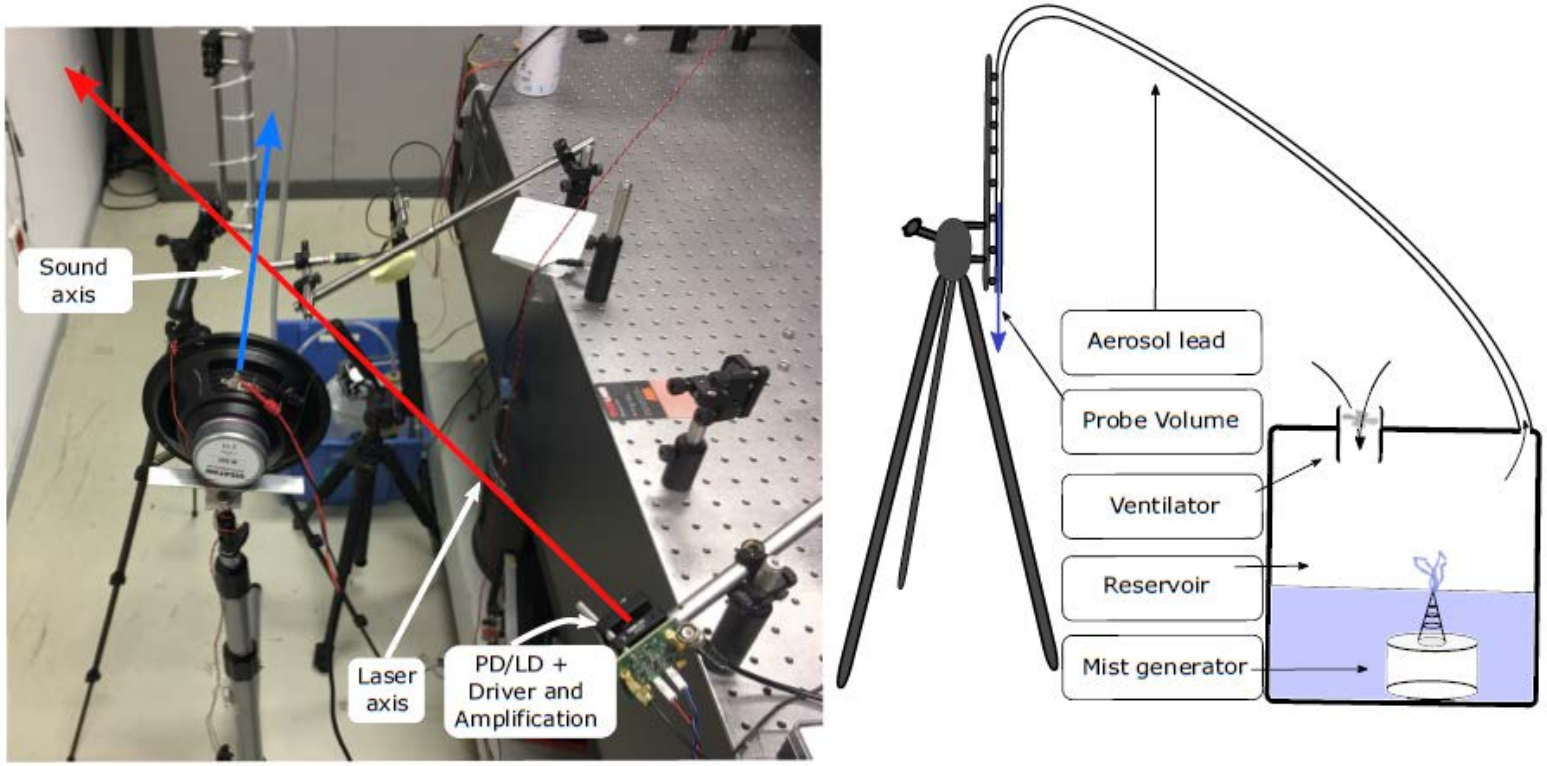

Figure 3.17: Photo of the experiment and schema of mist generation.

which takes it's input signals from a computer running Matlab.

A G.R.A.S 45AE Class 1 microphone is placed next to the PV, perpendicular to the laser axis, to record the sound waves. The microphone is powered by a DT9837 USB acquisition card, and the output signal from the microphone is recorded both by the DT9837 and the Tektronix DPO 4034 Oscilloscope.

Figure 3.17 shows a schema of the mist generation system and image of the experimental setup with lines marking the laser and sound axes. The image also show a number of objects and obstacles surrounding the PV, such as walls and experimental equipment, contributing to the perturbation of the acoustic waves.

A sequence of 11 acquisitions are made at acoustic frequencies ranging from 50 Hz to 3 kHz. The continuous sound waves are generated by Matlab where the output signal amplitude is tailored so that the audio amplifier and speaker outputs the same power at all frequencies. The sampling frequency is set to $f_s = 25$ MHz, and $1 \cdot 10^6$ points are recorded.

The recorded signals are loaded into Matlab filtered numerically with a 3^{rd}-order Butterworth lowpass filter with cutoff frequency $f_c = 500$ kHz to avoid aliasing. The signals are then downsampled by a factor 5 resulting in a new sampling frequency $f_s = 5$ MHz.

To obtain the acquisition system's noise profile, an "empty" acquisition is made. The laser beam goes through empty air: There is no particle flow or sound present to perturbe the laser. The only frequencies present in such a signal are those proper to the acquisition system. The frequency spectrum of the empty SM-signal is calculated using Welch's method using a $\sim 99\%$ overlap between consecutive windows.

Figure 3.18 shows the resulting power density estimation (the standard output when using Welch's method) of the frequency spectrum. The spectrum exhibits a low-frequency response with an additional peak at 85 kHz before flattening out around 150 kHz.

A weighted moment calculated on this spectrum will automatically be biased towards the lower frequencies of strong amplitude on the left hand side of the spectrum. Using the acquisition system's frequency profile, we can process the following SM-signals by weighing the frequency spectra according to this curve.

Care has to be taken when calculating the reference spectra. A large number of windows in Welch algorithm is in general advantageous in order to average out the value of each bin in the spectrum, and thus increase confidence in the computed value. But many windows mean they must be relatively short. If the windows are too short the frequency resolution may become inadequate. The number of points in the output spectrum is also an important factor. If there are too few points, we may loose information such as the 85 kHz peak in Fig.3.18. This spectrum was calculated using a window length of 512 points with an overlap

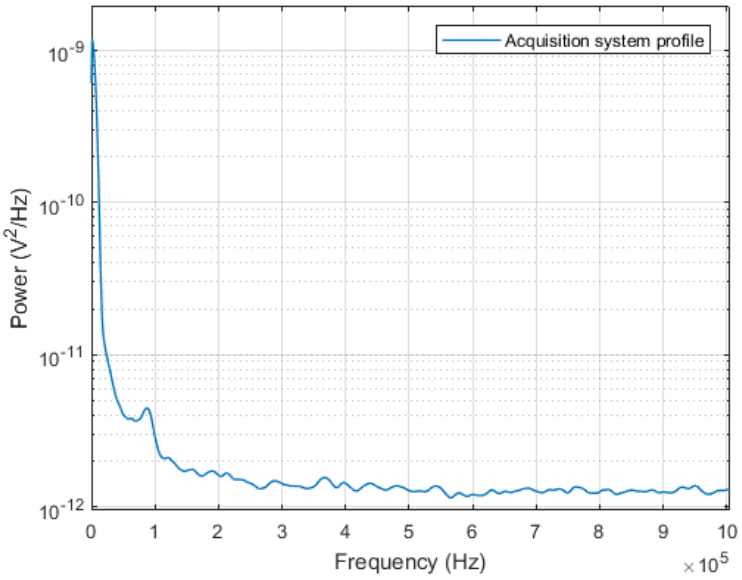

Figure 3.18: Frequency profile of acquisition system

of 506 points. When windows are shorter than this, we lose frequency resolution in the spectrum.

3.6.1.1 Results and Discussion

The system's frequency response to acoustic waves is discussed in this section. The response is affected by several parameters, ranging from the shape of the frequency spectrum to the length of a given signal. For the sake of explaining the demodulation process, we will consider the acquisition of an 800 Hz sound wave with amplitude 7.63 pA zero to peak.

The red curve in Fig. 3.19 is the frequency profile of the SM-signal acquired in the experiment. The spectrum is calculated using Welch's method and contains all of the Doppler frequencies present in the signal throughout the acquisition. Using the frequency profile from the acquisition system we apply a set weights to the spectrum as outlined in Section 3.5.3.1. The Doppler frequency $f_{\mathrm{D},0} = 234$ kHz is marked by a triangle in Fig. 3.20 and corresponds to $v_0 = 0.94$ m/s.

The shape of the curve in Fig. 3.20 shows a distribution of particle velocities throughout the particle flow. Ramirez et al [91] showed that in a microchannel, there is a distribution of particle velocities throughout the flow. At the edges of the channel, the velocity was 0, and it increased to it's maximum velocity in the center of the channel. This was reflected in the Doppler frequency distribution which ranged from 0 to $f_{\mathrm{D,max}}$. The laser was focused

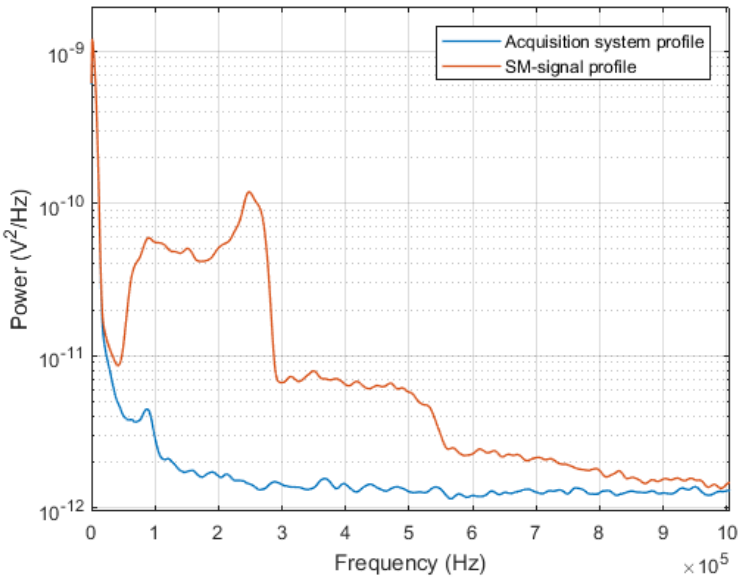

Figure 3.19: Frequency profile of acquisition system and SM-signal

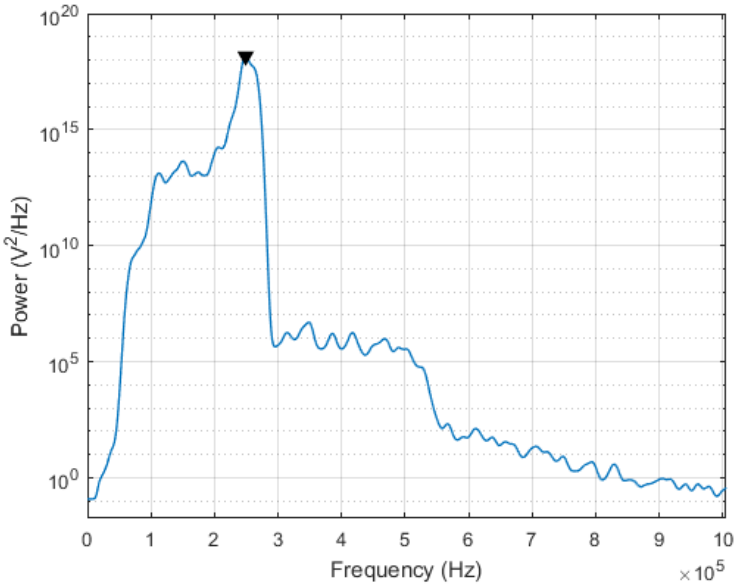

Figure 3.20: Frequency profile after weighing

at the center of the channel where the particle density was highest and their velocity the fastest, which lead to $f_{\mathrm{D,max}}$ having the highest signal amplitude.

In our experiment the particles at the edges of the flow are moving slower than in the center, where the laser beam is focused. However, the velocity is not 0. Similar to Ramirez et al's paper, there is a contribution of frequencies before the main Doppler lobe from these slower particles. The Doppler frequency amplitude associated with the slower particles are lower than the main lobe due to two factors. Firstly, the laser is if focused in the center of the flow, thus backscattering less light from the slower particles. Secondly, the density of the faster particles, in the center of the flow, is higher than at the edges. As such there are more photons returning from fast particles than from the surrounding area.

By looking at the spectrogram we can directly observe how the Doppler frequency oscillates in time. Each line in the spectrogram in Fig. 3.21 corresponds to a weighted output spectrum at the time t shown on the left Y-axis.

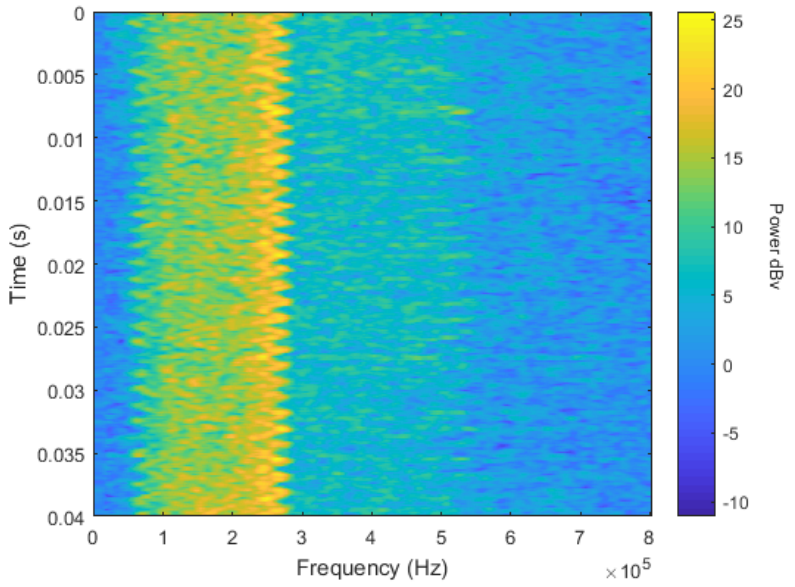

Figure 3.21: Spectrogram of SM-signal from particle flow entrained by a 800 Hz acoustic wave. Average flow velocity $v_0 = 0.94$ m/s

We clearly recognize the shape of the initial weighted spectrum from Fig. 3.20 where there is a plateau before the Doppler peak. Both the plateau and the Doppler peak oscillates throughout the acquisition and one oscillation period is 1.3 ms which is the period of an 800 Hz wave.

After determining $f_{\mathrm{D},0}$ the time domain SM-signal is divided into shorter sections on which to calculate the weighted moments. The sections overlaps $\sim$ 90%. The number

of samples per section depends on the acoustic frequencies. In general there should be fewer samples in a section than samples during a half acoustic period. Furthermore, it is computationally advantageous that the number of samples per section is a power of two. This renders the frequency analysis more efficient as the FFT algorithms are optimized for powers of two.

The length of the windows is calculated by

$$L_{\text{win}} = 2^{\text{nextpow2}\left(\frac{\frac{N_{\text{samples}}}{N_{\text{acoustic}}}/2}{N_{\text{win}}}\right)} \tag{3.25}$$

Where N_{samples} is the total number of samples in the signal, N_{acoustic} is the total number of acoustic periods in the acquisition, the factor 2 is for the half period and N_{win} is the number of windows per half acoustic period. In other words, the length of the window will be rounded up to the power of two the the closest to

$$\frac{\frac{N_{\text{samples}}}{N_{\text{acoustic}}}/2}{N_{\text{sections}}}$$

When the window length L_{win} is set, the weighted moment can be calculated on each consecutive window. To do this, first the frequency spectrum is calculated using Welch's method on the first time window. The output spectrum is then weighted using the acquisition system's noise profile as described earlier and shown in eq. (3.24) and Figures 3.19 and 3.20.

When we start the demodulation using weighted moments, the very first frequency window is based on the weighted Doppler spectrum shown in Fig. 3.20. $f_{1,0}$ and $f_{2,0} = \bar{f}_0 \pm 0.3 \cdot \bar{f}_0$, where $\bar{f}_0$ is the peak in Fig. 3.20.

$$\bar{f}_i = \frac{M_{1,i}}{M_{0,i}} = \frac{\int_{f_{1,i}}^{f_{2,i}} f \cdot P_{\text{W},i}(f)\, df}{\int_{f_{1,i}}^{f_{2,i}} P_{\text{W},i}(f)\, df} \tag{3.26}$$

Where i denotes the i^{th} section out of a total of N consecutive sections on which to calculate the weighted moment $\bar{f}_i$. The i_{th} weighted power of the frequency f is denoted $P_{\text{W},i}(f)$. For the consecutive frequency windows the upper and lower frequency limits are adjusted to $f_{1,i}$ and $f_{2,i} = \bar{f}_i \pm 0.3 \cdot \bar{f}_i$.

The i^{th} weighted moment will dictate the frequency delimitation for the $i+1^{\text{th}}$ weighted moment. We assume that the Doppler frequency will not change more than 30% in any direction between iterations. This allows the demodulation algorithm to freely follow the evolution of the Doppler frequency without the risk of it "loosing" the Doppler peak.

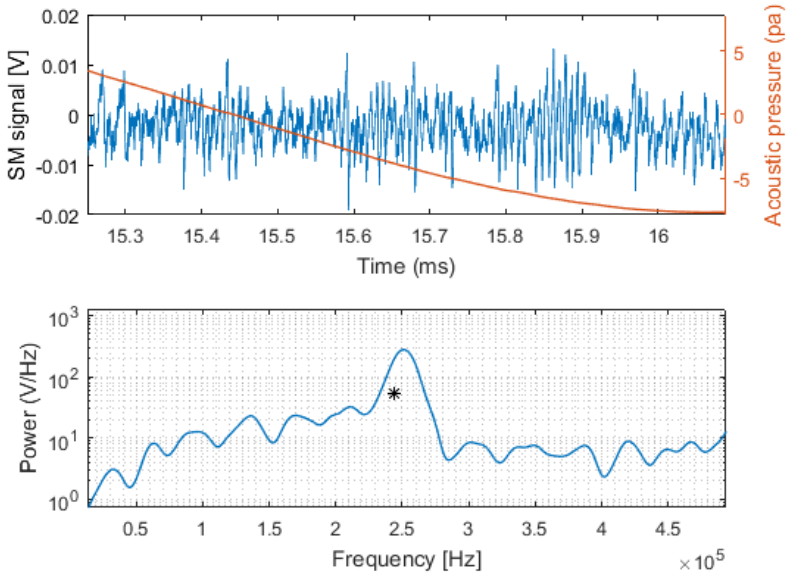

Figure 3.22: A step in the demodulation process. Top plot: In blue: Section of SM-signal on which to calculate the weighted moment. In red: Acoustic pressure. Bottom plot: In blue: Frequency spectrum of SM-signal. Black Star: Weighted moment calculated on current spectrum.

Figure 3.22 shows a step in the demodulation process. The time-domain window in the upper plot shows a section of SM-signal in blue, with the acoustic pressure overlapped in red.

The bottom plot shows the weighted spectrum of the section of the SM-signal in the upper plot. The black star denotes the weighted moment $\bar{f}_i = 243.5$ kHz calculated between $f_{1,i} = 169$ kHz and $f_{2,i} = 314$ kHz. For the next frequency window the delimiting frequencies will be $f_{1,i+1} = 170.9$ kHz and $f_{2,i+1} = 317$ kHz, based on the current weighted moment $\bar{f}_i$.

We observe that the weighted moment is not perfectly centered underneath the peak of the Doppler lobe. It is slightly biased towards the left. This is due to the impact of the slower moving particles in the Doppler spectrum, "drawing" the weighted moment towards the left.

This small bias should not affect the amplitude of the mean Doppler peak variation $\Delta f_{\mathrm{D,max}}$. It can be considered as a first approximation that the entire spectrum is shifted left and right by the acoustic wave. Thus, this small offset is not affecting the demodulation.

The demodulated signal is an ensemble of weighted moments $\bar{f}_i$, oscillating around the

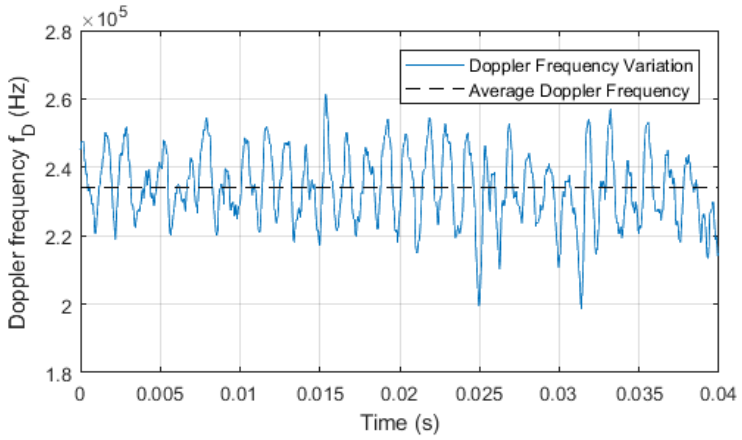

Figure 3.23: Demodulated Doppler signal

average weighted moment $< \bar{f} >= 234$ kHz. The result is shown in Fig. 3.23 where the demodulated Doppler signal oscillates around the average Doppler frequency, marked by a black line.

There is clear periodicity in the signal, but some noise is added during demodulation. Some of the amplitudes are also very low or very high. These dispersions in the demodulation result are attributed to perturbations in the shape of the spectrum. Sometimes the power of the Doppler peak is diminished, resulting in a biasing of the Weighted moment. This is shown clearly in the 25 ms and 31 ms points in Fig. 3.23, where the amplitude is around 20 kHz below the other peaks. Figure 3.24 shows the Doppler spectrum at the negative peak at 25 ms. There is a clear loss of Doppler peak, and the lower frequencies bias the $\bar{f}_i$ towards the left. Similar situations are responsible for perturbations throughout the signal.

To calculate the acoustic amplitude, we must first convert the weighted moments to velocity. In essence we are only interested in the change in velocity, $\Delta v_{\max}$ around v_0, and

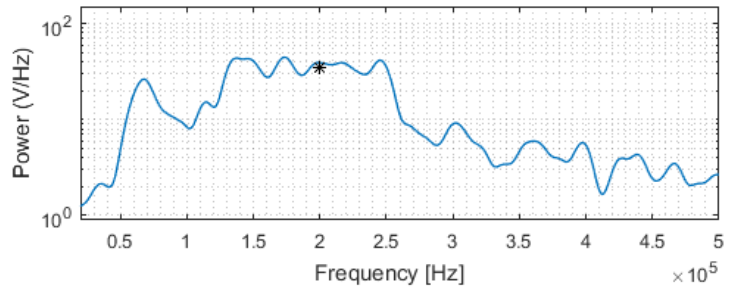

Figure 3.24: Doppler biasing by low frequencies

not so much v_0 itself. Therefore we center the weighted moments from Fig. 3.23 around 0 by subtracting the average frequency $< \bar{f} >$ from each of the weighted moments $\bar{f}_i$.

$$\bar{f}_{\text{zerocenter}} = \bar{f}_i - < \bar{f} > \tag{3.27}$$

Where $\bar{f}_{\text{zerocenter}}$ thus becomes the frequency offset from 0.

In calculating a Doppler frequency from velocity data, the different incident angles of the laser beam and the sound wave must be taken into account. The laser beam incident angle on the flow $\theta_1 = 80°$ is used when calculating the average Doppler frequency $f_{\text{D},0}$ from velocity data. The Doppler frequency variation Δf_{Dmax} is calculated using the incident angle of the acoustic waves on the laser beam $\theta_2 = 55°$.

This is because the oscillatory movement entrained in the particle flow, is along the acoustic axis. Thus it's contribution to the Doppler frequency has to be calculated using it's own incident angle on the laser beam. The Doppler frequency is this calculated as

$$f_{\text{D}} = \frac{2v_0 \cos\theta_1}{\lambda_{\text{laser}}} + \frac{2\Delta v \cos\theta_2}{\lambda_{\text{laser}}} \tag{3.28}$$

where θ_1 is the laser beam's incident angle on the flow, and θ_2 is the sound wave's incident angle.

Thus, when going the other way around, calculating velocity from Doppler frequency, we have to apply the same angles respectively. The mean velocity is calculated using the mean Doppler frequency and θ_1, and the velocity oscillation is calculated using θ_2 and the Doppler frequency variation.

Since we've centered the Doppler frequency variation around zero in eq (3.27), we only need to consider the second term in eq. (3.28) when calculating the velocity variation. We solve for Δv and obtain

$$\Delta v = \frac{\bar{f}_{\text{zerocenter}} \times \lambda}{2\cos(\theta_2)} \tag{3.29}$$

Where we've replaced f_{D} by $\bar{f}_{\text{zerocenter}}$ as it's the deviation from 0 we're interested in, and $\theta_2 = 55°$. Once the velocity data is calculated we can apply the acoustic model for converting particle velocity to pressure, as outlined in Section 3.2. The acoustic pressure is calculated using

$$p = \rho c_{\text{air}} v \tag{3.30}$$

Where the speed of sound in air is $c_{\text{air}} = 340$ m/s, and the air density $\rho = 1.23$ kg/m^3.

The result shown in Fig. 3.25 displays the demodulated SM-signal converted to acoustic pressure using eq. (3.30) issued from the model. The signal, plotted in blue, is overlapped with the acoustic signal recorded by the reference microphone.

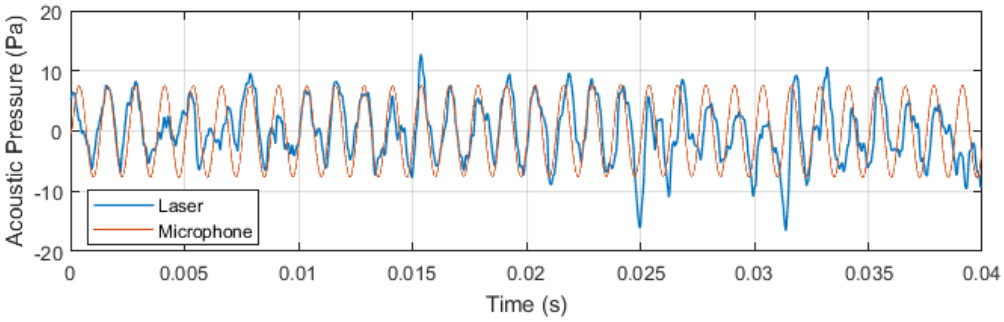

Figure 3.25: Demodulated SM-signal converted to pressure variation

The average zero to peak acoustic pressure p_{avg} is calculated by detecting the positive and negative peaks, separated by an acoustic period. The average peak to peak value is then divided by 2. For this demodulation $p_{\text{avg}} = 6.59$ Pa zero to peak which is 14.9% below the actual value of 7.74 Pa zero to peak as measured by the microphone. The lower amplitude of 6.59 Pa is due to instabilities in the demodulation. We observe however in Fig. 3.25 that the amplitudes between 15 ms and 25 ms are very close to the actual acoustic values.

The "quality" or correctness of the demodulated signal can be estimated by a correlation coefficient $R \in [0, 1]$ which indicates the correlation between the signal recorded by the reference microphone and the demodulated result. Both curves are plotted in Fig. 3.25. The correlation coefficient is calculated using the Matlab *corrcoef* function which takes the two signals as input. The R coefficient of two random variables can be considered measure of their linear dependence [108]. If each variable has N scalar observations, the correlation coefficient can be defined as

$$R(A, B) = \frac{1}{N-1} \sum_{i=1}^{N} \left(\frac{A_i - \mu_A}{\sigma_A} \right) \left(\frac{B_i - \mu_B}{\sigma_B} \right) \tag{3.31}$$

Where μ_A and σ_A, and μ_B and σ_B are the mean and standard deviations, respectively. When R is unity it indicates that the two correlated signals are perfectly equal. In general a low R means that there is low correlation between the signal, which often means that the demodulation has been performed poorly. In our example, the correlation coefficient for the demodulated signal in Fig. 3.25 is $R = 0.736$, which is considered a good correlation.

Having validated that our demodulation method is efficient, we can study the system's response to a set of acoustic frequencies.

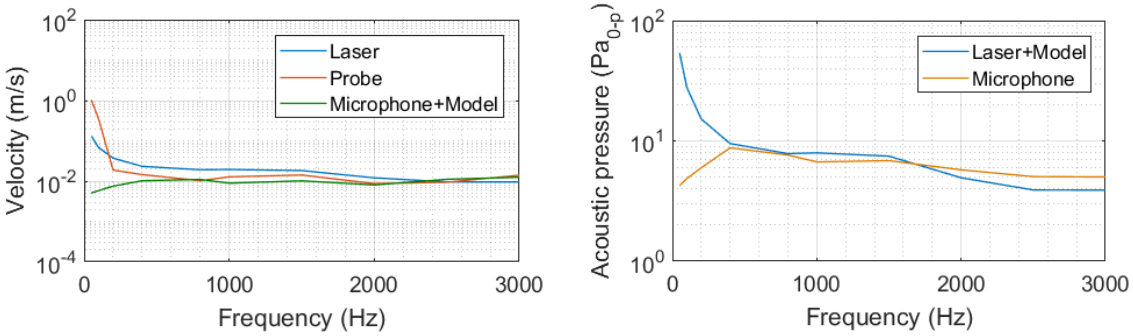

(a) Velocity comparison

(b) Pressure comparison

Figure 3.26: Comparison of velocity measurements and model for frequencies 50 Hz to 3 kHz. The blue line is the laser acquisition converted to velocity, the red line is the intensity probe and the green line is the model. **Left:** Blue: Laser acquisition converted to pressure using the model. Orange: Amplitude measurements by reference microphone.

System Frequency Response

Figure 3.26a compares velocity measurements from the intensity probe (red solid line) to the laser measurements - Doppler frequency converted to velocity (blue solid line) -, and to the model's output when it is fed with the acoustic pressures measured by the reference microphone (green solid line).

Figure 3.26b shows the demodulated laser signal converted to acoustic pressure using the model. The measurement result from the laser is compared to the corresponding acquisition by the reference microphone.

The velocity measurement from the intensity probe is similar to both the model and the laser measurement. We observe a good correlation between the laser's velocity measurement and the one made by the probe. As shown in Fig 3.26a the measurements and the model corresponds better in the frequency range 400 Hz to 3 kHz than for the lower frequencies of 50 Hz to 200 Hz.

The laser measures a slightly higher particle velocity in the frequency range 400 Hz to 2.5 kHz. This difference in the laser measurement and the probe can be attributed to the nature of the measurement: The probe measures the pressure variation between two points, whereas the laser measure a single point. The orientation of the probe affects it's measurement, and the position of the point of measure for the two acquisitions may be slightly different.

Figure 3.26b shows however that the demodulated laser signal converted to pressure using the model is similar in amplitude to the reference microphone in the frequency range

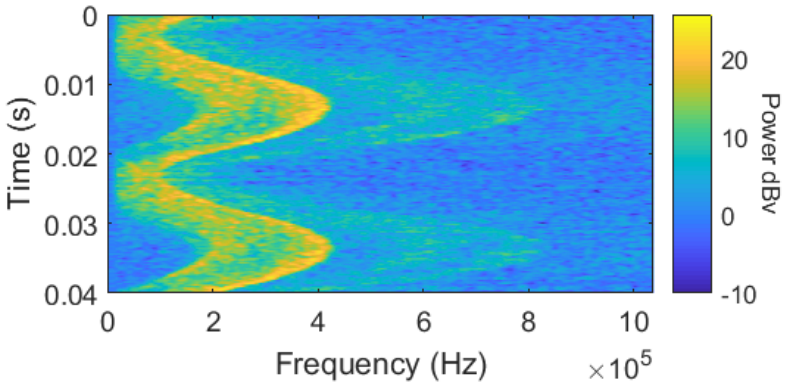

Figure 3.27: Spectrogram of Doppler signal with 50 Hz acoustic modulation

400 Hz to 3 kHz. The correlation coefficient of $R = 0.6$ is decent when calculated on the two pressure curves, where the greatest mismatch is in the lower frequencies. In the frequency range 400 Hz to 3 kHz, the correlation is $R = 0.92$.

The low frequencies, 50 Hz to 200 Hz, exhibits a powerful response to the acoustic pressure change. This is confirmed both by the intensity probe and by the laser measurement as shown in Fig. 3.26a. The acoustic amplitudes in the 50 Hz to 200 Hz range were slightly lower than in the 400 Hz to 3 kHz. Despite of this but the particle velocity was higher. Figure 3.27 shows a spectrogram calculated on the 50 Hz acquisition. Here we observe how the Doppler frequency varies strongly and is spread out throughout the acquisition.

The demodulation algorithm has reached a limit of operation in this case. The Doppler formula takes into account the particle velocity and it's incident angle to the laser beam, but whether the particle is moving backwards or forwards is not accounted for. As we can observe in Fig. 3.27 the particles vibrates back and forth with such an amplitude that the projection of their velocity along the optical axis changes direction.

When this happens, the Doppler peak will oscillate at $2 \times f_{\mathrm{a}}$. The demodulation algorithm is not equipped to account for this special case.

As mentioned in Section 3.2.2, the near-field of the speaker can perturb the particle velocity. At 50 Hz the acoustic wavelength $\lambda_{\mathrm{a}} = 6.68$ m and the near-field is estimated to be $z = 10.7$ cm. The near-field estimation is generic and does very likely deviate from the specific near field of the Visaton W 200 speaker used in our experiment.

When demodulating higher frequencies, there are other challenges to consider. As discussed in Section 3.5, for a given particle flow, when the acoustic frequency increases, there are fewer samples and fewer Doppler periods to work on per half acoustic period. This can pose problems when demodulating. A certain number of periods are necessary

per half acoustic period to properly estimate the Doppler frequency. This can be amended by increasing the flow velocity or decreasing the incident angle between the laser and the flow.

As an example we will study the 2 kHz acquisition, where the acoustic pressure was measured to 5.75 Pa zero to peak by the reference microphone and 5.61 Pa zero to peak by the laser.

Considering this acquisition, we examine the first aspect of the demodulation; the number of samples available and the window length. There are 1250 samples per 1/2 acoustic period in the SM-signal which leaves us with approximately $N_{\text{periods}} = 60$ Doppler periods per half acoustic period. This is found by

$$N_{\text{periods}} = f_{\text{D},0} \times \frac{T_{\text{a}}}{2} \tag{3.32}$$

Where the Doppler frequency is measured to be $f_{\text{D},0} = 241.7$ kHz and a half acoustic period $T_{\text{a}}/2 = 0.25$ ms.

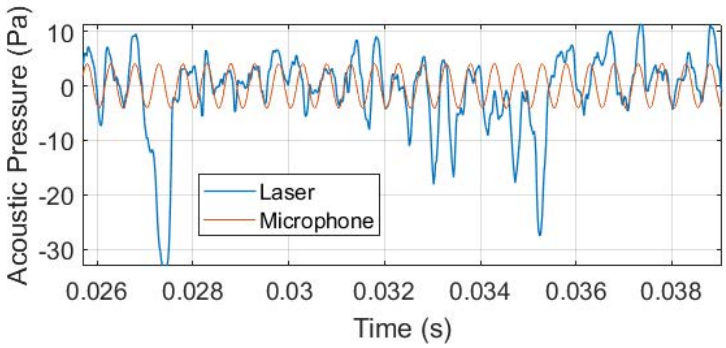

Figure 3.28: Demodulated SM-signal converted to pressure variation, acoustic pressure: 2 kHz

As discussed, the FFT algorithms prefer a power of 2 number of samples to be efficient, thus we chose a window length of 1024 samples with 930 samples of overlap. The 1024 samples-long window contains approximately 49 Doppler periods. The window spans almost the entire acoustic half-period, which is not optimal. However, this window length provides us with an adequate frequency resolution.

By diminishing the length to 512 points we cut the number of available periods per window in half, which has a negative impact on the frequency resolution. Thus we've opted for a window of 1024 points.

The demodulation algorithms are performed on the SM-signal and the result is shown in Fig. 3.28. The signal amplitude is unstable. Some acoustic periods are lost while others

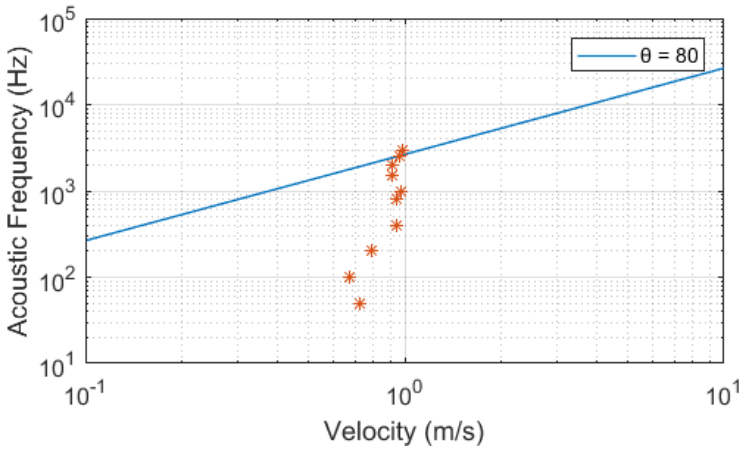

Figure 3.29: Theoretical limit (blue solid line) of maximum allowed acoustic frequency as function on flow velocity and incident angle $\theta = 80°$ between the flow direction and the laser beam. The red stars mark the particle velocity of frequencies 50 Hz to 3 kHz. The lowest star corresponds to 50 Hz and the highest corresponds to 3 kHz

are heavily amplified, with very low amplitude or out of phase.

The highly deviating acoustic pressures in some of the periods may be a consequence of the demodulation algorithm "loosing" the Doppler peak. In essence, the Doppler peak's power may be too low to effectively have an impact on the weighted moment. The average frequency $\bar{f}$ is as a consequence pulled towards higher powered frequencies.

The acoustic amplitude is measured to be 5.61 Pa zero to peak which is close to the input acoustic power of 5.75 Pa zero to peak. The signal correlation index $R = 0.064$, which is quite low. However, the average zero to peak amplitude of all the periods gives the correct demodulation amplitude. This indicates that when we demodulate a great number of periods, the average peak value approaches the correct amplitude, despite a poorly resolved Doppler frequency due to the short windows.

Figure. 3.29 is an extract from Section 3.5 and shows the theoretical maximum acoustic frequency we're able to demodulate with the current experimental setup. Above the blue solid line the number of Doppler periods per acoustic period, on which to estimate the Doppler frequency becomes too low. The red stars denotes the frequency demodulations from 50 Hz and up to 3 kHz.

From the plot we observe that the four highest frequencies: 1.5 kHz, 2 kHz, 2.5 kHz and 3 kHz are at the upper limit of what we can demodulate. As we approach this limit, the demodulation becomes less precise. When choosing a very high overlap such as is the case in this experiment, we effectively increase the number of points calculated. For the 2 kHz

signal, we calculated 23 points per acoustic period, which is two times the theoretical limit proposed in Section 3.5.

Despite the high overlap and thus high number of points per acoustic period, the signal was difficult to demodulate. This goes to show that a high overlap between consecutive windows only helps up to a certain point. The most efficient way to achieve a better demodulation is to do as indicated by Fig. 3.29 and to increase the flow velocity or incident angle θ.

System Amplitude Response

To determine the lowest detectable acoustic power by the system we measure a series of increasing acoustic powers using the laser and the reference microphone. Figure 3.30 compares the measurement of increasing acoustic pressures at $f_a = 1.5$ kHz.

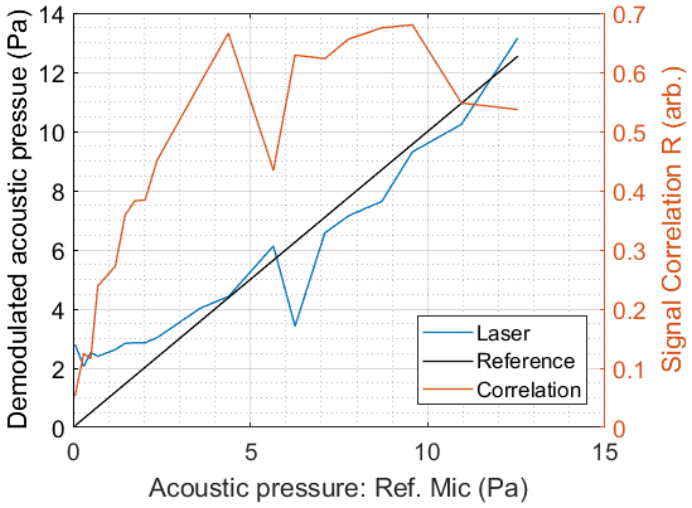

Figure 3.30: Minimal detected acoustic pressure 1.5 kHz. Marked in Black is the acoustic pressure from the reference microphone, in blue is the demodulated result and in red is the signal correlation R.

Marked in blue is the demodulated acoustic pressure, which is compared to the reference microphone, marked in black. The red curve denotes the correlation coefficient R between the reference microphone acquisition and the demodulated laser signal, for each acquisition. The R gives an indication of the quality of the demodulation.

With the increase of acoustic pressure observe an increase in the correlation coefficient. The higher acoustic pressures will have a greater effect on the particle velocity, effectively increasing the oscillation amplitude. This is in turn translated to a more marked Doppler

peak movement. When the Doppler oscillates with a great amplitude, the demodulation algorithm records it's movement with greater ease as opposed to a small movement.

The R in Fig. 3.32 is capped around $R = 0.7$. Figure 3.31 offers some insight into why the R is capped. The figure shows the demodulation of the 9.2 Pa zero to peak acoustic wave. We observe a decently demodulated signal marked in blue overlapping the reference microphone's acquisition marked in red.

The variation in amplitude contributes to lowering the R somewhat, but the real impact on R is observed towards the 10 ms mark. Here the demodulation algorithm has clearly failed, resulting in a lower R. Over the length of this particular signal this failure happens twice, resulting in the loss of a few periods. These losses contribute to lowering the R.

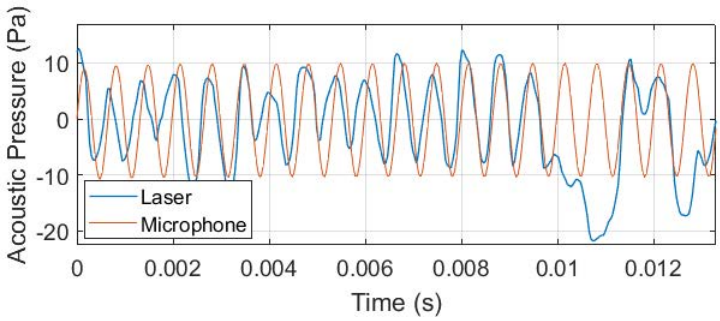

Figure 3.31: Demodulated time domain signal acquired of 9.2 Pa zero to peak acoustic wave.

On the other end of the spectrum, at the acoustic pressure of 2.03 Pa zero to peak (97.12 dB_{rms}), the demodulated signal indicates a pressure of 2.86 Pa zero to peak. The signal correlation factor $R = 0.38$ indicates that there is a great deal of noise, and that the acoustic signal and laser demodulation is not very well correlated. Below this pressure level, the R decreases rapidly. Furthermore, at the lower acoustic pressures the demodulation algorithm indicates acoustic pressures of around 2.5 Pa zero to peak regardless of the real pressure variation which is measured by the microphone.

Figure 3.32 shows the demodulated laser signal at 2.03 Pa zero to peak, superposed on the signal recorded by the reference microphone. Despite the high noise, and the 0.83 Pa zero to peak error between the microphone and the laser, we can visually resolve several periods of the acoustic signal. Furthermore, the acquisition of several periods averages out the demodulation errors. From the data presented in Fig. 3.30 we consider that the lowest detectable acoustic amplitude is around 2 Pa zero to peak in this configuration.

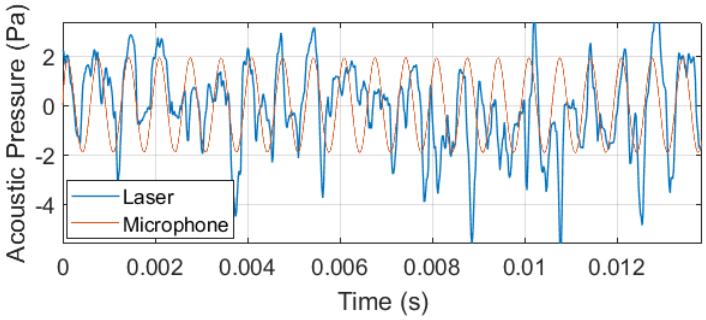

Figure 3.32: Demodulated time domain signal from lowest detectable acoustic amplitude of 2.03 Pa zero to peak.

3.6.2 Long Range Acoustic Acquisition

The principal interest of an acoustic LIDAR is to record acoustic waves at a distance. In the previous section we studied a system recording acoustic waves at a distance of less than a meter. The next step is to increase the distance between the laser and the target. Although the specifics of the experiments are described in detail in Section 3.6.2.2, the increased range comes with it's own set of challenges that we will briefly describe here.

The feedback parameter C which is discussed in Section 1.5.2 is impacted by the external cavity length, which is the distance from the laser to the target. A very high C can lead to instabilities in the laser thus perturbing the acquisition.

In this section we will discuss ways to impact the feedback parameter to our advantage, and we will demonstrate the system's ability to acquire sound by measuring the entrainment of particles in acoustic waves.

3.6.2.1 Target Reflectivity and Laser stability

The feedback parameter C is impacted by the distance between the laser and the target flow. When acquiring sound waves at a great distance, a high C-factor is one of the main perturbing elements.

In this section we study the impact of reflected optical power on the signal. We attempt to find an optimal configuration where the signal quality in terms of signal to noise amplitude is maximized for a configuration where the target is at a great distance from the laser.

Experiment

A DFB laser diode (LM720J11S) with wavelength $\lambda = 1310$ nm is mounted in an Arroyo Instruments laser mount that contains a temperature control driven by a ThorLabs TED 200C. A set of custom lenses and an optics rig designed by Epsiline (`www.epsiline.com`) is used to focus the laser beam at a distance 11.5 m. Five ThorLabs Protected Silver Mirrors are used to reflect the laser back and forth over the optical table to attain the 11.5 m of distance necessary. The width of the beam requires two $\varnothing = 76.2$ mm PF30-03-P01 mirrors as the first two reflectors. Then, two $\varnothing = 50.8$ mm PF20-03-P01 are used before a final $\varnothing = 12.7$ mm PF05-03-P01 mirror mounted in a ThorLabs KC1 Kinematic mount that aims the laser beam at the point of measure. An adjustable Thorlabs NDC-50S-1M neutral density is mounted between the last mirror and the point of measure. A schema of the experimental setup is displayed in Fig. 3.33.

The laser points on a rotating target of controlled velocity. The target is a metallic disk with a polished surface, offering an homogeneous rugosity. The interferometric signal containing the Doppler frequency related to the rotation velocity is acquired by Tektronix DPO 4034 Oscilloscope. A Schema of the experiment is presented in Fig. 3.33. Photos of the experiment are shown in Figures 3.34 and 3.35

Before hitting the target the beam passes through a CCM1-BD015/M beam splitter, sending 50% of the beam into a Thorlabs ND5 optical attenuator that absorbs the optical power. The rest of the beam goes straight through the beam splitter and hits the rotating target.

Upon reflection from the target, 50% of the returning photons (in the optical axis) will pass straight through the beam splitter. The other 50% are deflected onto a ThorLabs S122C photodiode connected to a ThorLabs PM100D, measuring the optical power.

The beam passes through a linear NDL-10C-2 attenuator of optical density (OD) 0-2 whose function is to decrease the target reflectivity. The attenuator is mounted on a Zaber linear translation stage that moves a distance of 100 μm between signal acquisitions. A total of 200 acquisitions are made.

For each value of attenuation the Signal to Noise Amplitude of the Doppler frequency in the SM-signal is estimated, and the returning optical power is measured.

To assure that the same zone of the spinning disk is scanned at each acquisition, a thin reflective band is fixed on the side of the rotating disk. Another laser is aimed at the side of the rotating disk, and each time the band passes through the laser beam a signal burst is produced. The oscilloscope triggers on the burst.

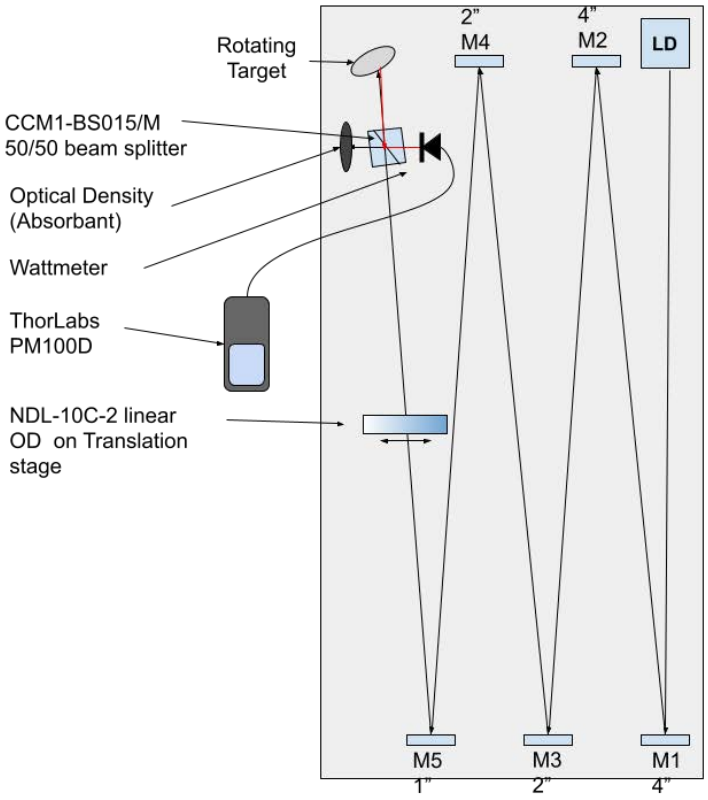

Figure 3.33: Schema of experimental setup

Results and Discussion

The SM-signals generated by the spinning disk shows that the signal to noise ratio (SNR) of the Doppler peak is impacted by the external reflectivity. Once acquired, the SM-signals were processed to recover the Doppler frequency. Welch's algorithm was applied to estimate the power density (PSD), and the SNR was estimated.

The noise floor in the PSD was estimated as shown in Fig. 3.36, by considering the amplitudes of the points preceding and succeeding the Doppler lobe. A line is drawn through the points 10 preceding the Doppler lobe, and it is prolonged through base of the Doppler lobe before it intersects the 10 points succeeding the lobe. The SNR is estimated as the amplitude difference between the peak of the lobe and the corresponding amplitude of the line drawn through the base of the lobe. Figure 3.36 shows graphically how the SNR is estimated. The blue line is the power density estimate, the red line is the Doppler lobe, the two green lines are the 10 points preceding and succeeding the Doppler lobe and

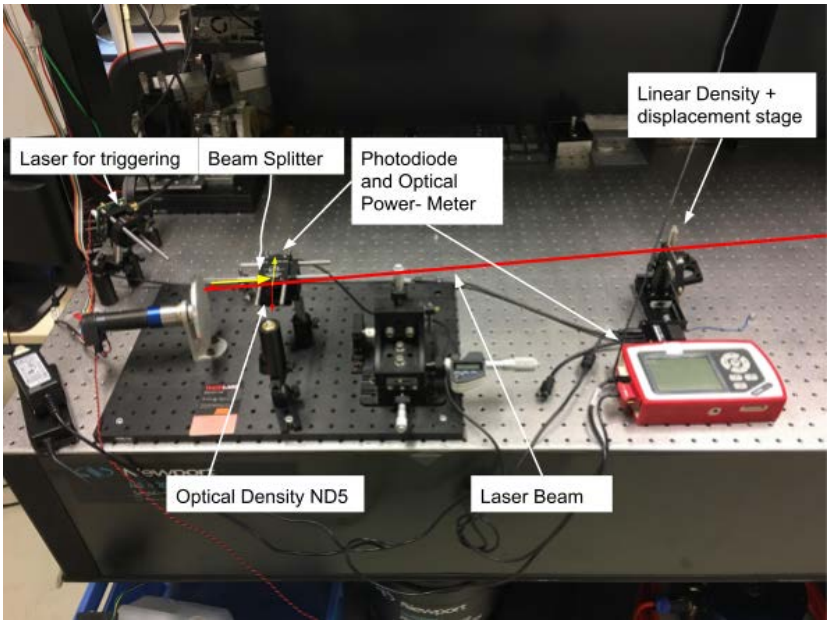

Figure 3.34: Photo of experimental setup

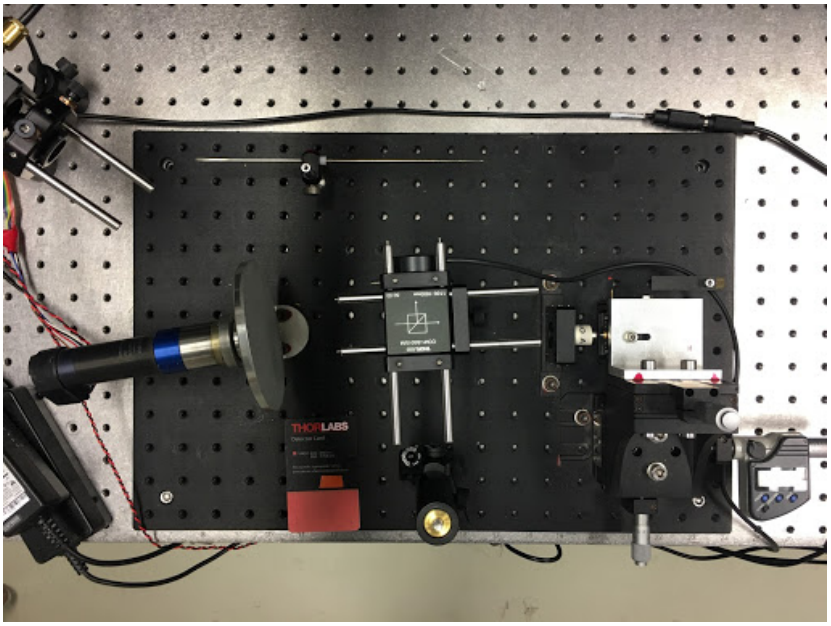

Figure 3.35: Close up of experimental setup

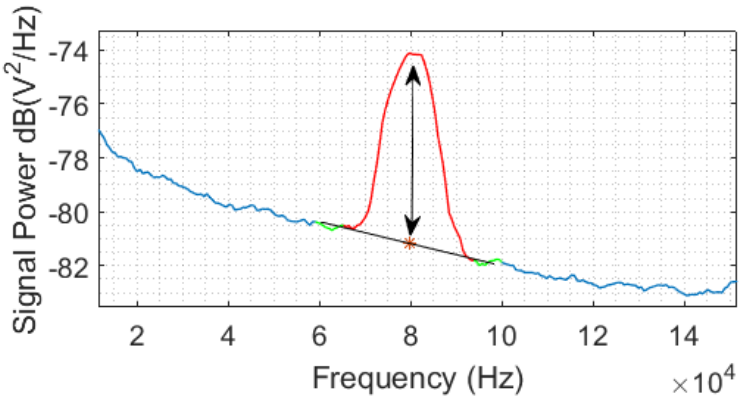

Figure 3.36: Graphic description of SNR estimation.

the black line is the estimated noise floor under the Doppler lobe. The red star marks the amplitude of the noise level at the Doppler peak. The SNR is estimated as the the difference in power between the peak and the noise, shown by a double arrow.

The experiment result is shown in Fig. 3.37. The top plot displays the SNR as the optical transmission increases. The bottom plot shows the amplitude of the noise floor and the amplitude of the Doppler peak.

The Thorlabs NDC-50S-1M neutral density was set to 0.1, and the NDL-10C-2 optical attenuation was used to gradually change the transmission. We observe that both the Doppler peak and the noise floor amplitude change with the increasing transmission. However, we observe that the two increase at a different rate. This indicates that an optimal target reflectivity exists where the Doppler peak is maximized with respect to the noise.

In this experiment an attenuation of 0.36 from the linear attenuator and 0.1 from the circular attenuator resulted in the highest SNR. The total attenuation value of $\mathrm{OD_{tot}} = 0.46$ indicates that the incident beam is reduced to around 34% of it's initial value after passing through the attenuators.

$$T = 10^{-\mathrm{OD_{tot}}} = 0.342 \tag{3.33}$$

In turn, the beam splitter spits the light 50/50 decreasing the transmission to half before the beam hits the rotating target. The returning flow of photons is split again when re-entering the beam splitter, which divides the transmission in half again.

The small amount of light that returned from the rotating target and back to the S122C photodiode connected to the wattmeter, was too low to be isolated from perturbing elements such as temperature variations and light pollution. Thus the reflected power could not be measured in a robust manner. The S122C photodiode's detection range is

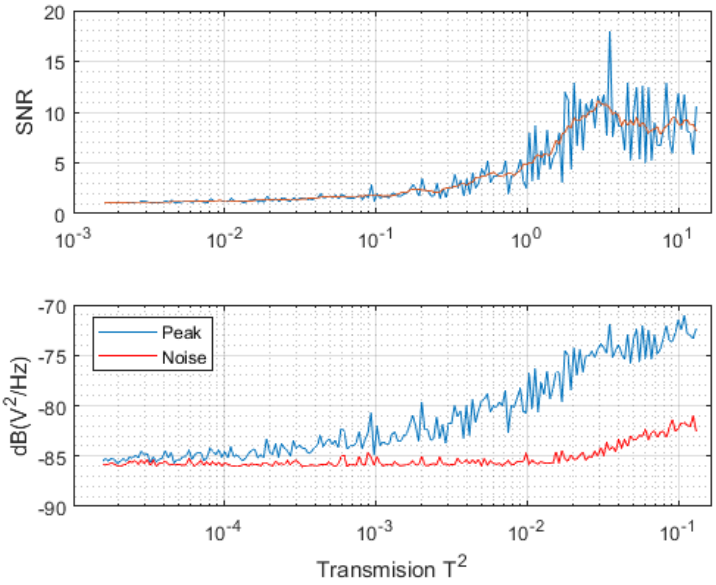

Figure 3.37: Experimental results. Top plot: SNR estimation for different transmission rates (T^2). Bottom plot: Doppler peak and noise floor.

50 nW - 40 mW. This could also indicates that the retro-diffused power was below 50 nW.

Since the part of the photons that travel back to the laser have to the pass through the same attenuators one more time, the transmission is calculated as T^2. The double pass through the beam splitter reduces the transmission by 75%. At the max SNR, this effectively leaves us with a transmission of 3% for the returning light that makes it back to the laser, as shown in Fig. 3.37.

This experiment shows that a high reflection coefficient is not ideal when the point of measure is far away from the laser source. A high coefficient increases the noise in the laser signal, as shown in Fig. 3.37 for the highest transmissions. Thus, attention has to be given to the reflectivity when acquiring acoustic waves from aerosol. The density of the aerosol flow and number of particles, will play a role in terms of target reflectivity.

3.6.2.2 Long Range Acoustic Acquisition: Experimental Setup

The experimental setup for long range acoustic acquisitions is similar to the experiment outlined in Section 3.6.1. Most components remain identical. The difference between the previous acoustic experiment and the following experiment is in the focusing lens, where we use Epsiline's optics for focusing the beam at a distance of 11.5 m.

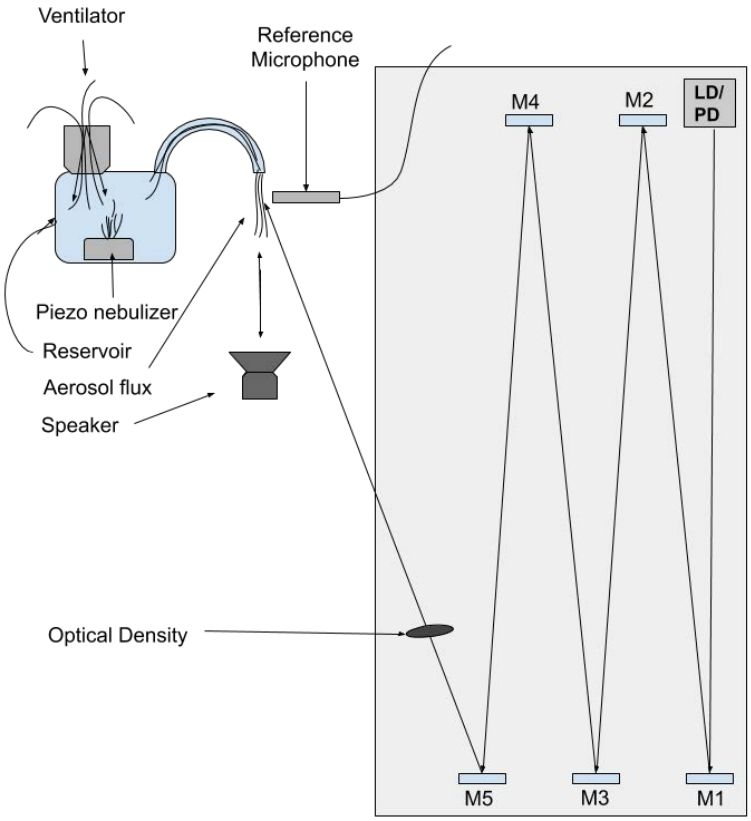

Figure 3.38: Schema of experimental Setup.

The point of measure (PV) remain unchanged from previous acoustic experiments, but the laser beam intersect the PV at an incident angle of $\theta = 85°$ to the flow traveling direction. Photons from the laser beam are then back scattered from the particles in the flow and travel back the way they came, having traveled a total of 23 m.

The laser is powered by an in-house low-noise power supply and the photo diode signal is recovered and amplified by an in-house amplification circuit. The electric signal from the amplification circuit is recorded by a Tektronix DPO 4034 Oscilloscope. The oscilloscope is controlled by Matlab.

The Visaton W 200 speaker is placed at 25 to 60 cm from the PV, at a $\theta_2 = 40°$ angle to the laser beam, facing the PV.

The acoustic input signal, the reference signal recorded by the microphone and the laser signal are all acquired simultaneously by the oscilloscope, and stored on the computer.

Figure 3.38 displays a schema of the experimental setup where the laser and it's optical rig is marked as PD/LD and the mirrors are marked as M1 thorough M5. Figure 3.39

displays two photos showing how the acoustic waves and laser beam intercept the probe volume.

As shown in Fig. 3.39a the speaker is positioned at 60 cm from the PV. The laser beam axis, marked in red, and the sound wave axis, marked in blue intersect at in the PV, where the incident angle is marked in black. The image shows a number of objects and obstacles surrounding the PV, such as walls and experimental equipment, contributing to the perturbation of the acoustic waves.

Figure 3.39b shows a close-up image of how the laser beam traverse the PV. The long neck of the particle guide reduces turbulence in the flow, thus rendering it close to laminar at the exit point where it intersects the laser beam.

3.6.2.3 Results and Discussion

Experiments to acquire an acoustic wave impinging on a particle flow at a distance of 11.5 m from the detector is performed. The acoustic wave is continuous and sinusoidal at a single frequency an amplitude. The acoustic frequency is $f_{\mathrm{a}} = 700$ Hz and the amplitude is 3.96 Pa zero to peak. The acoustic wave impinge on the flow and the acquisition lasts 4 ms. 28 acoustic periods are recorded and he signal length is set to $1 \cdot 10^6$ points.

The reference microphone and the laser is connected to the oscilloscope, so the acoustic signal is synchronized with the laser signal. The sampling frequency is set to $f_s = 25$ MHz to avoid aliasing around the Doppler frequency. The recorded signals are loaded into Matlab filtered numerically with a 3^{rd}-order Butterworth lowpass filter with cutoff frequency $f_c = 500$ kHz to avoid aliasing. The signal is then downsampled by a factor 5. The resulting output signals contain $2 \cdot 10^5$ samples.

The downsampled signal contains 3571 samples per half acoustic period, and the new sampling frequency is $f_s = 5$ MHz. Figure 3.40 shows the acoustic signal recorded by the reference microphone.

As discussed before, the laser acquisition system add a frequency / noise profile to the acquired SM-signal. This profile has to be flattened out using a set of weights. Figure 3.41 shows the laser signal and the underlying noise profile, and the weighted noise profile. The blue curve in Fig. 3.41a is the acquisition system's frequency profile, which impacts the Doppler lobe of the SM-signal plotted in red. Effectively, a weighted moment calculated on this profile will be biased to the left, towards the lower frequencies.

The weighted frequency spectrum is calculated by the logarithmic subtraction of the acquisition system's frequency profile from the SM-signal's frequency profile as before, using eq. 3.24. The result, shown in Fig. 3.41b is a flat spectrum where the Doppler lobe

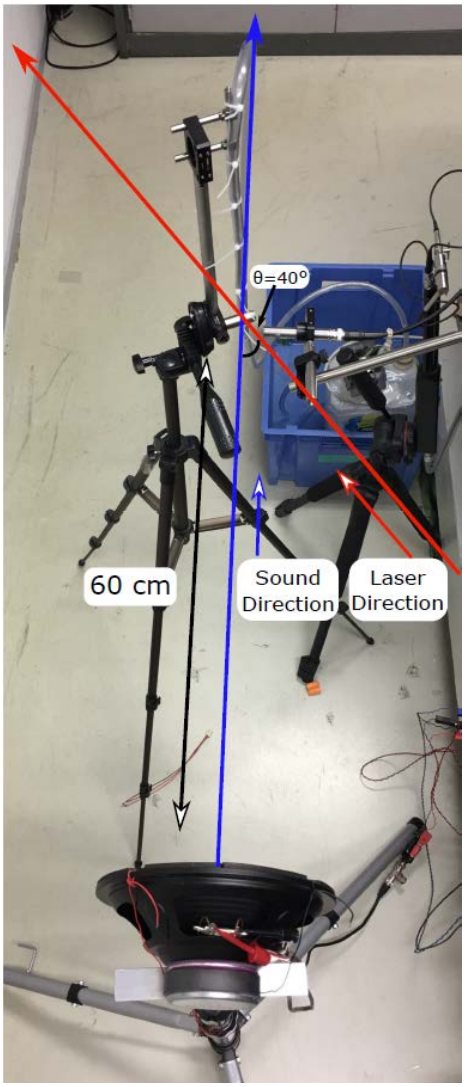

(a) Experiment seen from above

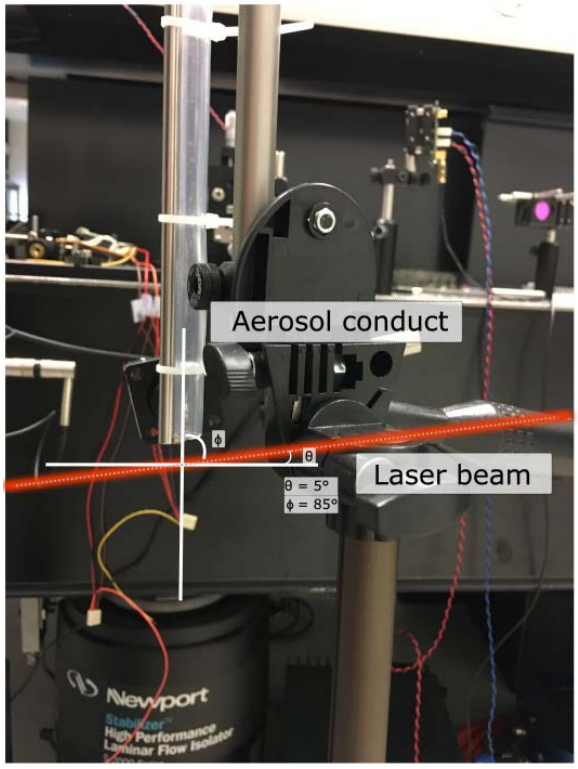

(b) Side View of Probe Volume

Figure 3.39: Photos of experiment from above, and of Probe Volume from the side with indicators of laser beam and sound directions.

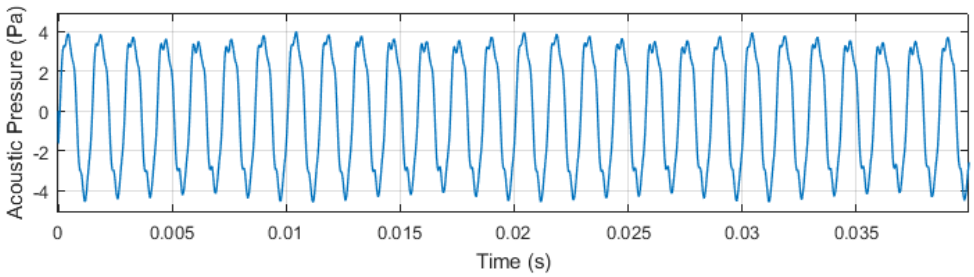

Figure 3.40: Acoustic signal recorded by the reference microphone. $f_a = 700$ Hz, amplitude 3.96 Pa zero to peak

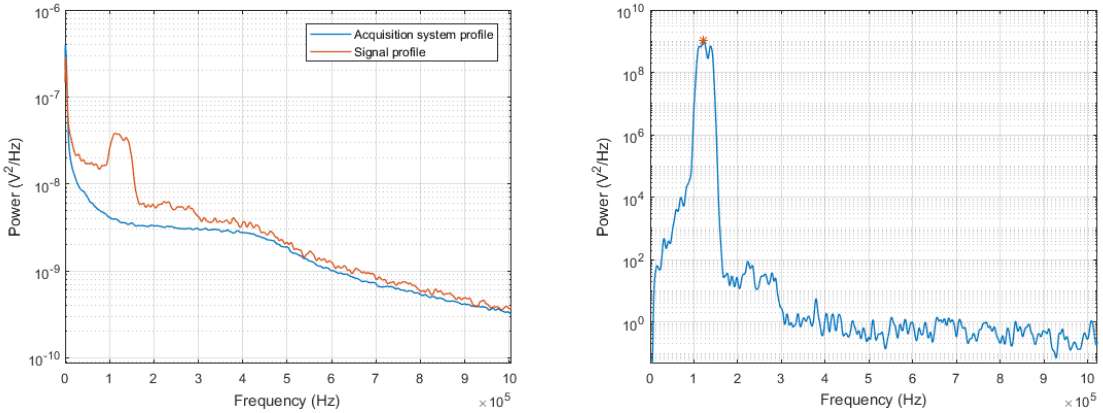

(a) Spectra of SM-signal and Acquisition chain

(b) Weighted spectrum

Figure 3.41: **Left:** Output spectra from SM-signal (red curve) compared to acquisition system (blue curve). **Right:** Weighted spectrum using profile from acquisition system.

is unperturbed by the low frequency response of the acquisition system.

The central Doppler frequency in this signal is marked by a red star in Fig. 3.41b and measures 124.5 kHz. As mentioned, there are ~ 3571 samples per half acoustic period. A window length of 1024 samples is chosen for the demodulation procedure, with 930 samples of overlap.

Figure 3.42 shows a step in the demodulation process where the weighted moment is calculated during a rise of pressure, as marked by the red curve in the top window. The curve is the acoustic pressure, recorded by the reference microphone. The blue jagged line in the same plot is the current section of the time domain SM-signal. The weighted spectrum $P_{W,i}$ is shown in the bottom plot. It is calculated from the signal above and weighted by the profile in Fig. 3.41a. The weighted moment in this frame is marked by a star in the bottom plot and is calculated to be $\bar{f}_i = 136.5$ kHz. The frequency windows are

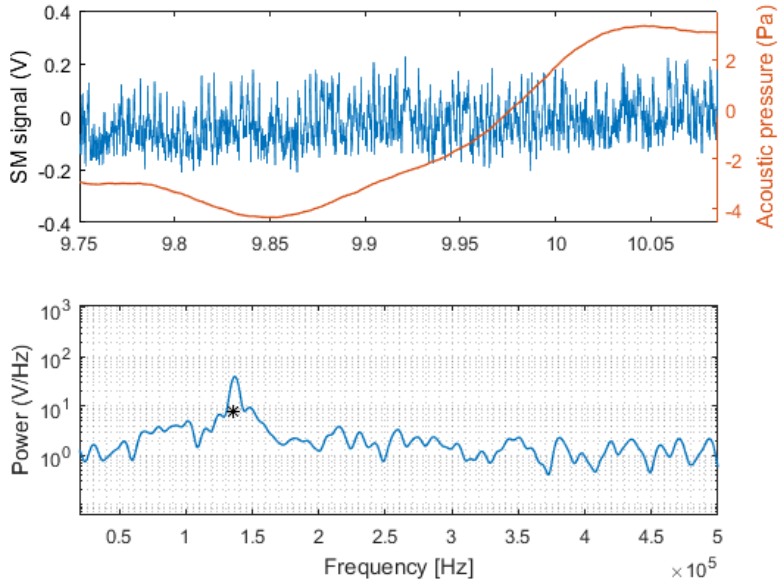

Figure 3.42: Demodulation step. **Top:** Time domain SM-signal in blue and acoustic pressure in red. **Bottom:** Weighted power spectrum in blue and weighted moment marked as a star.

updated, making $f_{1,i} = 95.55$ kHz and $f_{2,i} = 177.45$ kHz for the next frame, corresponding to $\bar{f}_i \pm 30\%$.

Figure 3.43 displays the demodulated result. There is clear periodicity in in the signal, but some variance in the peak to peak amplitude is observed.

As before a correlation between the acoustic reference signal and the demodulated signal is made. The two signals are displayed in Fig. 3.44 where the demodulated laser signal has been converted to pressure. The correlation coefficient $R = 0.871$ indicate a very good correlation between the two.

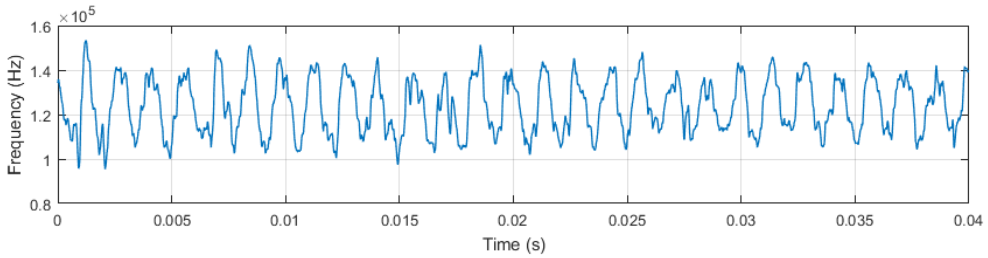

Figure 3.43: Demodulated SM-signal using weighted moments

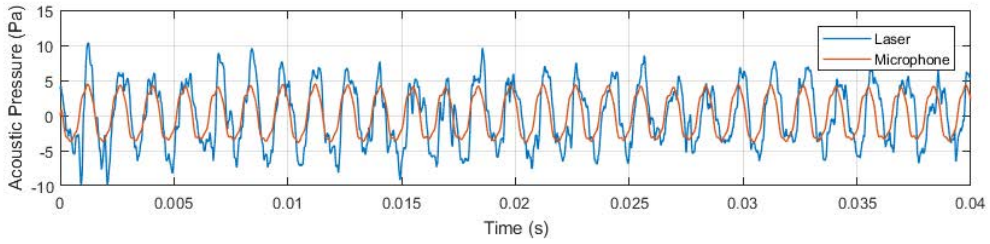

Figure 3.44: Demodulated SM-signal using weighted moments, converted to acoustic pressure

Despite the high correlation we observe some difference between amplitude of the signal, marked in blue, and the acoustic signal recorded by the reference microphone, marked in red. The average amplitude for the demodulated signal is $p_{\text{avg}} = 5.34$ Pa zero to peak. The amplitude measured by the reference microphone is 3.96 Pa zero to peak.

The measured acoustic amplitude depends on the incident angle between the laser and the acoustic wave's traveling direction. The angle was estimated to $\theta_2 = 40°$ using a protractor. However, lacking tools to make a precise measurement, an uncertainty of around 2° is added to this angle.

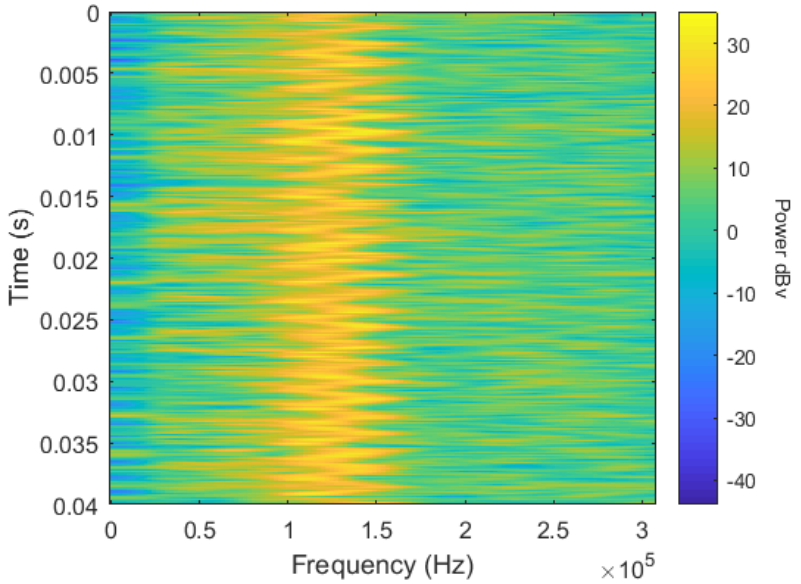

Figure 3.45: Spectrogram of SM-signal with 700 Hz acoustic oscillation

Looking at the spectrogram in Fig. 3.45 we see a clear oscillation between $f_1 \sim 87.16$ kHz and $f_2 \sim 162$ kHz. We can use this observation to force the frequency limits to stay unchanged throughout the demodulation. The result is shown in Fig. 3.46 where we

observe that the zero to peak amplitude is reduced to $p_{\text{avg}} = 4.17$ Pa.

This result is closer to the real acoustic amplitude. However, fixing f_1 and f_2 renders the demodulation less robust if a change in mean particle velocity is present. If a gradual acceleration or deceleration throughout the acquisition were present, the amplitude of the oscillation would risk falling outside of the limit imposed by f_1 and f_2. Furthermore, fixing the frequencies demands an a priori knowledge of where to limit these frequencies.

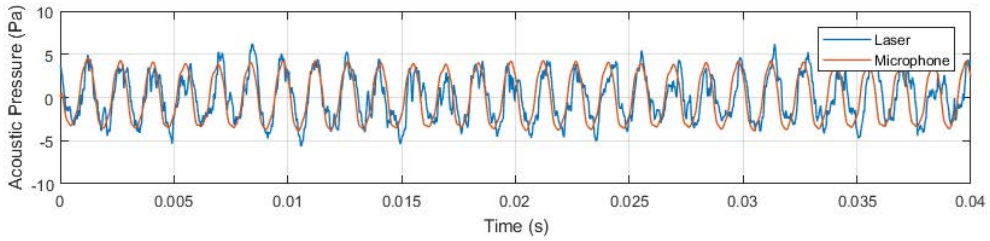

Figure 3.46: Demodulation of SM-signal with 700 Hz acoustic oscillation, using a static frequency window

In a final experiment to demonstrate how instabilities are easily manifested in long distance acquisitions, we compare two frequency spectra. The spectra are of signals recorded one right after the other. This acquisition does not contain acoustic waves as we're only interested in the shape of the spectra and the Doppler peaks. The adjustable Thorlabs NDC-50S-1M neutral density is set to 0.2, and the flow density is set to max.

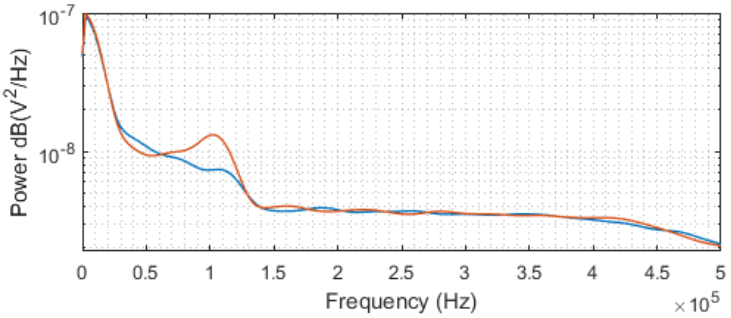

Figure 3.47: Frequency spectrum of two consecutive signals, acquired seconds apart.

Figure 3.47 compares the frequency spectra of two consecutive acquisitions recorded seconds apart. One of the spectra has a clear Doppler peak. The presence of such a clear peak often indicates that it is possible to demodulate the signal using our Demodulation algorithms. The lack of a clear peak in the blue line makes it challenging to recover the amplitude of an acoustic wave.

These experiments have all been performed using the experimental tools at hand. The flow density has an impact on the reflectivity of the target. However, we lack the tools to

properly quantify the number of particles produced. The reflected power from the flow also remain unresolved. The great external cavity distance increases the C factor. To regulate this we need to quantify and regulate the target reflectivity.

The ambient temperature may play a role in the behavior of the system under current settings. As the temperature changes, there may be dilations and contractions in the optics rig, made of aluminum, holding the lenses. This may in turn displace the focal point, entraining a change in the reflectivity from the flow.

Despite the obstacles to overcome when measuring sound at a great distance form the laser, we have demonstrated in this section that sound measurements are possible at 11.5 m from the source.

3.7 Chapter Synthesis

This chapter has been dedicated to the acquisition of sound through measurements of particle entrainment by acoustic waves. First we've proposed an established model to estimate the particle velocity when entrained by acoustic waves. The model works for planar waves in the direction of propagation of the wave, and is ideally used in for far field propagating waves. It does not take into account concepts such as viscosity and particle weight, as we assume the particles are small enough to be completely entrained by the acoustic wave.

We proposed a modification to the classical OFI Power Equation to account for periodic changes in the particle flow. The acoustic model and the new OFI Power Equation were then incorporated into a simulator designed to generate an artificial particle flow with velocity oscillations due to an acoustic wave. The modulation parameter m is generated in a way that mimics that the laser beam is reflected from particles of different reflectivity and position in the flow. The output signal is closer to what one can expect to acquire during experiments.

A signal processing algorithm is developed to demodulate SM-signals and to recover the velocity variation of the particles. The algorithm calculates the average frequency on consecutive sections of the acquired laser signal using the weighted moments method. The simulation was used to evaluate the efficiency of our demodulation algorithm. The algorithm outputs the velocity of the aerosol flow, and most notably it's modulation in time. The demodulated velocity data was then translated to acoustic pressure using the acoustic model.

Through an extensive set of experiments, we've put the concept to the test. We've

proven the efficiency of our algorithms for a given set of conditions and we've demonstrated that we can acquire acoustic waves using Optical Feedback Interferometry in a LIDAR configuration.

Through experiments we've identified several challenges to overcome. These challenges are related to the number of samples available per half acoustic period, and the number of Doppler periods. If these numbers are too low, we are unable to properly resolve the Doppler frequency and thus it's variations.

The experiments shows that demodulation algorithms are efficient at and gives results that are consistent with the intensity probe for frequencies between 50 to 3 kHz. The frequencies under 400 Hz deviate from the model, but the aerosol movement is resolvable by the algorithm. At frequencies higher than 1.5 kHz the number of Doppler periods available per half acoustic period on which to calculate the frequency spectra becomes limited.

The feedback parameter C is affected by parameters such as target reflectivity and external cavity round-trip time. Signals acquired at a distance of 11.5 m are perturbed by the strongly increased C-factor. By controlling the target reflectivity using optical attenuators, we have shown that there exist an optimal regime where the signal to noise ratio in the acquired laser signal can be maximized.

Experiments to acquire acoustic waves at 11.5 m were presented and the demodulation algorithms were successfully used to acquire an acoustic wave from the aerosol flow. However, due to the instability of the laser signal, that is proven to be due to a large coupling coefficient, acquisition is challenging at such a great distance.

An experiment demonstrating the sudden changes in feedback regime was performed where two consecutive signals are recorded from the aerosol flow. The two signals were taken seconds apart with the same experimental and environmental conditions in place. The Doppler peak of one of the signals is not present, whereas the other signal exhibit a clear Doppler peak.

Temperature oscillations make the optics rig dilate and contract. This pushes the focal point back and forth, which can pose problems for repeatability in a lab. The flow was placed in a fixed position, and thus temperature oscillations may have had an impact on the SM-signal quality. However, the temperature oscillations should have an impact on signals taken minutes or even hours apart. Not on signals acquires seconds apart. This leads us to think that the C-factor is the major culprit when the Doppler lobe disappears in a signal.

Throughout this chapter we've demonstrated the potential of the acoustic LIDAR, and we've shown that we can acquire acoustic waves at a distance of up to 11.5 m. In doing so,

we've revealed several challenges. By continuously improving the demodulation algorithms and ameliorating the experimental setup, these challenges will be overcome. The acoustic LIDAR by Optical Feedback Interferometry is the first of it's kind and is the cumulation of research over a broad range of scientific fields. Further research on signal processing, laser physics, acoustics and fluid dynamics will further advance this sensing scheme.

Conclusion and Perspectives

General Conclusion

In this PhD thesis we have discussed optical methods for recording acoustic waves. In Chapter 1, several audio detection systems were covered, and the advantages and inconveniences of mechanical and diaphragm based microphones were compared to diaphragm-free microphones and optical systems. Optical Feedback Interferometry, being a relatively low cost and easy to implement sensing scheme was proposed as an acoustic detector. The basic theory and operating principles of the OFI-sensing scheme was covered in Chapter 1 and we proposed two distinct OFI configurations for acoustic sensing.

The first configuration was used to measure the acousto-optic effect. When an acoustic wave travels through air, the refractive index of air is altered due to the change of pressure inside the wave. The change of refractive index is sensed by the laser as a change in optical path. The optical path variation induced by the acoustic pressure is smaller than a half laser wavelength, hence the laser signal does not contain any interferometric fringes.

The second configuration that was proposed, was used to measure acoustic waves at a distance from the laser. The OFI interferometer was set up in a LIDAR configuration to measure acoustic waves that impinge on a flow of particles. When an acoustic wave impinge on a particle or flow of particles in air, the particles are displaced. The particle displacement can be measured by the OFI interferometer.

In Chapter 2 we adress the acousto-optic sensing method and we showed that the shape of the interferometric fringe has an impact on signal amplitude in sub-$\lambda/2$ sensing. We demonstrated through experiments and simulations that the slope of the fringe is linearly coupled with the phase to power amplitude conversion. A steep slope will increase the amplitude of the detected signal. This research has an impact on acoustic measurements, where the optical path variation is smaller than $\lambda/2$.

We demonstrated that the algorithm developed by Kliese et al [68], for SM-signal generation accurately simulates sub-$\lambda/2$ optical path variations. Using this algorithm we were able to displace the operating point on the fringe. The different positions showed different amplitude responses to the same stimulus. These findings were confirmed by experiments. They reveal the difficulty that this method faces for measuring the sound pressure level quantitatively and with a sufficient accuracy.

In one experiment the operating point was positioned in between two fringes, in the fringe jump. This resulted in a strong increase in phase to power conversion gain. The

experiment indicate that clever positioning of the operating point can be beneficial to OFI vibrometers measuring sub-$\lambda/2$ optical path variations.

An experiment was constructed to measure the lowest detectable acoustic pressure through measurements of the refractive index of air. The smallest detectable acoustic level was measured to be 35 dB_{rms}. However, we discovered that the detector's sensitivity is frequency depended in the current experimental setup. This indicates that the we've reached the limits of the performances of the current experiment.

An attempt to quantify the acousto-optic effect was also made in Chapter 2. The model was put to the test using the experiment outlined above. Validating the model became challenging as the experimental setup was pushed to it's limits and we discovered that further improvements are needed to isolate the system from outside perturbations.

Chapter 3 was dedicated to measuring acoustic waves using the OFI detector in a LIDAR configuration. In this chapter applied a model that converts particle velocity into pressure. The model considers planar waves moving in a single direction and that an aerosol is small enough to be completely entrained by the acoustic wave. We validated the model using an intensity probe which measures the velocity of the movement of air inside an acoustic wave.

A demodulation algorithm was proposed to recover the acoustic data from the measured particle movement. The algorithm uses spectral analysis' of the OFI signals to compute the weighted moments to estimate the instantaneous Doppler frequency. The Doppler frequency variation is the converted to pressure using the acoustic model.

An experiment was proposed to demonstrate the detector concept. Acoustic waves impinging on a flow of particles were measured by the laser at a distance of several tens of centimeters. Using this configuration we studied the response of the system to various acoustic wave at different frequencies. We showed that the laser coherently measures the particle movement at acoustic frequencies from 50 Hz to 3 kHz. At frequencies lower than 400 Hz the particle flow's movement is much greater than the model predicts, but coherent with regards to the velocity measurements performed with an intensity probe.

At higher frequencies, the system demonstrates limitations induced by the too small difference between the Doppler frequency induced by the flow and the acoustic frequency.

For long distance acquisitions, we show that the high feedback parameter C can destabilize the laser. Using a variable optical density we show that there exists an optimal attenuation where the signal to noise ratio is maximized when measuring a rotating target at 11.5 m of distance.

Finally, acoustic waves were recorded at a distance of 11.5 m using optics designed

specifically for this application. The movement of a particle flow was recorded converted to acoustic pressure. Through this experiment we have demonstrated that sound acquisition is possible at great distances. Due to instabilities in the laser at these distances, we showed that we have less control over the repeatability of this experiment. The elevated feedback parameter C is a likely culprit laser instabilities.

Through these experiments we have successfully validated an experimental demonstrator to validate the concept of non-intrusive acoustic acquisition at a distance.

Future Perspectives

Both acoustic detection systems in this PhD are subjects to improvement and further development. Both systems are destined for different applications, but their respective potentials offer great prospects. Here we offer some future perspectives on the two acquisition configurations.

The acousto-optic effect was proven to be challenging to characterize. Improvements to this experiment should include better acoustic isolation of the laser beam. The reference microphone measures the acoustic waves only in one position in space. The laser beam integrates the change in refractive index over the length of the entire detection volume. As such, a characterization of the propagating acoustic field is needed. This would provide us with a better understanding of other perturbing factors and discrepancies between the acoustic measurements and the model.

The accelerometers measuring the relative displacement between the laser and the reflective wafer did not record much vibration. However, we must recognize that if the wafer itself were to vibrate, the accelerometer positioned on the piezo casing may be insensible to those vibrations. Using a rigid waveguide made of metal, and an impedance adapter made of a similar heavy material, may reduce acoustic leakage. These improvements may reduce potential vibrations of the reflector.

The length of the optical path has an impact on the detectors sensitivity. One way to detect even lower acoustic pressures is to increase the external cavity length. This may be achieved by creating multiple reflections back and forth through the detection volume. This way the laser beam would traverse the measurement zone multiple times.

An OFI-microphone could be conceived where the laser beam enters a reflective ring, and is bounced back and forth inside multiple times before reinjection. Figure 3.48 shows a conceptual schematic of how this technology could be incorporated.

The laser beam would travel through an acoustic wave inside the reflector ring several

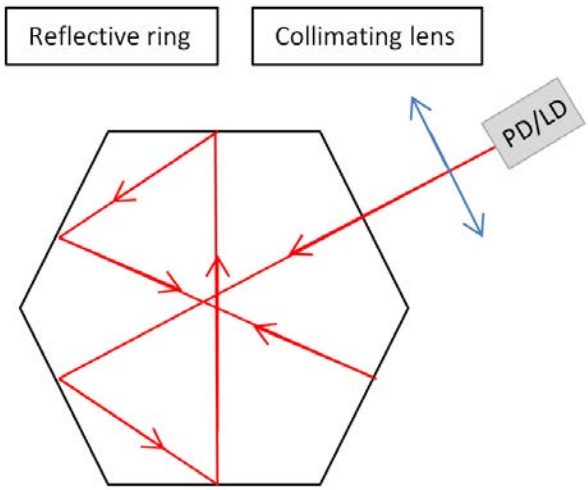

Figure 3.48: Illustration of concept to increase external cavity length in order to increase detection of changes in the refractive index of air.

times before being reinjected. A small ring would result in an planar acoustic wave inside the detection cavity.

The acoustic LIDAR by Optical Feedback Interferometry was demonstrated in this PhD. At it's current stage of development there are challenges to resolve in terms of system stability, signal demodulation and acoustic modeling.

The future system will be used to measure acoustic waves based on single particle detections in air. The experiment may be rigged in a way that allows for single or low-concentration seeding of particles into the PV.

The challenges related to a high C-factor must thus be evaluated with this in mind. As of today we measure the movement of a flow of particles. The reinjection potential for a flow of water droplets is higher than for a single particle.

The system has not been tested in open space in free air such as on a rooftop. Acosutic reflections would not be a problem in such an environment. but non-stable wind conditions will induce a dynamic flow velocity which is challenging for the processing algorithm we have proposed.

The acquisition system of a future system must be designed with high-velocity detection in mind. The future acoustic LIDAR will exert no control over the particle incident angle or velocity. Thus the system needs to be adapted for such situations.

ACOEM uses artificial intelligence and neural networks in their products while this topic is a long lasting expertise at the LAAS-CNRS and growing fast in the OASIS re-

search group. The future OFI LIDAR will strongly take advantage of this know-how. The processing algorithm may be coupled with DSP in a SOC configuration, to use AI algorithms to better recover the acoustic profile from the Doppler signal data.

One envisioned application of this system is to detect acoustic signatures in difficult to reach areas. The system could be placed on a rotating platform or on a vehicle. From that platform the laser is pointed into the zone of interest. Gas leaks in refineries could be detected by quickly moving the detector from point to point, and by placing the laser focal point close to critical structures where such leaks may occur.

Site such as airports where noise is generated by aircraft can benefit from this application. Sound signatures in the proximity of an aircraft's engine can be recorded. Since the sensor is non-contact, it can be safely placed away from an aircraft's engine, while recording the sound generated.

The versatility of the OFI sensing scheme has been proven in this PhD thesis. In the domain of acoustic detection, we have shown two configurations capable of recoding sound waves. Using the acousto-optic effect we are able to directly measure the change in refractive index of air due to the passage of an acoustic wave. The acoustic LIDAR measures the movement of particles entrained by an acoustic wave, at 11.5 meters from the laser source. Both of these applications are under development and will with further research become viable acoustic detectors available to the industry.

Appendix A

Extract Particle Velocity from Intensity Probe Measurement

To record the particle velocity using the intensity probe and the software developed by ACOEM, a few steps have to be taken. For given velocity acquisition the dBFA software acquires 32 recordings, per acquisition and on each acquisition the system calculates the autospectrum for each microphone $S_{1,1}$ and $S_{2,2}$, and the cross-spectrum $G_{1\to2}$. These parameters can be used to calculate the average particle velocity.

The velocity V of the molecular medium in a plane pressure wave moving along the z axis can be expressed in the frequency domain as

$$V(\omega, z) = -\frac{1}{\rho}\frac{1}{2\pi j f_{\mathrm{a}}}\frac{\partial P(\omega, z)}{\partial z} \tag{A.1}$$

Where $\omega = 2\pi f_{\mathrm{a}}$, and f_{a} is the acoustic frequency. The uppercase P indicates that we operate in the frequency domain. Available in dBFA from the measurements we have

1. $S_{1,1} = P1(\omega, z) \times P1^*(\omega, z)$

2. $S_{2,2} = P2(\omega, z) \times P2^*(\omega, z)$

3. $G_{1\to2} = P1(\omega, z) \times P2^*(\omega, z)$

Where the pressures $P1$ and $P2$ are the pressures recorded by microphone 1 and 2. The pressure gradient over the microphone duplet in the axis of travel of the acoustic planar wave is expressed as

$$\frac{\partial P}{\partial z} = \frac{P2 - P1}{z_2 - z_1} \tag{A.2}$$

where z_1 and z_2 are the coordinates of the microphones. The spacing between them is

$d_{1,2} = 0.0105$ m. Considering the following equation,

$$\Big(P2(\omega,z) - P1(\omega,z)\Big) \times \Big(P2(\omega,z) - P1(\omega,z)^*\Big) = \tag{A.3}$$

$$P2(\omega,z) \times P2^*(\omega,z) + P1(\omega,z) \times P1^*(\omega,z) - 2\,\Re\Big(P1(\omega,z) \times P2^*(\omega,z)\Big) \tag{A.4}$$

we recognize the parameters $S_{1,1}$, $S_{2,2}$ and $G_{1\to2}$. The pressure difference in the frequency domain ΔP can thus be calculated as

$$\mid \Delta P(\omega,z) \mid^2 = S1,1 + S2,2 - 2 \times \Re(G_{1\to2}) \tag{A.5}$$

Using this we can now calculate the velocity for a given frequency f_a

$$\mid V(\omega,z) \mid = \mid \Delta P(\omega,z) \mid \frac{1}{d_{1,2}} \frac{1}{\rho} \frac{1}{\omega} = \frac{\sqrt{S_{1,1} + S_{2,2} - 2 \times \Re(P1 \times P2^*)}}{d_{1,2}/\rho/\omega} \tag{A.6}$$

where ρ is estimated to be $\rho = 1.23$.

Using eq. A.6 with the data from the acquisition software we can can calculate the particular velocity at the point of measure.

Bibliography

[1] K. Bertling, J. Perchoux, T. Taimre, R. Malkin, D. Robert, A. D. Rakić, and T. Bosch, "Imaging of acoustic fields using optical feedback interferometry," en, *Optics Express*, vol. 22, no. 24, p. 30 346, Dec. 2014 (cit. on pp. 2, 24, 35, 53, 54, 88).

[2] Édouard-Léon. S. de Martinville, *L'enregistrement du son, french patent 1bb31470 25.03.1857 phonautograph*, fr, Mar. 1857 (cit. on p. 6).

[3] P. F. U. Ortiz, "2D and 3D visualization of acoustic waves by optical feedback interferometry," en, *PhD Thesis: Micro and nanotechnologies/Microelectronics. Institut national polytechnique de Toulouse (INPT), 2019. English. tel-02442503*, p. 140, Jan. 2020 (cit. on pp. 7, 21, 24, 35, 53, 54, 80).

[4] K. Alexander and P. Alexander, *Small optical microphone/sensor*, Patent US 6,462,808 B2, 2002 (cit. on pp. 10, 11).

[5] J. Bob, *The optoacoustics 1140 fiber-optic microphone*, Licencing Creative Commons Wikipedia CC BY-SA 3.0, 2009 (cit. on p. 11).

[6] A. Glinsky, *Theremin: Ether Music and Espionage*. University of Illinois Press, p. 261. ISBN: 0-252-02582-2, Year 2000 (cit. on p. 11).

[7] G. Takács, J. Otčenáš, J. Vachálek, and B. Rohal'-Ilkiv, "Modal response-based technical countersurveillance measure against laser microphones," en, *Journal of Vibroengineering*, vol. 18, no. 5, pp. 3369–3382, Aug. 2016 (cit. on p. 11).

[8] R. Teysseyre, "Détection homdyne appliquée à la mesure de la vitesse du vent," PhD thesis, Institut National Polytechnique de Toulouse, 2013 (cit. on pp. 13, 37).

[9] M. Davis, "Hot wire anemometer response in a flow with acoustic disturbances," *Journal of Sound and Vibration*, vol. 56, no. 4, pp. 565 –570, 1978 (cit. on p. 13).

[10] G. Huelsz and F. López-Alquicira, "Hot-wire anemometry in acoustic waves," en, *Experiments in Fluids*, vol. 30, no. 3, pp. 283–285, Mar. 2001 (cit. on p. 13).

[11] D. M. Schwartz, *Particulate flow detection microphone*, en, Patent US 7,580,533 B2, 2005 (cit. on p. 13).

[12] J.-C. Valière, *Acoustic particle velocity measurements using lasers: priniciples signal processing and applications*, en. London ISTE: Hoboken, NJ, 2014 (cit. on pp. 14–17, 19, 20, 37).

[13] R. J. Adrian, "Particle-Imaging Techniques for Experimental Fluid Mechanics," en, vol. 23, p. 44, 1991 (cit. on p. 14).

[14] C. E. Willert and M Gharib, "Digital particle image velocimetry," en, *Experiments in Fluids*, p. 13, 1991 (cit. on p. 14).

[15] D. B. Hann and C. A. Greated, "Particle image velocimetry for the measurement of mean and acoustic particle velocities," en, *Measurement Science and Technology*, vol. 8, no. 6, pp. 656–660, Jun. 1997 (cit. on p. 14).

[16] D. B. Hann and C. A. Greated, "The measurement of flow velocity and acoustic particle velocity using particle-image velocimetry," en, *Measurement Science and Technology*, vol. 8, no. 12, pp. 1517–1522, Dec. 1997 (cit. on p. 14).

[17] M. Campbell, J. Cosgrove, C. Greated, S. Jack, and D. Rockliff, "Review of LDA and PIV applied to the measurement of sound and acoustic streaming," en, *Optics & Laser Technology*, vol. 32, no. 7-8, pp. 629–639, Oct. 2000 (cit. on pp. 15, 37).

[18] J. C. Valière, P. Herzog, V. Valeau, and G. Tournois, "Acoustic velocity measurements in the air by means of laser doppler velocimetry: Dynamic and frequency range limitations and signal processing improvements," *Journal of Sound and Vibration*, vol. 229, no. 3, pp. 607–626, Jan. 2000 (cit. on pp. 15, 16, 20, 37).

[19] T. L. Hoffmann, "Environmental implications of acoustic aerosol agglomeration," en, *Ultrasonics*, vol. 38, no. 1-8, pp. 353–357, Mar. 2000 (cit. on pp. 16, 37).

[20] S. Temkin and C.-M. Leung, "On the velocity of a rigid sphere in a sound wave," en, *Journal of Sound and Vibration*, vol. 49, no. 1, pp. 75–92, Nov. 1976 (cit. on p. 16).

[21] I. González, T. L. Hoffmann, and J. A. Gallego, "Precise measurement of entrainment in a standing-wave acoustic field between 20 and 3500 hz," en, *Journal of Aerosol Science*, vol. 31, no. 12, pp. 1461–1468, Dec. 2000 (cit. on pp. 16, 37).

[22] I. González, J. A. Gallego-Juárez, and E. Riera, "The influence of entrainment on acoustically induced interactions between aerosol particles—an experimental study," en, *Journal of Aerosol Science*, vol. 34, no. 12, pp. 1611–1631, Dec. 2003 (cit. on p. 16).

[23] J. Cleckler, S. Elghobashi, and F. Liu, "On the motion of inertial particles by sound waves," en, *Physics of Fluids*, vol. 24, no. 3, p. 033 301, Mar. 2012 (cit. on pp. 16, 77, 78).

[24] K. J. Taylor, "Absolute measurement of acoustic particle velocity," en, *The Journal of the Acoustical Society of America*, vol. 59, no. 3, pp. 691–694, Mar. 1976 (cit. on pp. 16, 20).

[25] K. J. Taylor, "Absolute calibration of microphones by a laser-Doppler technique," en, *The Journal of the Acoustical Society of America*, vol. 70, no. 4, pp. 939–945, Oct. 1981 (cit. on p. 16).

[26] M. Davis and K. Hews-Taylor, "Laser-doppler measurement of complex acoustic impedance," en, *Journal of Sound and Vibration*, vol. 107, no. 3, pp. 451–470, Jun. 1986 (cit. on p. 16).

[27] J. F. Vignola, Y. H. Berthelot, and J. Jarzynski, "Laser detection of sound," en, *The Journal of the Acoustical Society of America*, vol. 90, no. 3, pp. 1275–1286, Sep. 1991 (cit. on p. 16).

[28] D. M. Eckmann and J. B. Grotberg, "Experiments on transition to turbulence in oscillatory pipe flow," en, *Journal of Fluid Mechanics*, vol. 222, no. -1, p. 329, Jan. 1991 (cit. on p. 16).

[29] V. Valeau, J. Valiere, P. Herzog, L. Simon, and C. Depollier, "Instantaneous frequency tracking of a sine wave phase modulation signal," en, in *Proceedings of Third International Symposium on Time-Frequency and Time-Scale Analysis (TFTS-96)*, Paris, France: IEEE, 1996, pp. 501–504 (cit. on p. 16).

[30] A. L. Duff, "Contribution à l'estimation paramétrique de signaux à variation sinusoïdale de la fréquence instantanée et à amplitude variable: Application à l'anémométrie laser à effet Doppler pour l'acoustique," p. 172, (cit. on p. 17).

[31] S. Donati, *Electro-optical instrumentation: sensing and measuring with lasers*. Upper Saddle River, NJ: Prentice Hall, 2004 (cit. on p. 18).

[32] A. Le Duff, G. Plantier, J. C. Valière, and B. Gazengel, "Acoustic velocity measurement by means of Laser Doppler Velocimetry: Development of an Extended Kalman Filter and validation in free-field measurement," en, *Mechanical Systems and Signal Processing*, vol. 70-71, pp. 832–852, Mar. 2016 (cit. on p. 20).

[33] C. Scruby and L. Drain, *Laser Ultrasonics Techniques and Applications*. Taylor & Francis, 1990 (cit. on p. 20).

[34] T. Davies, "Schlieren photography—short bibliography and review," en, *Optics & Laser Technology*, vol. 13, no. 1, pp. 37–42, Feb. 1981 (cit. on p. 20).

[35] X. Jia, G. Quentin, and M. Lassoued, "Optical heterodyne detection of pulsed ultrasonic pressures," en, *IEEE Transactions on Ultrasonics, Ferroelectrics and Frequency Control*, vol. 40, no. 1, pp. 67–69, Jan. 1993 (cit. on p. 20).

[36] J.-P. Remenieras, O. Matar, S. Calle, and F. Patat, "Acoustic pressure measurement by acousto-optic tomography," en, in *2001 IEEE Ultrasonics Symposium. Proceedings. An International Symposium (Cat. No.01CH37263)*, vol. 1, Atlanta, GA, USA: IEEE, 2001, pp. 505–508 (cit. on p. 20).

[37] L. Zipser, H. Franke, E. Olsson, N.-E. Molin, and M. Sjödahl, "Reconstructing two-dimensional acoustic object fields by use of digital phase conjugation of scanning laser vibrometry recordings," en, *Applied Optics*, vol. 42, no. 29, p. 5831, Oct. 2003 (cit. on p. 21).

[38] L. Zipser and H. Franke, "5E-4 Refracto-Vibrometry for Visualizing Ultrasound in Gases, Fluids and Condensed Matter," en, in *2007 IEEE Ultrasonics Symposium Proceedings*, New York, NY: IEEE, Oct. 2007, pp. 395–398 (cit. on p. 21).

[39] L. Zipser, H.-D. Seelig, and H. Franke, "Refracto-vibrometry for visualizing ultrasound in small-sized channels, cavities and objects," en, in *2009 IEEE International Ultrasonics Symposium*, Rome, Italy: IEEE, Sep. 2009, pp. 2588–2591 (cit. on pp. 21–23).

[40] R. Malkin, T. Todd, and D. Robert, "A simple method for quantitative imaging of 2D acoustic fields using refracto-vibrometry," en, *Journal of Sound and Vibration*, vol. 333, no. 19, pp. 4473–4482, Sep. 2014 (cit. on pp. 21, 23).

[41] F. Mbailassem, Q. Leclère, E. Redon, and E. Gourdon, "Experimental analysis of acoustical properties of irregular cavities using laser refracto-vibrometry," en, *Applied Acoustics*, vol. 130, pp. 177–187, Jan. 2018 (cit. on p. 21).

[42] Y. Oikawa, M. Goto, Y. Ikeda, T. Takizawa, and Y. Yamasaki, "Sound field measurements based on reconstruction from laser projections," in *Proceedings. (ICASSP '05). IEEE International Conference on Acoustics, Speech, and Signal Processing, 2005.*, vol. 4, 2005, iv/661–iv/664 Vol. 4 (cit. on pp. 23, 24).

[43] H. W. Jentink, F. F. M. de Mul, H. E. Suichies, J. G. Aarnoudse, and J. Greve, "Small laser Doppler velocimeter based on the self-mixing effect in a diode laser," en, *Applied Optics*, vol. 27, no. 2, p. 379, Jan. 1988 (cit. on p. 24).

[44] L. Scalise and N. Paone, "Laser Doppler vibrometry based on self-mixing effect," en, *Optics and Lasers in Engineering*, vol. 38, no. 3-4, pp. 173–184, Sep. 2002 (cit. on p. 24).

[45] G. Giuliani, S. Bozzi-Pietra, and S. Donati, "Self-mixing laser diode vibrometer," en, *Measurement Science and Technology*, vol. 14, no. 1, pp. 24–32, Jan. 2003 (cit. on pp. 24, 42, 43, 49, 52).

[46] M. Norgia and A. Pesatori, "Fully analog self-mixing laser vibrometer," en, in *2011 IEEE International Instrumentation and Measurement Technology Conference*, Hangzhou, China: IEEE, May 2011, pp. 1–4 (cit. on p. 24).

[47] S. Donati, "Developing self-mixing interferometry for instrumentation and measurements," en, *Laser & Photonics Reviews*, vol. 6, no. 3, pp. 393–417, May 2012 (cit. on pp. 24, 28).

[48] M. Norgia, D. Melchionni, and S. Donati, "Exploiting the FM-Signal in a Laser-Diode SMI by Means of a Mach–Zehnder Filter," en, *IEEE Photonics Technology Letters*, vol. 29, no. 18, pp. 1552–1555, Sep. 2017 (cit. on pp. 24, 30).

[49] S. Donati and M. Norgia, "Self-Mixing Vibrometer has picometer sensitivity by exploiting the FM Channel," en, in *Conference on Lasers and Electro-Optics*, San Jose, California: OSA, 2018, ATu4M.7 (cit. on p. 24).

[50] L. Campagnolo, M. Nikolić, J. Perchoux, Y. L. Lim, K. Bertling, K. Loubière, L. Prat, A. D. Rakić, and T. Bosch, "Flow profile measurement in microchannel using the optical feedback interferometry sensing technique," en, *Microfluidics and Nanofluidics*, vol. 14, no. 1-2, pp. 113–119, Jan. 2013 (cit. on pp. 24, 33, 37).

[51] L. Campagnolo, "Optical feedback interferometry sensing technique for flow measurements in microchannels," fr, p. 197, Apr. 2013 (cit. on pp. 24, 32, 33, 37, 76).

[52] E Ramírez-Miquet, J. Perchoux, R. D. C. Moreira, Y Zhao, A. L. Arriaga, C. Tronche, and O Sotolongo-Costa, "Optical feedback interferometry: From basics to application of laser flowmetry," en, *Revista Cubana de Fisica*, vol. 34, no. 1, p. 11, 2017 (cit. on pp. 24, 33, 37, 76).

[53] R. Atashkhooei, E. E. Ramirez-Miquet, R. d. C. Moreira, A. Quotb, S. Royo, and J. Perchoux, "Optical Feedback Flowmetry: Impact of Particle Concentration on the Signal Processing Method," en, *IEEE Sensors Journal*, vol. 18, no. 4, pp. 1457–1463, Feb. 2018 (cit. on pp. 24, 76, 91).

[54] F. de Mul, M. Koelink, A. Weijers, J. Greve, J. Aarnoudse, R. Graaff, and A. Dassel, "A semiconductor laser used for direct measurement of the blood perfusion of tissue," en, *IEEE Transactions on Biomedical Engineering*, vol. 40, no. 2, pp. 208–210, Feb. 1993 (cit. on pp. 24, 33, 37).

[55] M. Norgia, A. Pesatori, and L. Rovati, "Self-mixing laser Doppler: A model for extracorporeal blood flow measurement," en, in *2010 IEEE Instrumentation & Measurement Technology Conference Proceedings*, Austin, TX, USA: IEEE, 2010, pp. 304–307 (cit. on pp. 24, 33).

[56] M. Norgia, G. Giuliani, and S. Donati, "Absolute Distance Measurement With Improved Accuracy Using Laser Diode Self-Mixing Interferometry in a Closed Loop," en, *IEEE Transactions on Instrumentation and Measurement*, vol. 56, no. 5, pp. 1894–1900, Oct. 2007 (cit. on p. 24).

[57] L. Rovati, L. Di Cecilia, and S. Cattini, "On the feasibility of Absolute Distance Measurement by using Optical-Feedback into a Superluminescent Diode Cavity," en, *IEEE Transactions on Instrumentation and Measurement*, pp. 1–1, 2019 (cit. on p. 24).

[58] M. Veng, J. Perchoux, and F. Bony, "Fringe Disappearance in Self-Mixing Interferometry Laser Sensors: Model and Application to the Absolute Distance Measurement Scheme," *IEEE Sensors Journal*, pp. 1–1, 2019 (cit. on pp. 24, 28, 43).

[59] F. Urgiles, J. Perchoux, and T. Bosch, "Characterization of Acoustic Sources by Optical Feedback Interferometry," en, *Proceedings*, vol. 1, no. 4, p. 348, Aug. 2017 (cit. on pp. 24, 35, 53, 54).

[60] P. F. Urgiles Ortiz, J. Perchoux, A. L. Arriaga, F. Jayat, and T. Bosch, "Visualization of an acoustic stationary wave by optical feedback interferometry," en, *Optical Engineering*, vol. 57, no. 05, p. 1, Feb. 2018 (cit. on pp. 24, 53, 54).

[61] P. F. Urgiles Ortiz, J. Perchoux, A. L. Arriaga, F. Jayat, and T. Bosch, "Visualization of an acoustic stationary wave by optical feedback interferometry," en, *Optical Engineering*, vol. 57, no. 05, p. 1, Feb. 2018 (cit. on pp. 24, 35, 53, 54).

[62] T Asakura, T. W. Hansch, T Kamiya, F Krausz, B Monemar, M Ohtsu, H Venghaus, H Weber, and H Weinfurter, "Editor-in-Chief: W. T. Rhodes, Atlanta," en, *optical sciences*, p. 489, (cit. on pp. 25, 27, 29).

[63] G. H. M. van Tartwijk and D Lenstra, "Semiconductor lasers with optical injection and feedback," *Quantum and Semiclassical Optics: Journal of the European Optical Society Part B*, vol. 7, no. 2, pp. 87–143, 1995 (cit. on pp. 25, 27, 28).

[64] G. Acket, D. Lenstra, A. Den Boef, and B. Verbeek, "The influence of feedback intensity on longitudinal mode properties and optical noise in index-guided semiconductor lasers," en, *IEEE Journal of Quantum Electronics*, vol. 20, no. 10, pp. 1163–1169, Oct. 1984 (cit. on pp. 26, 44).

[65] W. Wang, K. Grattan, A. Palmer, and W. Boyle, "Self-mixing interference inside a single-mode diode laser for optical sensing applications," en, *Journal of Lightwave Technology*, vol. 12, no. 9, pp. 1577–1587, Sep. 1994 (cit. on pp. 27, 29).

[66] K Petermann, *Laser Diode Modulation and Noise*, en. Dordrecht: Springer Netherlands, 1988, OCLC: 851388814 (cit. on pp. 27, 43).

[67] T. Taimre, M. Nikolić, K. Bertling, Y. L. Lim, T. Bosch, and A. D. Rakić, "Laser feedback interferometry: A tutorial on the self-mixing effect for coherent sensing," en, *Advances in Optics and Photonics*, vol. 7, no. 3, p. 570, Sep. 2015 (cit. on pp. 28, 29, 43, 44, 71, 88).

[68] R. Kliese, T. Taimre, A. A. A. Bakar, Y. L. Lim, K. Bertling, M. Nikolić, J. Perchoux, T. Bosch, and A. D. Rakić, "Solving self-mixing equations for arbitrary feedback levels: A concise algorithm," en, *Applied Optics*, vol. 53, no. 17, p. 3723, Jun. 2014 (cit. on pp. 28, 31, 43–45, 48–51, 73, 131).

[69] C. Henry, "Theory of the linewidth of semiconductor lasers," en, *IEEE Journal of Quantum Electronics*, vol. 18, no. 2, pp. 259–264, Feb. 1982 (cit. on pp. 28, 43).

[70] R. Lang and K. Kobayashi, "External optical feedback effects on semiconductor injection laser properties," en, *IEEE Journal of Quantum Electronics*, vol. 16, no. 3, pp. 347–355, Mar. 1980 (cit. on pp. 28, 43).

[71] L. A. Coldren and S. W. Corzine, *Diode Lasers and Photonic Integrated Circuits*, en. John Wiley & Sons, Ltd, 1995 (cit. on p. 29).

[72] C. A. Grimes, E. C. Dickey, and M. V. Pishko, Eds., *Encyclopedia of sensors*, en. Stevenson Ranch, Calif: American Scientific Publishers, 2006, OCLC: ocm76894825 (cit. on p. 29).

[73] C. Bes, G. Plantier, and T. Bosch, "Displacement Measurements Using a Self-Mixing Laser Diode Under Moderate Feedback," en, *IEEE Transactions on Instrumentation and Measurement*, vol. 55, no. 4, pp. 1101–1105, Aug. 2006 (cit. on p. 32).

[74] A. Luna Arriaga, F. Bony, and T. Bosch, "Analytic phase retrieval of dynamic optical feedback signals for laser vibrometry," en, in *IEEE SENSORS 2014 Proceedings*, Valencia, Spain: IEEE, Nov. 2014, pp. 762–765 (cit. on p. 32).

[75] F. F. M. de Mul, M. H. Koelink, A. L. Weijers, J. Greve, J. G. Aarnoudse, R. Graaff, and A. C. M. Dassel, "Self-mixing laser-Doppler velocimetry of liquid flow and of blood perfusion in tissue," en, *Applied Optics*, vol. 31, no. 27, p. 5844, Sep. 1992 (cit. on pp. 33, 37).

[76] S. Ozdemir, S. Takamiya, S. Ito, S. Shinohara, and H. Yoshida, "Self-mixing laser speckle velocimeter for blood flow measurement," *IEEE Transactions on Instrumentation and Measurement*, vol. 49, no. 5, pp. 1029–1035, Oct. 2000, Conference Name: IEEE Transactions on Instrumentation and Measurement (cit. on p. 33).

[77] S. K. Ozdemir, "Noninvasive blood flow measurement using speckle signals from a self-mixing laser diode: In vitro and in vivo experiments," en, *Optical Engineering*, vol. 39, no. 9, p. 2574, Sep. 2000 (cit. on p. 33).

[78] S. K. Ozdemir, I. Ohno, and S. Shinohara, "Assessment on Self-mixing Laser Interferometry for Blood flow Measurement over Skin Surface," in *2006 IEEE Instrumentation and Measurement Technology Conference Proceedings*, ISSN: 1091-5281, Apr. 2006, pp. 27–31 (cit. on p. 33).

[79] S. K. Ozdemir, I. Ohno, and S. Shinohara, "A Comparative Study for the Assessment on Blood Flow Measurement Using Self-Mixing Laser Speckle Interferometer," en, *IEEE Transactions on Instrumentation and Measurement*, vol. 57, no. 2, pp. 355–363, Feb. 2008 (cit. on p. 33).

[80] J Hast, R. Myllylä, H Sorvoja, and J Miettinen, "Arterial pulse shape measurement using self-mixing effect in a diode laser," en, *Quantum Electronics*, vol. 32, no. 11, pp. 975–980, Nov. 2002 (cit. on p. 33).

[81] J. Hast, R. Myllylä, H. Sorvoja, and J. Miettinen, "Arterial pulse shape measurement using self-mixing interferometry," en, vol. 4956, p. 7, 2003 (cit. on p. 33).

[82] C. Zakian, M. Dickinson, and T. King, "Particle sizing and flow measurement using self-mixing interferometry with a laser diode," en, *Journal of Optics A: Pure and Applied Optics*, vol. 7, no. 6, S445–S452, Jun. 2005 (cit. on p. 33).

[83] M. Norgia, A. Pesatori, and L. Rovati, "Optical flowmeter for blood extracorporeal circulators," in *2009 IEEE Instrumentation and Measurement Technology Conference*, ISSN: 1091-5281, May 2009, pp. 1759–1762 (cit. on p. 33).

[84] Y. Zhao, J. Perchoux, L. Campagnolo, T. Camps, R. Atashkhooei, and V. Bardinal, "Optical feedback interferometry for microscale-flow sensing study: Numerical simulation and experimental validation," en, *Optics Express*, vol. 24, no. 21, p. 23 849, Oct. 2016 (cit. on pp. 33, 37).

[85] Y. Zhao, J. Perchoux, T. Camps, and V. Bardinal, "Optical Feedback Interferometry Flowmetry Sensor in Microfluidics Chip," en, *Proceedings*, vol. 1, no. 4, p. 507, Aug. 2017 (cit. on pp. 33, 37).

[86] R. da Costa Moreira, J. Perchoux, Y. Zhao, C. Tronche, F. Jayat, and T. Bosch, "Single nano-particle flow detection and velocimetry using optical feedback interferometry," en, in *2017 IEEE SENSORS*, Glasgow: IEEE, Oct. 2017, pp. 1–3 (cit. on pp. 33, 37).

[87] Y. Zhao, T. Camps, V. Bardinal, and J. Perchoux, "Optical Feedback Interferometry Based Microfluidic Sensing: Impact of Multi-Parameters on Doppler Spectral Properties," en, *Applied Sciences*, vol. 9, no. 18, p. 3903, Sep. 2019 (cit. on pp. 33, 37).

[88] Y. Zhao, Q. Li, J.-B. Doucet, P.-F. Calmon, F. Mesnilgrente, B. Reig, C. Tronche, T. Camps, J. Perchoux, and V. Bardinal, "Implementation of Integrated VCSEL-Based Optical Feedback Interferometry Microfluidic Sensor System with Polymer Microoptics," en, *Applied Sciences*, vol. 9, no. 24, p. 5484, Dec. 2019 (cit. on p. 33).

[89] P. E. Ciddor, "Refractive index of air: New equations for the visible and near infrared," en, *Applied Optics*, vol. 35, no. 9, p. 1566, Mar. 1996 (cit. on pp. 36, 53, 54).

[90] R. Teysseyre, *Dispositif de mesure de la vitesse du vent*, fr, Apr. 2011 (cit. on p. 37).

[91] E. E. Ramírez-Miquet, "Implementation of Optical Feedback Interferometry for Sensing Applications in Fluidic Systems," en, p. 139, (cit. on pp. 37, 101).

[92] A. N. Lukashkin, M. E. Bashtanov, and I. J. Russell, "A self-mixing laser-diode interferometer for measuring basilar membrane vibrations without opening the cochlea," en, *Journal of Neuroscience Methods*, vol. 148, no. 2, pp. 122–129, Oct. 2005 (cit. on pp. 43, 49).

[93] T. Taimre and A. D. Rakić, "On the nature of Acket's characteristic parameter C in semiconductor lasers," en, *Applied Optics*, vol. 53, no. 5, p. 1001, Feb. 2014 (cit. on p. 44).

[94] U. Zabit, O. D. Bernal, and T. Bosch, "Self-Mixing Laser Sensor for Large Displacements: Signal Recovery in the Presence of Speckle," en, *IEEE Sensors Journal*, vol. 13, no. 2, pp. 824–831, Feb. 2013 (cit. on p. 46).

[95] E. Knudsen, J. Perchoux, T. Mazoyer, F. Jayat, C. Tronche, and T. Bosch, "Lower detection limit of the acousto-optic effect using optical feedback interferometry," in *2020 IEEE International Instrumentation and Measurement Technology Conference (I2MTC)*, 2020, pp. 1–4 (cit. on pp. 53, 73).

[96] B. Edlen, "The Dispersion of Standard Air," en, vol. 43, p. 6, 1953 (cit. on p. 54).

[97] B. Edlén, "The Refractive Index of Air," en, *Metrologia*, vol. 2, no. 2, pp. 71–80, Apr. 1966 (cit. on p. 54).

[98] K. P. Birch and M. J. Downs, "An Updated Edlén Equation for the Refractive Index of Air," en, *Metrologia*, vol. 30, no. 3, pp. 155–162, Jan. 1993 (cit. on p. 54).

[99] K. P. Birch and M. J. Downs, "Correction to the Updated Edl{\'{e}}n Equation for the Refractive Index of Air," en, vol. 31, Jan. 1994 (cit. on p. 54).

[100] J. C. Owens, "Optical Refractive Index of Air: Dependence on Pressure, Temperature and Composition," en, *Applied Optics*, vol. 6, no. 1, p. 51, Jan. 1967 (cit. on p. 54).

[101] E. R. Peck and K. Reeder, "Dispersion of Air*," en, *Journal of the Optical Society of America*, vol. 62, no. 8, p. 958, Aug. 1972 (cit. on p. 54).

[102] K. E. Erickson, "Investigation of the Invariance of Atmospheric Dispersion with a Long-Path Refractometer*," en, *Journal of the Optical Society of America*, vol. 52, no. 7, p. 777, Jul. 1962 (cit. on p. 54).

[103] H. Barrell and J. E. Sears, "The refraction and dispersion of air and dispersion of air for the visible spectrum," en, *Philosophical Transactions of the Royal Society of London. Series A, Mathematical and Physical Sciences*, vol. 238, no. 786, pp. 1–64, Feb. 1939 (cit. on p. 54).

[104] K. J. Taylor, "Absolute measurement of acoustic particle velocity," en, *The Journal of the Acoustical Society of America*, vol. 59, no. 3, pp. 691–694, Mar. 1976 (cit. on pp. 77, 78).

[105] S. Temkin and C.-M. Leung, "On the velocity of a rigid sphere in a sound wave," en, *Journal of Sound and Vibration*, vol. 49, no. 1, pp. 75–92, Nov. 1976 (cit. on p. 77).

[106] D. Zhou, Z. Luo, M. Fang, M. Lu, J. Jiang, H. Chen, and M. He, "Numerical calculation of particle movement in sound wave fields and experimental verification through high-speed photography," en, *Applied Energy*, vol. 185, pp. 2245–2250, Jan. 2017 (cit. on pp. 77, 78).

[107] M. Bruneau, *Manuel d'acoutistique fondamentale*, French. Paris: Hermès, 1998, OCLC: 1132457984 (cit. on p. 78).

[108] *Correlation coefficients - MATLAB corrcoef - MathWorks France* (cit. on p. 108).

Résumé — Dans cette thèse, nous présentons le développement d'un microphone de Classe 1 utilisant l'interférométrie à réinjection optique. Les ondes acoustiques sont mesurées grâce à l'effet acousto-optique. Nous construisons une expérience dédiée, répétable et robuste montrant l'impact de la forme de la frange sur les acquisitions de variations de chemin optique sub-$\lambda/2$. Nous démontrons expérimentalement que l'amplitude du signal acquis est couplée linéairement à la pente de la frange, un résultat pas encore explicitement publié dans la littérature OFI. En tant que deuxième sujet de recherche de cette thèse, nous présentons un démonstrateur du LIDAR acoustique par interférométrie à réinjection optique pour les acquisitions à distance d'ondes acoustiques. Nous développons un algorithme de démodulation qui extrait les informations acoustiques d'un flux de particules fait osciller par une onde acoustique. Le démonstrateur expérimental est capable d'acquérir des ondes acoustiques à distance à plus de 11 m du capteur.

Mots clés : Optical Feedback Interferometry, Acoustics, Remote Sensing, Laser.

Abstract — In this PhD we present the development of a Class 1 microphone using Optical Feedback Interferometry. The acoustic waves are measured thought the acousto-optic effect. We build a dedicated, repeatable and robust experiment showing the impact of the fringe shape on acquisitions of sub-$\lambda/2$ optical path variations. We demonstrate experimentally that the aquired signal amplitude is linearly coupled to the slope of the fringe, a result not yet explicitly published in the OFI literature. As a second research subject in this PhD we present a demonstrator of the Acoustic LIDAR by Optical Feedback Interferometry for the remote acquisitions of acoustic waves. We develop a demodulation algorithm that extracts the acoustic information from a flow of particles that is made to oscillate by an acoustic wave. The experimental demonstrator is capable of acquiring acoustic waves remotely at over 11 m from the detector.

Keywords: Optical Feedback Interferometry, Acoustics, Remote Sensing, Laser.

LAAS-CNRS, Université de Toulouse, CNRS, INP / ACOEM
Toulouse / Limonest